Growth and Doping of Zinc Selenide Using Alternative Gaseous Source Epitaxial Techniques

by

Easen Ho

B. S. Electrical Engineering
University of Washington, 1987

M. E. in Information Processing
Tokyo Institute of Technology, 1990

SUBMITTED TO THE DEPARTMENT OF ELECTRICAL ENGINEERING AND COMPUTER SCIENCE IN PARTIAL FULFILLMENT OF THE REQUIREMENTS FOR THE DEGREE OF

DOCTOR OF PHILOSOPHY IN ELECTRICAL ENGINEERING
AT THE
MASSACHUSETTS INSTITUTE OF TECHNOLOGY

JUNE 1996

Signature of Author ___
Department of Electrical Engineering and Computer Science
March 13, 1996

Certified by _____
Leslie A. Kolodziejski
Esther and Harold E. Edgerton Associate Professor of Electrical Engineering and Computer Science

Accepted by ___
Frederick R. Morgenthaler
l Engineering and Computer Science
Chairman, Department Committee on Graduate Students

Growth And Doping Of Zinc Selenide Using Alternative Gaseous Source Epitaxial Techniques

by

Easen Ho

Submitted to The Department Of Electrical Engineering and Computer Science on March 8, 1996, in partial fulfillment of the requirements for the Degree of Doctor of Philosophy in Electrical Engineering

Abstract

Zinc Selenide based II-VI wide bandgap materials are promising candidates for visible light emitters operating in the blue regime of the visible spectrum. Much progress has been demonstrated in the epitaxy and amphoteric doping of ZnSe in recent years using molecular beam epitaxy (MBE), and ultimately resulted in the first demonstration of a continuous wave, room temperature injection laser diode in 1993. Aiming to overcome some of the significant shortcomings, e.g., repeatability in flux control, of the MBE technique as applied to II-VI's, the growth of ZnSe using various alternative gaseous source epitaxy techniques that retain the benefits of an UHV background has been investigated. Using metalorganic precursors for both the group II and group VI elements, metalorganic molecular beam epitaxy (MOMBE) has been found to be suitable for selective epitaxy applications; this technique is hampered in their general suitability for II-VI growth only by the requirement of a uniform photon irradiation during growth. Both n-type, using chlorine, and p-type doping, using a plasma source of nitrogen, of ZnSe have been attempted during gas source molecular beam epitaxy (GSMBE), where a hydride source of selenium is substituted for the high vapor-pressure solid selenium. While predictable incorporation of both dopants have been observed, only n-type activation has been consistently obtained. Subsequent comparisons with MBE indicated that hydrogen, both in the form of sub-hydrides attached to the anion precursors as well as any H_2 that is present in the growth environment, can lead to significant passivation of the nitrogen acceptors. These hydrogenation

results have important implications for the applicability of various epitaxial methods currently in use for the growth of II-VI compounds where appreciable H_2 may be present in the growth environment.

Motivated by the short lifetimes experienced by the state of the art blue-green injection laser diodes, we have also carried out parallel investigations into the use of novel III-V epitaxial buffer layers for the heteroepitaxy of ZnSe. These i*n-situ*-transferred buffer layers are capable of providing simultaneous lattice-matching and reduced hole-injection barriers to p-type ZnSe. Our preliminary results indicate that ZnSe with comparable optical qualities to those grown on GaAs can be obtained using MBE. Room temperature cathodoluminescence (CL) characterization has also been shown to afford fast and direct feedback that can be useful in the continuing effort to reduce the densities of both strain- and nucleation-related defects on these novel buffer layers.

Thesis Supervisor: Leslie Kolodziejski

Title: Esther and Harold E. Edgerton Associate Professor of Electrical Engineering and Computer Science

Acknowledgments

Conducting research in the area of epitaxial growth necessarily involves a group effort. The long hours and the need to juggle multiple events in parallel make collaborators and "buddies" all the more important in maintaining a smoothly running laboratory. Throughout my stay at the CBE laboratory, I have been fortunate to have the help of a number of co-workers that made it possible for me to carryout my research through their various contributions and support. Every past and present member of the CBE lab had in some way provided help and friendship that served to enhance my MIT experience. My gratitude goes to the following individuals: Joe Ahadian, Ziad Azzam, George Chen, Chris Coronado, Jay Damask, Philip Fisher, James Geraci, Jody House, Carmen Huber, Hisashi Kanie, David Lee, Anna Lopatnikova, Kuo-Yi Lim, Kan Lu, Elisabeth Marley, Mariya Minkova, Jeremy Milikow, Gene Nanto, Sang-Hoon Park, Steve Patterson, Gale Petrich, Steve Shephard, Jack Shue, Tom Tang, Emily Warlick, and Ayca Yuksel. Thanks also go to Angela Odoardi and Charmaine Cudjoe for taking care of various administrative duties over the years, and picking up after us in general. Acknowledgment also goes to Richard Perilli, whose facility know-how's and candid advice in various matters are greatly appreciated.

Various individuals, particularly those in the II-VI research group, have made especially appreciated contributions to both professional and personal aspects of my Ph.D. career and therefore deserve special recognition. From my own perspective, the most difficult period of my MIT career was the first couple of years: long lab hours, impossibly-long problem sets, and the first-hand experience of the Murphy's law in equipment troubles. The support and guidance of

the small and tightly knit group (consisting of Leslie, myself, Steve Shephard, Chris Coronado, and Carmen Huber) were instrumental in helping me gain a foothold in the MIT environment. In particular, my friend and long-time co-worker, Chris Coronado, played a key role in "breaking me in", and to whom I owe the lion share of my acknowledgments. He had consistently shouldered the burdens of the lab when problem sets and various exams threatened to overcome me. I also enjoyed and valued his companionship in the various extracurricular activities we shared. Thanks also goes to Steve Shephard for shepherding the system through the initial specification and installation processes.

As the bugs in the epitaxy system were stamped out on-by-one, the size of the group also increased: it seemed, however, that workload and research commitments always outpaced available hands. As the need for each student to specialize in some particular characterization method increased, the help of Jody House, particularly in performing numerous photoluminescence measurements (often on short notice), is greatly appreciated. The aid and companionship of Philip Fisher also eased the operational and maintenance burdens of the II-VI system. To Mr. Fisher, whom I have known since my undergraduate years: I wish him much success in whatever endeavor he eventually undertakes with the full force of his personal conviction.

Particularly sincere thanks also go to Dr. Gale Petrich for: (*i*) churning out beautiful buffer layers one after another; (*ii*) greasing the wheels so that the lab can proceed with some semblance of order; (*iii*) fixing anything that's not working in the lab; and (*iv*) providing endless hours of (mutual?) amusement poking fun at one another; and (*v*) converting to a die-hard windows addict. The latter part of my research would not have been possible without his numerous contributions and sacrifices in the name of research. Gratitude is also due Emily Warlick, the

latest member of the II-VI team and future "chief veterinarian" of the II-VI beast. Her help was particularly appreciated during the time of my thesis preparation as most of the workload had fallen on her shoulders. She has my best wishes for a successful (and succinct) Ph.D. career.

Lastly but by no mean least, words cannot express my appreciation for the enduring guidance, support (☺☺☺+$$$) and care of Professor Leslie Kolodziejski. Her generosity in allowing us to purchase additional equipment and affect repairs as necessary greatly reduced the amount of work and headache required of us. Being the student with (thus far) the longest tenancy in her lab, and one who has witnessed the hard work and tribulations in her path toward tenureship, I am truly glad that she finally received her just deserves. Her philosophy that "a professor doesn't have to be lofty, dictatorial, and unapproachable" made the quality of life at MIT that much more bearable for me. I sincerely hope that her crusade to make MIT a "better and gentler place" and her willingness to accept her students as her peers will continue to triumph. I would also like to thank Professor Fonstad and Professor Fitzgerald for serving on my thesis committee, and for their many helpful suggestions.

On a more personal but equally important note, all of this would not be possible without the understanding, love and support of my parents, my brother Eugene and the rest of the family. To my parents, to whom I owe the greatest love and respect as well as debt of gratitude: my achievements are but reflections of your years of moral guidance and nurturing. Finally, I could not have done it without the love and companionship of Jennifer, my "significant other", who has unerringly stayed by my side throughout all the good times and the bad.

Table of Contents

List of Figures

List of Tables

1. Background and Motivation

1.1 Why ZnSe?

With a direct room temperature bandgap of 2.67 eV (or 464 nm), ZnSe has been the focus of on going research effort for over 30 years, primarily as a candidate material for blue light emitting devices. Together with Mg and S, ZnSe-based II-VI compounds are capable of spanning the energy and lattice constant ranges between 2.67 eV to 4.5 eV, and 5.42 Å to 5.89 Å, respectively. Figure 1–1 shows a plot of the energy bandgap versus lattice constant diagram for II-VI compounds as well as some common III-V and group IV materials. The shaded region in

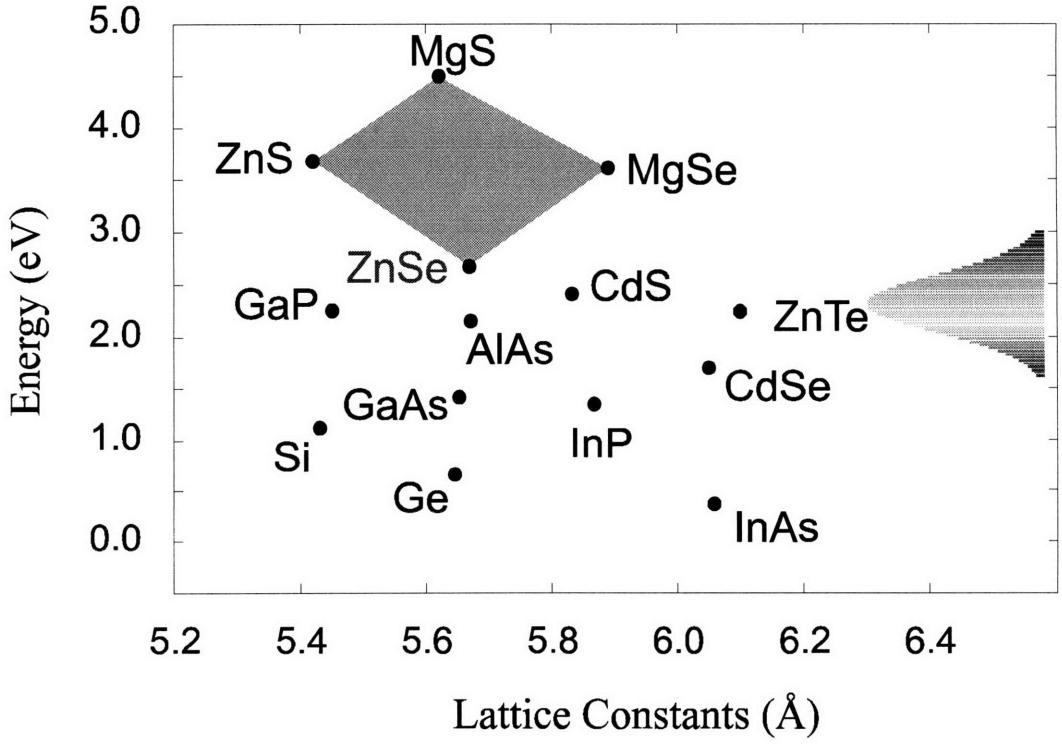

Figure 1–1 Bandgap versus lattice constant diagram for II-VI and III-V binary materials. The curve near the right hand vertical axis schematically indicates the spectral sensitivity of the human eye.

Figure 1–1 highlights the bandgap ranges that can be achieved using the (Zn,Mg)(S,Se) system that has been actively pursued only in the last few years.

Numerous applications exist that would benefit from the availability of a practical blue or blue-green semiconductor light source: spectroscopy, underwater communications, information displays, and optical data storage. Optical data storage is arguably the most lucrative application with tremendous mass-market potential. As the diffraction-limited minimum spot size of a focused optical beam is approximately proportional to λ/NA (where λ is the wavelength of light and NA the numerical aperture of the objective lens), a recording density improvement of 4-5X over that currently achievable using infra-red GaAs-based diodes is expected. As a result, major corporations such as Sony, Philips, Mitsubishi, and 3M have established considerable research efforts in the II-VI arena.

A major obstacle encountered by early research efforts in ZnSe was its resistance to various p-type doping attempts by "self-compensation", where compensating n-type defects appear in response to acceptor introduction and results in electrically inactive acceptors [1,2,3]. It was not until the successful application of a plasma source of nitrogen during molecular beam epitaxy (MBE) in 1990 that definitive p-type conversion was demonstrated [4,5]. Since then, the progress in II-VI research has been impressive: the first injection laser diode was demonstrated in 1991 [6], and the first continuous wave, room temperature operation of a II-VI laser diode was obtained in 1993 utilizing a ZnSe/ZnCdSe quantum well active region and (Zn,Mg)(S,Se) optical confinement layers [7]. Recently, Ishibashi et al. reported the CW operation of (Zn,Mg)(S,Se)-based multi-quantum-well laser diodes having a maximum lifetime of up to 1 hour at room temperature [8]. Structural degradation of the II-VI active region has thus far limited the lifetime of laser diodes to the order of hours of CW operation at room temperature: a far cry from the

tens of thousands of hours of useful lifetime exhibited by commercial GaAs-based laser diodes. After several years of a headlong rush toward laser device demonstrations, the II-VI community has now refocused research efforts back to detail material and epitaxial issues in an effort to prolong the device lifetimes. One must, however, appraise the II-VI optical devices' rate of progress in proper perspective. In light of the fact that amphoteric conduction was only achieved approximately five years ago, the progress of II-VI laser and light emitting diodes has indeed been impressive as well as exciting.

1.2 Comparison of Epitaxial Techniques

A number of advanced thin-film epitaxial growth techniques with atomic-layer precision have been developed in the last one to two decades and applied to the deposition of III-V compound semiconductors with much success. These include molecular beam epitaxy (MBE), metalorganic vapor phase epitaxy (MOVPE) or metalorganic chemical vapor deposition (MOCVD), chemical beam epitaxy (CBE), metalorganic molecular beam epitaxy (MOMBE), and gas source molecular beam epitaxy (GSMBE). To clarify possible confusion in naming conventions, Table 1-1 provides a set of definitions used throughout this thesis, along with some characteristic advantages and disadvantages of each of these techniques. Although the merits of some of these techniques (as applied to wide bandgap II-VI materials) will be born out in more detail in later chapters, it is nevertheless useful at this point to illustrate the ways in which the various techniques are related in a general "physical" sense. Figure 1–2 schematically compares these epitaxial growth techniques in terms of their source flexibility, background pressure, as well as their suitability for the application of a variety of useful *in-situ* characterization tools.

Table 1-1 Definition and comparison of various epitaxial growth techniques in terms of their advantages and disadvantages

Name	***Molecular Beam Epitaxy***	***Metalorganic Vapor Phase Epitaxy or Metalorganic Chemical Vapor Deposition***	***Gas Source Molecular Beam Epitaxy***	***Chemical Beam Epitaxy***	***Metalorganic Molecular Beam Epitaxy***
Acronyms	MBE	MOVPE or MOCVD	GSMBE	CBE	MOMBE
Group II Sources	solid elemental sources	metalorganic sources	solid elemental sources	metalorganic sources	metalorganic sources
Group VI Sources	solid elemental sources	metal-organic or hydride sources	hydrides	hydrides	metalorganic sources
Advantages	UHV; simple surface chemistry; high purity sources available; mature technology	easily adaptable to mass production; ex-situ source replenishment; rich surface chemistry	UHV; retains surface chemistry aspect of MOVPE; precision control of sources	UHV; retains surface chemistry aspect of MOVPE; precision control of sources	UHV; retains surface chemistry aspect of MOVPE; precision control of sources
Dis-advantages	difficult flux control of volatile group V or VI elements	large amount of highly toxic sources required; insufficiently pure sources	highly toxic hydrides required	highly toxic hydrides required; insufficiently pure sources	insufficiently pure sources

From the figure, it is apparent that the "alternative gaseous source approaches", e.g., MOMBE, GSMBE and CBE, represent hybrids of the MBE and MOVPE techniques such that the most desirable property of the constituents (i.e. the UHV environment of MBE and the source flexibility of MOVPE) are combined. To date, significant and substantial progress in the field of II-VI device research has been realized primarily by employing conventional MBE with all solid sources. The potential offered by implementing *in-situ* feedback (thus excellent compositional control) and source flexibility, as well as the feasibility for production scaling, constitute the major impetus for our efforts in applying these alternative gaseous source epitaxial methods to the II-VI family of semiconductor compounds.

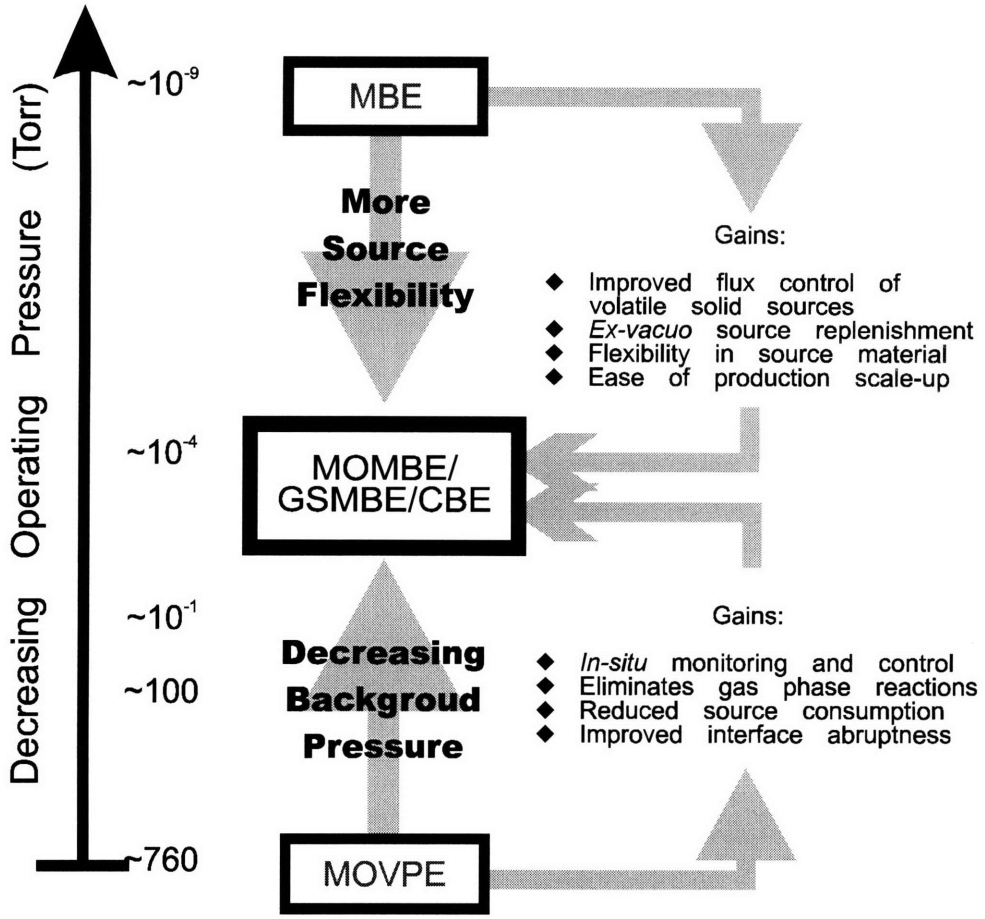

Figure 1–2 Comparisons of the physical properties and the relative merits of the key epitaxial growth techniques employed for the fabrication of semiconductor heterostructures.

1.3 Outline of This Thesis

The goal of this research is to apply these alternative gaseous source epitaxial techniques to the heteroepitaxy of the archetypical II-VI compound, ZnSe, on GaAs substrates. Our decision to adopt these novel technique was initially motivated by the desire to provide solutions to the previously-discussed shortcomings of the widely-used MBE technique. We were also concerned with the ease of production scale-up for future commercialization purposes. It was further hoped

that by exploring the different chemical and kinetic environments at the growth surface will provide addition degree of control over the growth processes, and lead to better understanding of critical issues such as dopant incorporation and native defect generation.

After a brief section describing the state-of-the-art in several aspects of the II-VI research (in Section 1.4), Chapter 2 begins with our results on the MOMBE growth of ZnSe on GaAs using a combination of diethyl and dimethyl sources of Zn and Se. Beam-assisted growth (using photons and electrons) was found to be particularly effective for achieving maskless selective epitaxy in this mode of growth.

Due to a combination of the observed low unilluminated growth rates and metalorganic source purity issues, however, we subsequently began to explore the use of GSMBE technique for the growth of ZnSe. Chapter 3 describes the growth of ZnSe by GSMBE on bulk GaAs, as well as various *in-situ* transferred epitaxial GaAs and other III-V buffer layers. Both n-type doping using chlorine and p-type doping using nitrogen have been investigated. The issue of hydrogen passivation of dopants were also examined in detail; intentionally introduced hydrogen was used during conventional MBE to gain a better understanding of the source and behavior of the hydrogen passivation.

Chapter 4 presents some preliminary results from our parallel and on-going effort in the study of II-VI/III-V heteroepitaxy. Our primary aims in this area can be broadly stated as: (*i*) to understand the effect of nucleation, growth, and surface chemical conditions on the structural and defect properties of the ZnSe epilayer; (*ii*) to investigate the use of novel III-V buffer layers having intermediate bandgap energies between those of ZnSe and GaAs as hole-injection layers. Cathodoluminescence (CL) imaging was extensively used as a fast and direct method to obtain semi-quantitative information on the microstructural defect properties of ZnSe. Very

encouraging results have been realized in controlling the nucleation conditions, resulting in reduced densities of threading dislocation defects in the ZnSe overlayer grown on lattice-mismatched GaAs buffer layers of controlled surface stoichiometry.

1.4 Current State of the Art in II-VI Materials Research

1.4.1 Heteroepitaxial growth of ZnSe on GaAs

GaAs has since became the de-facto substrate for the growth of ZnSe-based II-VI structures because of its fairly close lattice match with ZnSe (0.27%), compatible thermal expansion coefficient, and most important of all, the scarcity of suitable ZnSe substrates. The maturity of the GaAs industry effectively guarantees that a ready supply of high quality and inexpensive wafers will be available in various sizes and conductivities. MBE growth of ZnSe on GaAs substrates has thus far contributed to the majority of materials and device advances in the widegap II-VI material system. The first demonstration of unambiguous p-type doping [4,5], as well as the first injection laser diodes [6] were products of the MBE technique. The availability of *in-situ* characterization techniques, low temperature growth, the chemical simplicity, and the hydrogen-free UHV environment are the main reasons for the success of the MBE-grown materials.

There has also been a substantial amount of effort to develop MOVPE of ZnSe on GaAs, but with limited success: although high quality (both optically and structurally) ZnSe have been reported, p-type conversion of layers grown by MOVPE has proven to be elusive due to unintentional hydrogen incorporation originating from the source species and/or the large amount of hydrogen that is present in the MOVPE growth environment [9,10]. Typical MOVPE-grown

ZnSe:N layers were reported to be highly resistive due to hydrogen passivation. Another quandary that faces the MOVPE technique is the trade-off between the higher growth temperature required when simpler metalorganic precursors (such as dimethyl- and diethyl-compounds of Zn and Se) that can yield better optical qualities are used, and the higher nitrogen acceptor activation that has been observed when novel sources such as ditertiarybutylselenide [11,12] were used at lower growth temperatures.

Until recently, highest reported net acceptor concentrations ($[N_A-N_D]$) for as-grown ZnSe:N films by MOVPE were ~1-2x10^{17} cm^{-3} [13]: this is still significantly below the ~ 10^{18} cm^{-3} achievable by MBE. Although thermal annealing was reported to increase $[N_A-N_D]$ of ZnSe:N films grown by MOVPE [14], the achievement of as-grown p-type films remains a considerable barrier for successful application of MOVPE in the growth of ZnSe. Several recent reports, however, gave considerable grounds for optimism that the all-pervasive hydrogen problem could at least be reduced under certain circumstances. Fujita et al. reported recently that net acceptor concentrations comparable to those obtainable by MBE are possible by using a combination of dimethylzinc, dimethylselenide and tertiarybutylamine during photo-assisted MOVPE growth [15]. Although the mechanism that led to the reduced passivation is still unknown, 77K, pulsed operation of a ZnCdSe single quantum well laser device with ZnMgSSe cladding layers has been demonstrated on GaAs substrate using photo-assisted MOVPE[16].

Other alternative gas source methods such as GSMBE, CBE and MOMBE have largely been met with the similar hydrogen passivation predicament. Apart from our own results, progress in the MOMBE/CBE field has been fairly stagnant except for the pioneering work by Ando et al. [17] and Kobayashi et al. [18], as well as one other report of ZnSe growth from Hughes research laboratory [19]. To our best knowledge, there are only two other groups in the world that are

currently pursuing the GSMBE approach [20,21]. Although GSMBE-grown laser diodes have been demonstrated by researchers at the Mitsubishi Electric Co. [22], the performance has been inferior to the MBE-grown counterparts. Portions of their doping results have in fact been the subject of some controversy at various conferences.

1.4.2 Homo-epitaxial growth of ZnSe on ZnSe

All of the strain-related defect issues are of course eliminated if high quality and conductive ZnSe substrates are made available. At the present, ZnSe substrates are available commercially in experimental quantities from Sumitomo Electric Co., although the high cost (~ $400 for 5x5 mm^2 samples) and inconsistency of the crystal quality still present major problems for homoepitaxy. Using specially-contracted ZnSe wafers from Eagle-Pitcher [23,24], highly encouraging results have been reported by workers at the North Carolina State University, demonstrating efficient LED's [25,26] as well as injection laser diodes operating near room temperature under pulsed conditions [27]. A large part of the difficulty presently facing ZnSe homoepitaxy, which is also the subject of current research efforts in bulk ZnSe growth, arises from: (*i*) surface preparation methods prior to epitaxial growth, and (*ii*) the lack of conducting ZnSe-bulk substrates for vertical injection of carriers.

1.4.3 ZnSe Injection Light Emitting and Laser Diodes

Throughout the history of laser diode development, demonstration of injection laser operation at cryogenic temperatures has often been used as an important milestone in assessing the potential of new device structures or material systems. After many decades of research toward realization of p-type doping of ZnSe, the successful use of a nitrogen plasma source during MBE growth of ZnSe in 1992 very quickly led to the first demonstrations of 77 K, pulsed

injection laser diodes emitting in the blue-green region of the optical spectrum [6,28]. Due to the lack of a suitable wide-gap barrier and cladding material, ZnSe/ZnCdSe/ZnSe quantum wells were used as the active region of the first injection diodes. Introduction of (Zn,Mg)(S,Se) quaternary material [29,30] in late 1992 substantially increased the device designer's flexibility, and resulted in the gradual shortening of the operating wavelength [31,32] along with increasing operating temperatures and duty cycles toward room temperature [33,34]. State-of-the-art ZnSe-based injection diodes today can operate at room temperature under continuous-wave operation with lifetimes on the order of hours emitting at around 480 nm [35,36]. These devices are nominally pseudomorphic structures lattice-matched to GaAs, and make use of wider bandgap ZnMgSSe quaternaries in separate-confinement-quantum-well heterostructure configurations to improve photon and carrier confinement. Significant progress has also been made in using superlattice structures as p-type contact layers to reduce the operating voltages [37,38,39]. The impressive progress of the last few years is only tempered by the short lifetimes of the injection diodes due to what is believed to be the large number of defects that still exist in the diode structures.

The thrust of the current II-VI research effort has since been re-directed toward better understanding of the fundamental defect generation mechanisms during the heteroepitaxial growth process. With competition from GaN-based wide-gap laser devices increasing [40], the ability to control and reduce the grown-in defects due to both strain- and nucleation-related mechanisms are the key first step in maintaining the head start that the II-VI community has built in the race toward a practical blue diode laser. The unique system of interconnected II-VI and III-V chambers at MIT allows us to explore these important interface issues with the flexibility to

alter the condition and chemical makeup of the epitaxial starting surface, as well as to perform the II-VI heteroepitaxy using various epitaxial techniques.

2. *Metalorganic Molecular Beam Epitaxy of ZnSe*

2.1 Advantages and Disadvantages of MOMBE

Of the spectrum of epitaxial growth technologies in existence, the two main-stream techniques of MBE and MOVPE represent the two extremes in terms of their operating pressure regimes. The ultrahigh vacuum (UHV) environment of MBE allows for easy application of various *in-situ* monitoring methods, such as reflection high energy electron diffraction (RHEED), quadrupole mass spectrometry (QMS), and quartz crystal oscillators. Information derived from these *in-situ* tools has greatly facilitated the compositional and stoichiometric control during growth of compound semiconductors, allowing for monolayer-level thickness control. On the other hand, although MOVPE lacks the complement of *in-situ* characterization methods found in MBE, clear advantages are realized in terms of source flexibility and ease of flux control and manipulation. MOMBE techniques can therefore be considered as a stylized idealization that combines the best aspects of MBE and MOVPE. By using metalorganic gas sources in an UHV-environment, MOMBE retains the MOVPE-like source flexibility and precise flux control advantages, while simultaneously allowing for the use of *in-situ* techniques that are normally available only in UHV-compatible growth methods like MBE.

Relative to MBE, MOMBE embodies the following important advantages:

1. Use of precision mass flow controllers for both Group II and Group VI precursors allows for precise flux control.

2. Ex-situ source replenishment effectively results in a semi-infinite supply of the source materials.
3. A rich chemistry, e.g., the presence of a variety of precursor molecules, at the growth surface provides additional incorporation pathways such that the reaction can be fine tuned or engineered. For example, maskless selective area epitaxy can be relatively easily achieved.

Advantages of the MOMBE technique as compared to MOVPE, on the other hand, include:

1. The UHV background allows for the use of various *in-situ* characterization tools such as RHEED and QMS. In addition, other vacuum-compatible sources such as radio-frequency (RF), or electron cyclotron resonance (ECR), plasma sources can be utilized.
2. A much smaller flow of precursor (without the necessity of using a large amount of H_2 carrier gas) reduces the safety risks associated with the handling of exhaust gases.

On the down side, however, MOMBE systems tend to be fairly complicated. The full complement of gas and exhaust handling equipment that is typical for MOVPE is still required for MOMBE. In addition, large pumping systems are necessary to achieve both (*i*) high through-put (to maintain molecular beam conditions during gaseous growth); and (*ii*) low background pressure (to maintain an UHV environment). *In-situ* characterization tools have become indispensable in controlling the growth process, and are therefore necessarily operated in higher pressure regimes than those typically encountered during MBE. This leads to somewhat compromised service lifetime performance for some apparatuses such as electron guns and ionization gauges.

2.2 Epitaxy System and Experimental Setup

Figure 2–1 depicts the epitaxy system at MIT employed for the heteroepitaxy of ZnSe on GaAs by MOMBE. Two growth chambers (a Riber CBE32P III-V GSMBE reactor and a custom II-VI MOMBE/GSMBE/MBE chamber) are interconnected through a system of UHV transfer and buffer chambers. An analytical chamber equipped with an Auger Electron Analyzer (AES) and *in-situ* metallization capability is also attached to the transfer chamber. The ability to transfer samples in an UHV environment makes this system highly unique and particularly well suited for heteroepitaxial research. In order to achieve both high pumping speed as well as low ultimate pressures, the II-VI reactor is outfitted with a combination of pumps including ion (440 liters/s), cryogenic (1500 liter/s), diffusion (2300 liter/s), as well as a titanium sublimation pump. The ultimate vacuum that can be achieved in the II-VI chamber after a system bake is typically $\leq$ $1x10^{-9}$ Torr. A liquid nitrogen-cooled cyrotrap is positioned between the II-VI chamber and the diffusion pump in order to prevent back-streaming of oil vapor. Using the proper combination of effusion and cracking ovens, the same system can be used for GSMBE as well as MBE growth of ZnSe. The chamber is also equipped with a RF plasma cell for nitrogen doping as well as hydrogen plasma cleaning of bulk substrate surfaces. A sapphire viewport inclined 45° relative to the substrate assembly (with the loaded substrate facing down) is used to introduce optical radiation for photo-assisted growth. Elemental source fluxes are measured using a water-cooled quartz crystal oscillator that is fitted on a flexible bellow, allowing it to be positioned two to three centimeters below the substrate.

Figure 2–2(a) is a schematic of the II-VI reactor showing the locations and the orientations of the sources and the substrate assembly. In addition to the two opposing ports for the RHEED gun and the phosphorous screen, eight 6" flange positions are available for installation of effusion ovens, cracker cells, viewports, etc. The distance between the tip of a typical effusion oven to the substrate is approximately 20 cm. The substrate assembly can be rotated under computer control to improve the film thickness uniformity. Various smaller flange ports (not shown) are fitted with optical pyrometer, CCD camera and general-purpose viewports. All of the effusion ovens and the high (group VI) and low temperature (group II) gas injectors (or crackers) were designed and manufactured by EPI Corporation of Minnesota.

Figure 2–2(b) shows a schematic diagram of the II-VI metalorganics gas manifold. The metalorganic precursors are introduced into the vacuum chamber through crackers fed by heated stainless steel tubes to minimize condensation. Coaxial double-shielded stainless steel lines are used for highly toxic precursors such as hydrides used in GSMBE growths. A vent-run configuration (with the vent-lines evacuated by a diffusion/mechanical rotary pump combination) was chosen to minimize the gas-switching time and reduce pressure transients. The metalorganic bubblers are housed in temperature-controlled isothermal baths in order to achieve the desirable vapor pressures for regulation by mass flow controllers without necessitating the use of carrier gases. The all-metal mass flow controllers were manufactured by MKS Corporation, with flow capabilities between 0 to 10 SCCM. In cases where the use of hydrogen is desired, a heated palladium cell is used for purification. All exhausts generated by the system are routed through a toxic gas absorber (TGA) containing activated carbon-based resins before exiting the room.

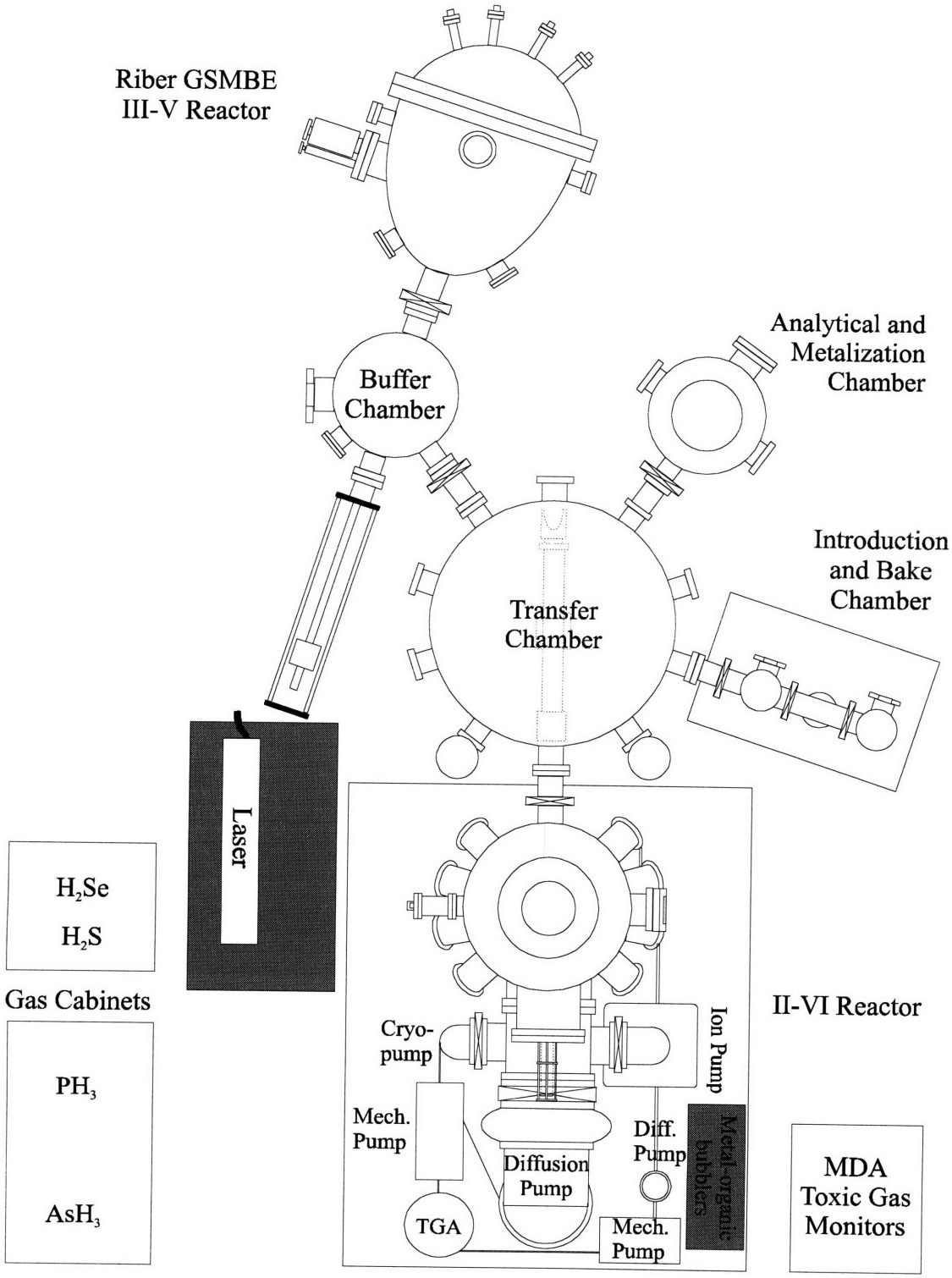

Figure 2–1 Schematic diagram of the MIT heteroepitaxy system with UHV-connected growth chambers dedicated to the III-V and II-VI system of materials.

Diethylzinc (DEZn) and diethylselenium (DESe) were normally used as the metalorganic group II and group VI precursor, respectively. These sources have sufficient vapor pressure near room temperature such that a H_2 carrier gas is not required (as is usually the case for MOVPE that demands large flows of the precursor gases). In addition, dimethylzinc (DMZn) as well as elemental Zn and Se were used in order to aid our understanding of the complex behavior of the MOMBE growth mechanisms. Due to their thermal stability, DESe and DMZn required thermal decomposition in a pyrolytic boron nitride (PBN) cracker having tantalum baffles. The typical cracking temperatures for DESe and DMZn were 800 and 1050°C, respectively, and were determined using QMS of the gas beam. DEZn was found to pyrolyze readily on the ZnSe surface at normal growth temperatures. In order to reduce accumulation in the gas injector, the DEZn cracker was set at 50°C in nearly all growths.

The majority of the films investigated in this MOMBE study were grown at a calibrated substrate temperature of 320°C; however, substrate temperatures ranging from 150°C to 475°C have been explored.* The substrate temperature was calibrated using a low temperature optical pyrometer to measure the eutectic phase transition (356°C) of 500 Å of Au deposited onto a Ge substrate. Eutectic chips were mounted along-side indium-bonded GaAs wafers on molybdenum holders to calibrate the thermocouple readings for each experiment. The correspondence between the pyrometer and the thermocouple was found to depend on various parameters such as the size of the sample used, details of the mounting procedure, and the surface conditions of the molybdenum holder.

---

* Unless otherwise specified, all growth temperatures stated in this thesis are calibrated temperatures, i.e., pyrometer reading.

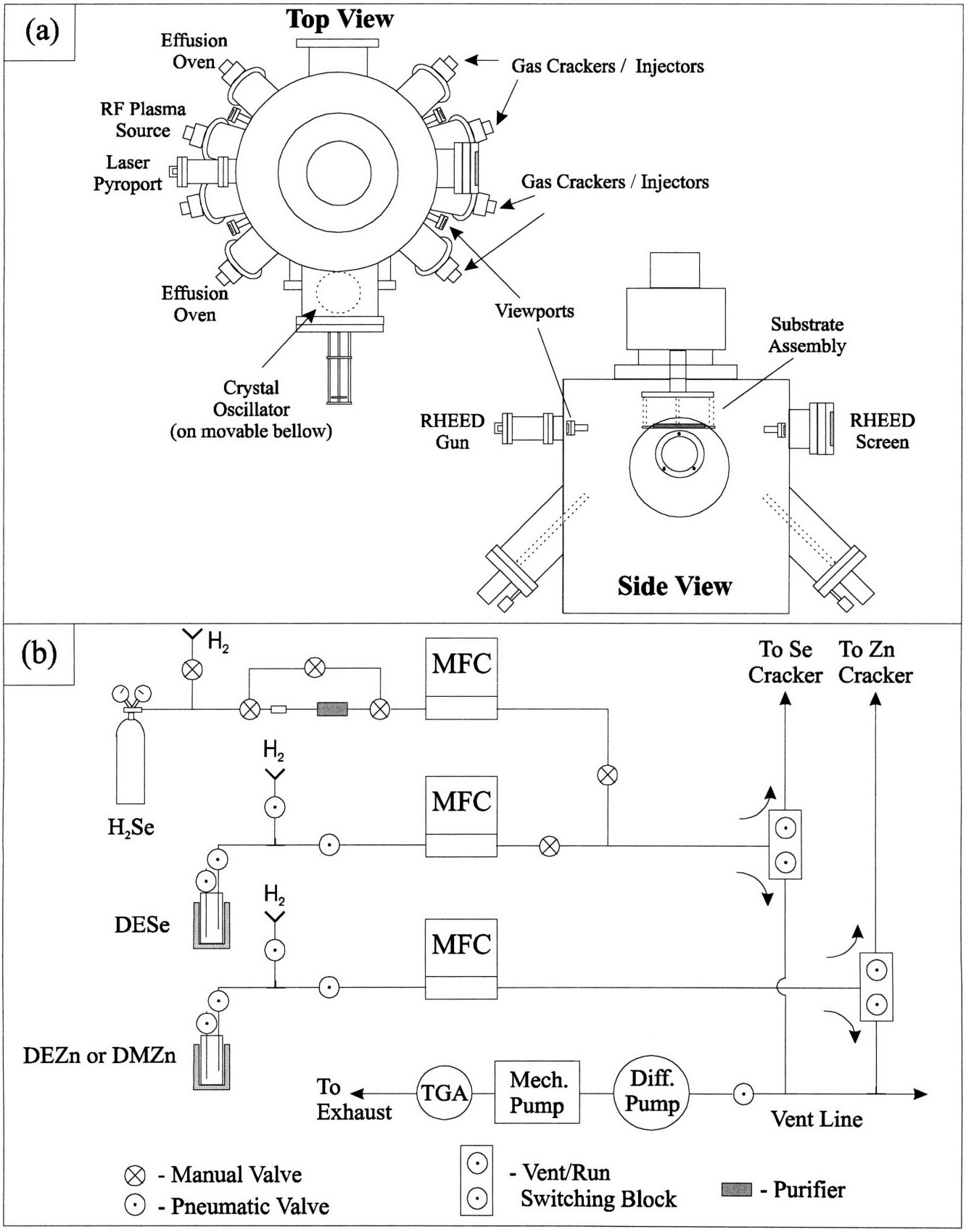

Figure 2–2 Schematic diagram of (a) the MOMBE reactor for the growth of ZnSe; and (b) the gas manifolds for delivery of metalorganic sources.

GaAs wafers of various conduction types were used as the substrates. The substrates were initially degreased in trichloroethane, acetone, and methanol solutions. Degreased substrates were then immediately wet-etched in a 5:1:1 solution of H_2SO_4:H_2O_2:H_2O for 90 seconds, followed by oxide formation in deionized water. The etched substrates were then mounted on the molybdenum holder using high purity indium. A 1-hour bake at 210°C in the transfer chamber was then carried out to remove the residual moisture before introduction into the II-VI chamber. After calibrating the thermal couple reading to the pyrometer reading with the aid of the eutectic, the native oxide of GaAs was removed by heating to ~ 600°C (without the use of an arsenic overpressure) while observing the evolving RHEED pattern. Following oxide desorption, the temperature was then immediately lowered to the growth temperature and allowed to stabilize before initiating growth. Typical gas flow rates of 0.5 - 2.5 SCCM were used for the Group II and Group VI precursors, resulting in chamber pressures of ~ $1x10^{-4}$ Torr during growth. The surface stoichiometry is monitored by observing the RHEED reconstruction patterns during growth, e.g., c(2x2) and (2x1) reconstruction patterns were used to delineate the Zn- and Se-stabilized surfaces, respectively.

2.3 Growth Rate Limitations due to Surface Blockage

Figure 2–3 shows a set of typical RHEED patterns observed immediately after oxide desorption (Figure 2–3(a)), as well as nearing the end of a ~ 1 μm thick ZnSe epilayer (Figure 2–3(b)) in two azimuthal directions. The presence of narrow streaks and the readily apparent Kikuchi bands suggests the existence of single crystalline films having smooth surface morphology. It is worthwhile to note that the typical RHEED patterns observed during MOMBE

(as represented by the photographs in Figure 2–3(b)) are qualitatively similar to those observed during the MBE growth of ZnSe. In this particular case, the presence of the two-fold reconstruction in the <001> indicates that growth is occurring under a cation-rich condition.

Using growth conditions as described above, the MOMBE growth did not proceed as anticipated: in particular, the growth rate was extremely low using DESe and DEZn as sources. Unpublished work [41] on the MOMBE of ZnSe indicated a similar problem in achieving reasonable growth rates. Figure 2–4 shows a plot of the growth rate as a function of the

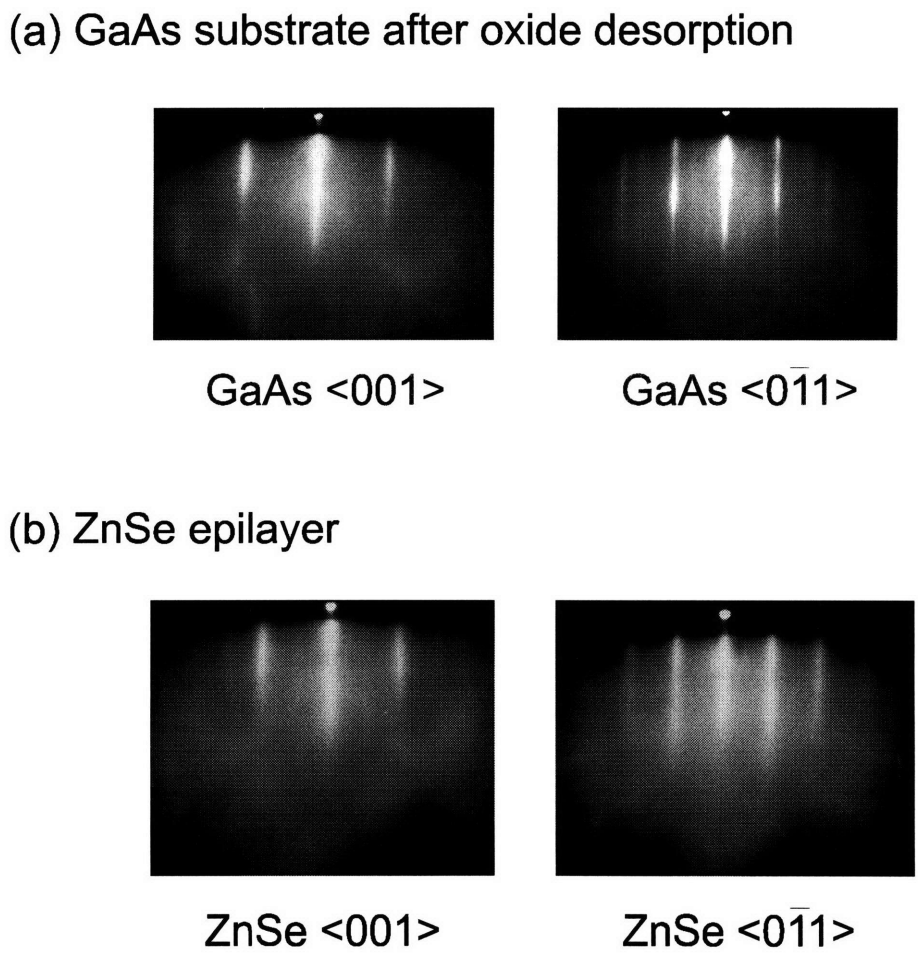

Figure 2–3 Typical RHEED patterns observed (a) after GaAs substrate oxide desorption, and (b) after ~ 2000 Å (unilluminated) of ZnSe grown by MOMBE in the $<001>$ and the $<0\bar{1}1>$ azimuthal directions.

calibrated substrate temperature. Typical growth rates of 100-400 Å/hr were observed *regardless of the growth parameters* when the various combinations of precursor-pairs indicated in the figure legend were used. It is worthwhile to emphasize that Figure 2–4 contains nearly all of our the MOMBE growths carried out at MIT using a variety of growth conditions. The growth parameters that were varied include: substrate temperature, gas flow rate, VI/II flow rate ratio, intentional addition of hydrogen supplied through a gas injector, and the thermal pre-cracking temperature of each precursor by the use of a "cracking" gas injector. For the lowest metalorganic gas flows used, the available amount of zinc and selenium should have yielded a minimum growth rate of ~0.2 μm/hr. QMS analysis of the gas beams confirmed that thermal decomposition of DESe and DMZn occurred at 800 and 1050°C, respectively, whereas DEZn was found to pyrolyze at temperatures greater than 300°C.

Closer scrutiny of the DESe + DEZn growth data, in conjunction with growth experiments carried out using various combinations with elemental Zn, Se and DMZn, provided the following clues: (*i*) the observed low growth rate appeared to be due to a kinetic-limited (as opposed to mass transport-limited) process; and (*ii*) the overall growth rate remained low whenever one ethyl-based metalorganic precursor was used. To ensure that the observed low growth rate was not due to unpyrolyzed DEZn, the DEZn was cracked at 800°C: the growth rate was found to remain very low. Complete avoidance of ethyl-based precursors enabled the growth rate to approach that obtained using a MBE-mode of growth. To further demonstrate that the resultant low growth rate was unique to the use of diethyl-containing metalorganic sources, MOMBE was performed with DMZn (thermally pre-cracked). In this case, the growth rate achieved using DMZn and elemental Se was typical of that achieved in MBE, and limited only by mass transport

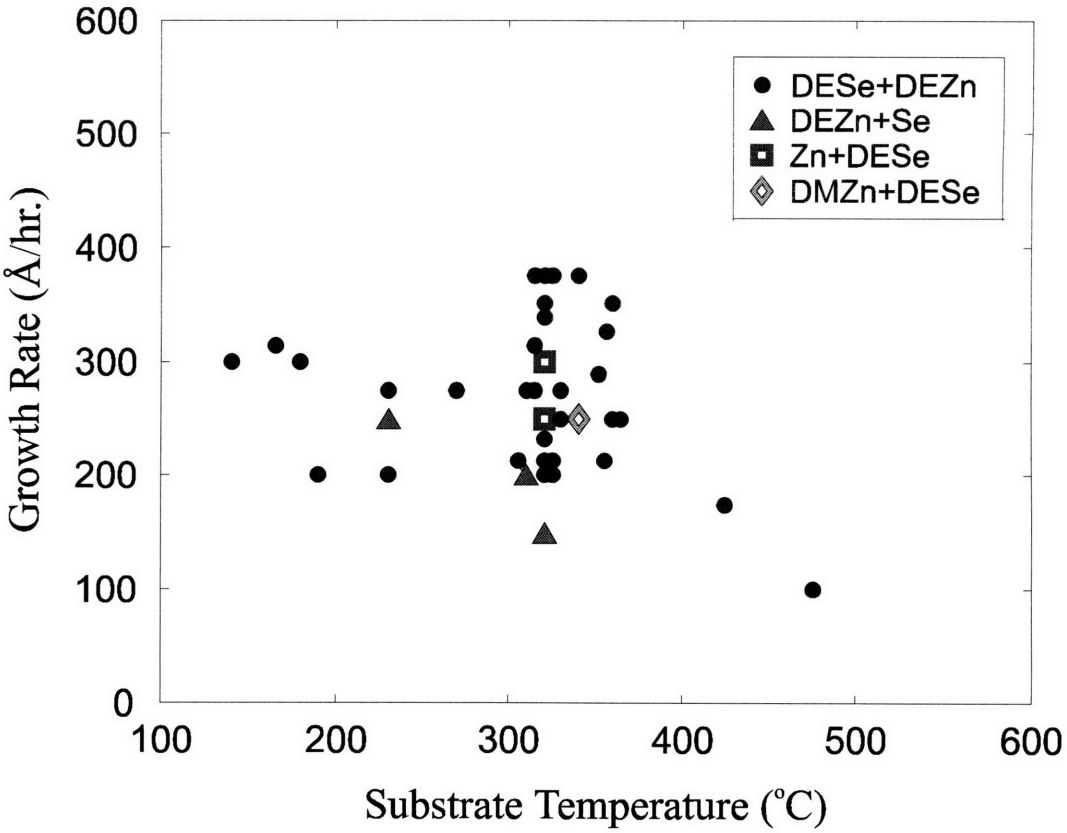

Figure 2–4 Growth rate of ZnSe (using at least one ethyl-based metalorganic source) as a function of the calibrated growth temperature for all the experimental conditions and source combinations investigated.

to the substrate surface. When cracked DESe was substituted for elemental Se for growth with DMZn, however, the growth rate was again very low.

Based on these observations, we postulated that the growth rate was limited by the inability of the zinc and selenium precursors to incorporate into the lattice due to surface site blockage by ethyl-radicals [42,43]. These ethyl-radicals are believed to be strongly chemisorbed on the surface such that incorporation sites for additional metal atoms are not available. Attempts to increase the desorption rate of the ethyl-based species responsible for surface site blockage by increasing the substrate temperatures up to 475°C were unsuccessful, as the resultant growth rate was at the extreme low end (~100 Å/hr). We speculate that whereas the desorption rate of the

ethyl species was not significantly modified at the high substrate temperatures, the desorption of zinc and selenium from the growing surface became significant and dominated the growth. A study of the thermal decomposition of triethylgallium (TEG) on GaAs (100) by Murrell et al. and others [44,45,46] indirectly supported our hypothesis that a surface species was effectively blocking the incorporation sites. Murrell and coworkers observed that TEG decomposition resulted in the formation of highly stable, chemisorbed ethyl species that saturated the surface sites. It was thus suggested that the observed decrease in the growth rate at low temperatures (between 300 - 400°C) in the chemical beam epitaxy of GaAs using TEG and AsH_3 was due to a reduction in TEG adsorption due to site blockage by the stable ethyl species. We believe that a similar mechanism is at work in the case of the MOMBE growth of ZnSe using ethyl-based metalorganic sources as well. Although the use of diethyl metalorganic sources would be expected to be advantageous to enable low temperature growth, they appear to be unsuitable for the growth of ZnSe due to the observed surface site blockage that severely curtails the growth rate. However, as will be described in the next section, we found that the use of DEZn and DESe may actually provide some advantages when one is interested in selective area epitaxy by employing photo- or electron beam-assisted MOMBE growth.

2.4 Beam-Assisted Growth

The use of photon- and electron beam-illumination was found to alleviate the previously mentioned limitation in the growth rate of ZnSe grown by MOMBE. Under the appropriate photon-illumination conditions during growth (i.e., photo-assisted epitaxy), the growth rate was found to dramatically increase by up to a factor of 15 when compared to the unilluminated

growth rates. The effect of photons on the growth was found to be dependent on the power density and energy of the illuminating photons, as well as on the type of precursors employed.

Photo-assisted epitaxy has been reported for the growth of narrow- [47,48,49,50] and wide-bandgap [51,52,42,53,54,55,56,57,58] II-VI materials, as well as for a variety of III-V compound semiconductors [for example, see 59,60,61,62,63,64,65,66,67,68,69]. Several physical mechanisms have been reported or experimentally verified to account for the effect of photon-illumination:

(1) selective modification of the desorption rate of the adsorbed source precursors.

(2) pyrolysis of precursors at the growth front due to a localized increase in the substrate temperature.

(3) direct gas-phase photolysis of the source precursors.

(4) photo-catalysis of the adsorbed molecular species through the creation of free carriers at the growing surface.

Similar effects on the epitaxial growth process have been reported when the surface is illuminated with an electron beam [43,70]. In the electron beam-assisted modification of growth, the physical mechanisms that have been postulated include the kinetically-induced decomposition of adsorbed precursor molecules and the generation of charge carriers that subsequently interact with the surface species. In the photo-assisted epitaxy of II-VI materials, the most common mechanisms were found to be:

(1) photolysis of the source materials (as in photo-assisted MOVPE using light sources tuned to specific absorption lines of the precursors).

(2) modification of the relative desorption rates of the precursor species (as in photo-assisted MBE).

(3) enhanced photo-catalysis of the precursor molecules through the interaction of photo-generated carriers (as in photo-assisted growth of MOVPE and MOMBE).

Photo-assisted growth of MOMBE was performed in our experiments by selectively illuminating a portion of the wafer's surface at a 45° angle to the substrate normal using various optical sources. The laser spot on the wafer was typically an ellipse with major and minor axes of 1.4 and 1.0 cm, respectively. Optical sources that were used include the various emission lines of a 5-Watt Ar ion laser (Spectra-Physics, Model 2025), a Ti:sapphire solid state laser, a tunable organic dye laser containing Coumarin-7 fluorescent dye (pumped by an Ar ion laser), as well as a He-Ne laser. With these sources, a wavelength range between 780 nm to 380 nm was accessible for investigating the wavelength dependence of the photo-assisted phenomenon. The power density was maintained below 200 mW/cm^2 in order to eliminate the possibility of laser-induced local thermal gradients (the rise in the local temperature under such low power densities was calculated to be <1°C [71]). Layer thicknesses (and thus the photo-enhanced growth rate) were measured both by ellipsometry, as well as by surface profiling of a step formed by selectively etching the ZnSe film.

Figure 2–5 shows the growth rate enhancement ratio (defined as the ratio of the illuminated growth rate over the unilluminated growth rate) as a function of the energy of the illuminating photons, using diethyl-based as well as dimethyl-based precursors. For these experiments, DEZn was expected to be pyrolyzed at the surface (substrate temperature was 320°C), whereas DMZn molecules were decomposed in the gas injector (1050°C) prior to arrival at the surface. The enhancement ratios for both metalorganics zinc sources were unity (no enhancement) when photons with energies ($\lambda_{incident}$) less than the energy bandgap (or the energy of interband defect states) at the growth temperature ($\lambda_{bandgap}$) illuminated the surface. Photo-assisted growth with

photon energies greater than the energy bandgap resulted in a nearly constant growth rate enhancement ratio for a given power density. In Figure 2–5, the approximate location of the energy bandgap at the growth temperature for the films grown with DEZn (substrate temperature was 320°C) and DMZn (substrate temperature was 340°C) is indicated with an arrow [58].

These results suggested that photo-generated electron/hole pairs are necessary in order to achieve an increased growth rate. Growth rate enhancement due to gas-phase absorption [72] was ruled out as it is expected to occur at wavelengths much shorter (248 nm for DEZn) than the

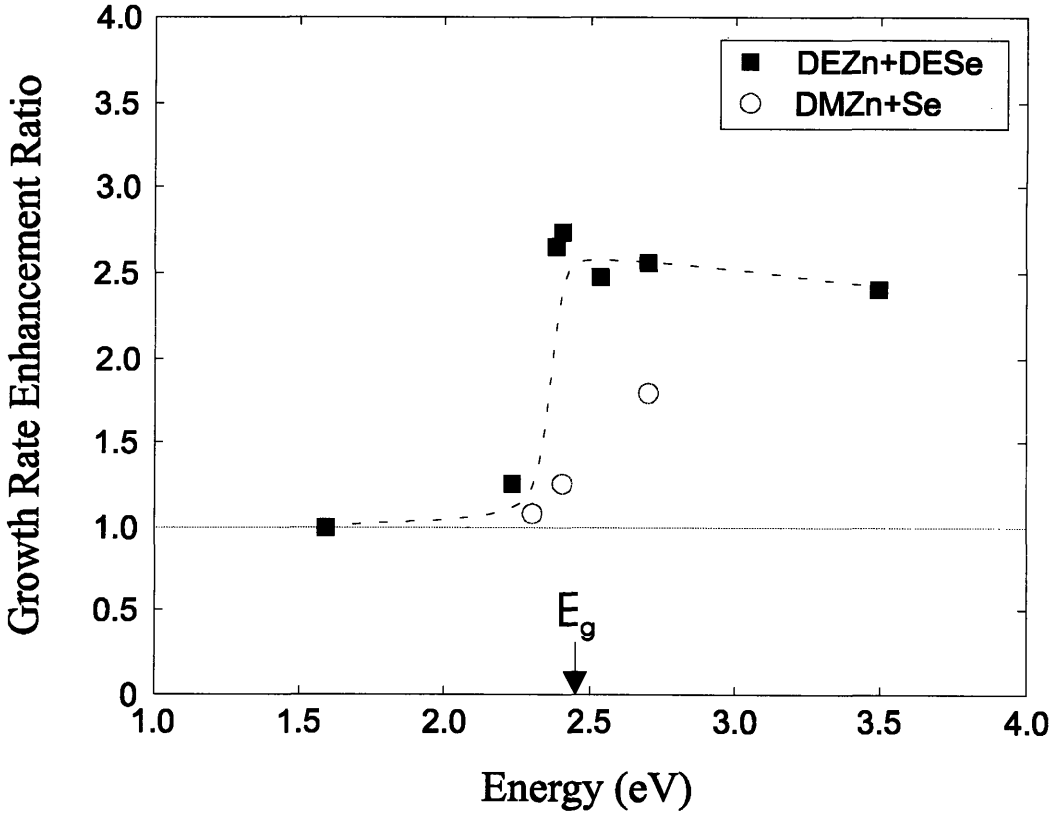

Figure 2–5 Growth rate enhancement ratio (defined as the ratio of the illuminated growth rate over the unilluminated growth rate) as a function of the incident photon energy for two combinations of metalorganic sources. The power density of the illumination for all experiments was kept constant at ~180 mW/cm^2.

wavelength range employed in our experiments. We speculate that photon absorption led to the generation of electron/hole pairs within the ZnSe layer, where the holes drift toward the surface due to band bending. These free carriers were then able to interact with the adsorbed and unpyrolyzed DEZn molecules, leading to the release of the ethyl-radicals which in turn increased the rate of incorporation of Zn.

Figure 2–6 shows a thickness profile of the illuminated region using growth and illumination conditions that led to growth rate enhancement. The resulting thickness profile (and thus the enhancement ratio) was found to be directly proportional to the TEM_{00} mode of the argon ion laser used. Optical interference caused by the large refractive index contrast between the thin ZnSe layer and the GaAs substrate resulted in colorful and dramatic representation of the thickness gradient as a result of localized growth rate enhancement. Although we have not

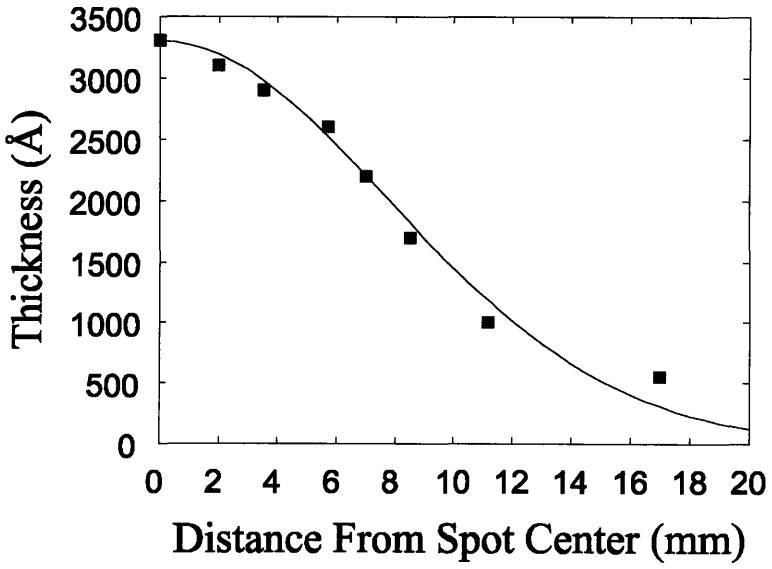

Figure 2–6 Lateral thickness profile of a ZnSe region illuminated with photons having energies greater than the energy bandgap at the growth temperature.

actively attempted to optimize the growth conditions to obtain the highest growth rate enhancement, a factor of 15 increase in growth rate with illumination has been observed. Yoshikawa et al. [73] have suggested a similar growth rate enhancement mechanism observed during photo-assisted MOVPE growth of ZnSe. In their case, the photo-generated carriers in the ZnSe layer participate in oxidation and reduction reactions with the adsorbed and unpyrolyzed metalorganics to increase the growth rate. The most important difference (when compared with our MOMBE results) is that while the photo-assisted MOVPE growth of ZnSe primarily allows the ZnSe to be grown at lower substrate temperatures with illumination, mass-transport-limited growth of ZnSe was not possible at any substrate temperature using MOMBE without the use of photon- (or as will be described later, electron-) illumination.

In order to determine the precursor species most strongly affected by the photo-generated carriers, elemental Zn and Se were also used in photo-assisted growth experiments along with metalorganic precursors (DEZn, DMZn and DESe) that were introduced either "cracked" or "uncracked". Table 2-1 tabulates the results of these series of experiments. As can be expected, the use of uncracked DESe with any Zn precursor resulted in no appreciable growth, as DESe is highly stable and remains unpyrolyzed over the range of growth temperatures used here. On the other hand, as long as uncracked DEZn was used with any Se precursor, a significant growth rate enhancement was observed with above-bandgap illumination. When both Zn and Se elemental sources were used, illumination using photon energies sufficient to generate electron/hole pairs resulted in growth rate suppression (i.e., the growth rate decreased with illumination). This phenomenon has been observed in photo-assisted MBE growth of ZnSe that led to growth rate suppressions [56], the magnitude of which was consistent with our MOMBE results based on a comparison of the respective power densities used. When DMZn was used as the Zn precursor,

Table 2-1 Comparison of Growth Rates of ZnSe Grown by MOMBE with Photo-Irradiation

Source of Zn	Source of Se	MOMBE Growth Rate[a]	Effect of Illumination on Growth Rate
DEZn	DESe	No Growth	None
DEZn	cracked DESe	Low	Enhancement
cracked DEZn	cracked DESe	Low	Suppression
elemental Zn	cracked DESe	Low	Suppression
DEZn	elemental Se	Low	Enhancement
elemental Zn	elemental Se	High	Suppression
cracked DMZn	cracked DESe	Low	Enhancement
cracked DMZn	elemental Se	High	Suppression or Enhancement

[a] Low: 200 - 400 Å/hr. High: typical of MBE

low growth rates were still obtained using DESe; however, normal growth rates were observed when elemental Se was used (i.e., no diethyl precursors involved). The transport-limited mode of growth observed with the combination DMZn + elemental Se indicated that the significant site blockage phenomenon is associated primarily with the ethyl-containing precursors.

The photo-assisted growth behavior of DMZn + elemental Se is more complicated due to the necessity for pre-cracking of DMZn: both growth rate enhancement and suppression were observed. In general, lower cracking temperatures led to the observation of growth rate enhancement; while higher DMZn cracking temperatures resulted in growth rate suppression similar to photo-assisted MBE. We were not able to clearly discern the mechanism that is at

work involving DMZn because of the insufficient number of experiments that were carried out. Notice that the use of DMZn + Se combination was intended for verification of the site-blocking problem only: use of elemental Se negates the primary aim of the MOMBE technique in replacing the high vapor pressure sources with gaseous ones. Optical characterization of films grown with DMZn + Se further indicated the presence of persistent deep levels that might be caused by undesirable impurities in the DMZn sources.

Optical characterization of the ZnSe films grown by MOMBE (both with and without laser assistance) was carried out by low temperature photoluminescence (PL). Typical 10K PL spectra of unilluminated regions were dominated by a broad peak centered at ~2.25 eV with weaker excitonic features near the band-edge, suggesting that the film may be highly non-stoichiometric. Regions illuminated by above-bandgap radiation, however, showed a sharp excitonic feature without prominent emission from the deep levels. Figure 2–7 shows the PL collected from a ZnSe layer grown (a) without and (b) with laser illumination. The effect of the laser illumination during growth is dramatically evident. The unilluminated film (1100 Å thick) is dominated by a broad deep level; the illuminated region (3500 Å thick) exhibits an intense donor-bound exciton peak at 2.799 eV with negligible deep level emission.

The strong effect of the laser on the PL properties of ZnSe can be consistently explained by the increased availability of Zn for incorporation as induced by photon illumination. The amount of useful Zn precursor made available by photon-illumination effectively allows one to effectively "tune" the surface stoichiometry. Under conditions where the illuminated regions exhibit desirable PL spectra one would expect an approximately 1:1 surface stoichiometry. Therefore, it is reasonable to expect that the non-illuminated regions are highly Zn-deficient and defective as observed by photoluminescence.

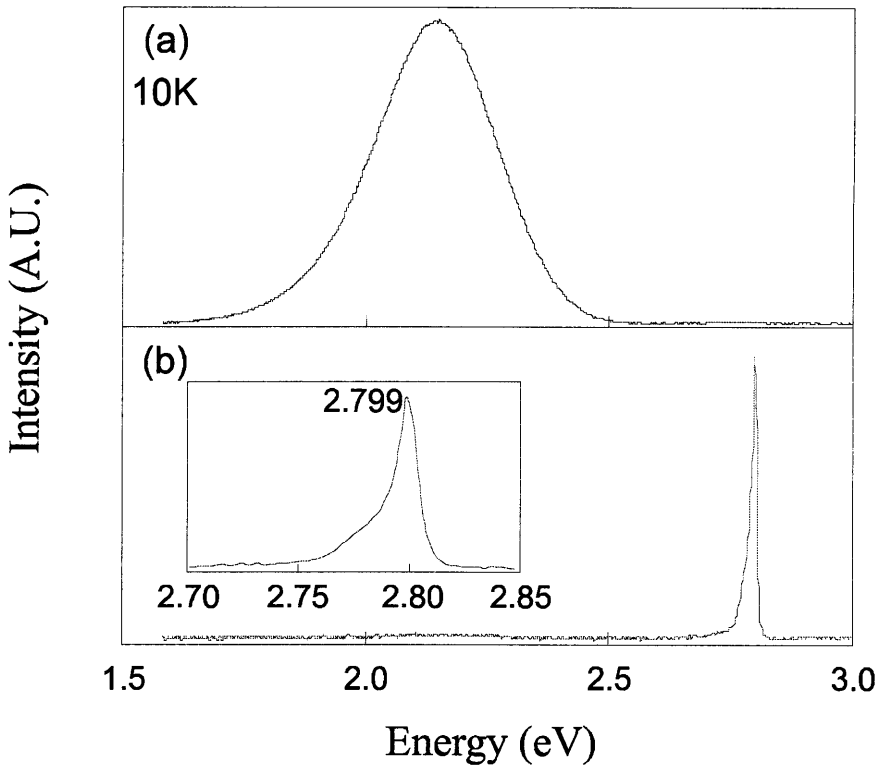

Figure 2–7 Photoluminescence of (a) ZnSe grown using DESe + DEZn without photo-irradiation; and (b) regions illuminated with above-bandgap photons along with an inset emphasizing the near-bandedge portion of the spectrum.

We further observed that a similar growth rate enhancement/suppression was possible when a high energy (typically 10 kV) electron beam was incident on the substrate during the MOMBE growth of ZnSe. The RHEED electron gun provided a convenient source of electrons that can be focused or defocused at will. Since RHEED was usually utilized throughout the duration of a growth experiment, the electron-beam irradiated areas exhibited variations in thickness. The magnitude of electron beam-assisted growth rate modification was found to be dependent on the flux of the incident electron beam, as well as the amount of unpyrolyzed DEZn species present at the surface. The electron beam-assisted growth behaved qualitatively similar to photo-assisted growth when $\lambda_{incident} > \lambda_{bandgap}$: i.e., growth conditions that led to photo-assisted growth rate

enhancement (or suppression) also led to electron beam-assisted growth rate enhancement (or suppression). Takahashi et al. [70] have reported growth rate enhancement in the MOVPE of GaAs using trimethylgallium (TMG) and arsine with a focused, high energy (40 kV), electron beam. In this case, the authors believe the enhancement mechanism to be kinetically-induced decomposition of adsorbed TMG by the incident electron beam; that speculation is supported by the presence of very high levels of carbon incorporation in their films. In the work of Takahashi et al. [70], the growth of the GaAs was performed at temperatures considered to be very low and in some cases at room temperature. Secondary ion mass spectroscopy (SIMS) measurements of our ZnSe films, however, failed to find an elevated level of carbon regardless of the electron beam illumination conditions. These observations suggest that the growth rate enhancement mechanism for ZnSe grown with electron beam illumination is most likely not kinetically-induced. A slightly elevated carbon concentration localized about the ZnSe/GaAs interface can be seen in some samples, but is believed to be carbon residue as a result of the substrate preparation procedure.

Based on the similarity between photo- and electron beam-assisted growth behaviors, a likely mechanism for the observed electron beam-induced effect was the generation of electron/hole pairs as electrons decelerate in the ZnSe layer. These electron/hole pairs then interact with the adsorbed (and unpyrolyzed) DEZn and DMZn in mechanisms similar to photo-generated carriers. The fact that blue emission has been observed by electron beam illumination during conventional MBE growth further supports this hypothesis. Characterization of the irradiated regions of the ZnSe layers has not been thoroughly performed due to the typically small (1-2 mm) regions that were obtained. Both growth rate enhancement mechanisms described here, e.g., photo- and electron beam-assisted growth, can be applied in the selective

area epitaxy of ZnSe. Optical imaging or shadow mask methods can be used with photo-irradiation to define patterns *in-situ*. Similar to electron beam lithography, selective area epitaxy consisting of very fine lines of ZnSe material can potentially be achieved by rastering an incident electron beam.

2.5 Summary

MOMBE growth of ZnSe using DEZn and DESe has been performed on GaAs substrates. These precursors were initially chosen for their low thermal pyrolysis temperature which enables low temperature growth. However, the use of these ethyl-based metalorganics were found to generate ethyl-containing radials that effectively reduce the incorporation rate such that the useful growth rate was only several hundred angstroms per hour. In order to elucidate the nature of the surface blockage, both elemental Zn, Se, and DMZn were used in conjunction with DEZn and DESe under photo- and electron beam-illumination. Using photo- as well as electron beam-illumination under the proper conditions were found to locally eliminate the surface blockage problem such that the illuminated growth rates are increased by over an order of magnitude. Photons with energies greater than the bandgap of ZnSe at the growth temperature were observed to increase the growth rate over the unilluminated counterparts by over 1500%. A 10 KV electron beam introduced during growth at a glancing angle was also found to result in a substantial increase in the growth rate. Although the detailed kinetic reaction involving the ethyl-radical culprits and the electron-hole pairs could not be identified, we believe that these electron-hole pairs generated by the two illumination mechanisms participate in the surface reaction leading to enhanced incorporation of partially pyrolyzed DEZn species and the liberation

of ethyl-species. The free carriers at the surface may provide an anti-bonding mechanism for the alkyl radicals such that the radical is released from the Zn-precursors. These results are consistent with the observation that a significant growth rate enhancement was observed whenever unpyrolyzed DEZn exists on the surface, while laser-induced growth rate suppression is observed when cracked DEZn is used with DESe.

SIMS measurements also indicated that a significant level of carbon incorporation in the region illuminated by the laser or electron beam was not observed. PL measurements suggest that laser-irradiation can substantially improve the optical quality of the ZnSe epilayer. Although the use of the DEZn and DESe sources may not be optimal for normal MOMBE growth of ZnSe due to the requirement of large area illumination, laser- and electron beam-assisted growth can provide opportunities to take advantage of the selective area epitaxy potential for the II-VI family of materials.

3. GSMBE Growth and Doping of ZnSe

3.1 Advantages and Disadvantages of GSMBE

Gas source molecular beam epitaxy (GSMBE) is an alternative gaseous source epitaxial growth method that replaces the high vapor pressure elements in the MBE method with hydride sources that are amenable to regulation using a precision mass flow controller. For examples, AsH_3, PH_3 and H_2Se are used in place of elemental As, P, and Se, respectively, thus greatly reducing the associated problem of flux control. Lower vapor pressure elements such as Ga, In, and Zn are used as effusion sources. GSMBE retains most of the UHV advantages of MBE while avoiding the use of metalorganic precursors, which circumvents the issues of source purity and carbon incorporation. Hydride sources are available with very high purity (p.p.m. impurity levels can be obtained) because of their chemical simplicity. This simplicity in source materials also translates directly into a much simpler array of growth chemistries as compared to MOVPE, and results in easier control and prediction of the epitaxial growth process. The use of a gas cracker for the hydride sources, however, does allow for an additional degree of freedom in controlling the form of the precursors provided to the growing surface. For example, in the GSMBE growth of InP, the dimer molecules produced by cracking the PH_3 are known to have a higher sticking coefficient than the tetramer molecules normally produced by an effusion source of solid phosphorous. Several tradeoffs, however, are involved when using the GSMBE method. First and foremost is the use of highly toxic hydrides that necessitate the use of sophisticated gas monitoring equipment, and extreme care in the daily operation and exhaust handling. Since the

thermal dissociation of the hydrides generates a large amount of the by-product H_2, the pumping requirements are essentially that of MOMBE. The frequency of required source replenishment is now dictated by the elemental sources and is no longer completely *ex-situ*. Overall, the GSMBE method represents a best-case compromise that strives to achieve a balance between (*i*) the necessity of using a gaseous source to control the high vapor pressure elemental constituents, and (*ii*) the desire to keep source materials and the reactions involved as simple as possible.

Another unique aspect of GSMBE is the copious and unavoidable generation of H_2 and sub-hydride species (such as As-H and Se-H). Whether these H_2 and sub-hydride species are beneficial or deleterious depends on the material system involved. In the growth of III-V materials, the presence of hydrogen radicals has been postulated to aid in the removal of residual carbon inadvertently introduced into the vacuum system [74,75]. However, electrical passivation of both intentional and un-intentionally introduced dopants has been frequently observed in the growth of Si and III-V compound materials. In these cases, annealing at modest temperatures was usually sufficient to reverse the hydrogen passivation effects. As will be shown later in this section, however, hydrogen plays a central role in the growth and doping of ZnSe by GSMBE, particularly when nitrogen doping is involved.

3.2 Experimental Procedures

Ultra-high purity (6N) Zn and Se, as well as H_2Se (5N) gas, were employed as precursors for the GSMBE growth of ZnSe. The H_2Se gas was thermally decomposed in an EPI high-temperature hydride gas cracker at temperatures ranging from 600-1100°C with the typical cracking temperature usually set at ~1000°C. The cracking tube is composed of a pyrolytic

boron nitride (PBN) tube capped with a tantalum end baffle having an exit aperture of ~0.7 cm in diameter. The PBN cracking tube assembly also contained a significant amount of internal Ta baffling.

ZnSe epilayers were usually grown on 0.5 - 0.75 μm epitaxial GaAs buffer layers grown on (100) GaAs epi-ready substrates. Earlier GSMBE growths employed GaAs wafers that were chemically etched and In-bonded to molybdenum holders. Wafers prepared in this manner was found to consistently give satisfactory RHEED patterns after oxide desorption, but were prone to seemingly unpredictable particulate contamination problems. A possible cause seems to be the process of excess indium removal around the wafer by scraping. Another shortcoming of this method is that the emissivity setting tended also to depend on the amount of indium as well as the manner in which the wafers were bonded, making temperature calibration less repeatable. Later growths were performed on indium-free substrate holders using full 2" epi-ready wafers from AXT Crystal, Inc. The reduced wafer handling was found to substantially improve the morphological defects that were believed to be caused by particulates. One trade-off that had to be contended with was the inability to use eutectic chips when full 2" GaAs wafers were used. However, this is fortunately mitigated by the decrease in the number of variables that can affect the heating characteristics of the substrate holder assembly, leading to reduced discrepancy between the thermal couple and the pyrometer readings. A relatively wide range of growth temperatures (between 250-370°C) have been explored using GSMBE in this study.

The buffer layers were grown in our UHV-interconnected GSMBE reactor dedicated to III-V materials, and transferred into the II-VI reactor *in-situ* without surface passivation. As part of our II-VI/III-V heterostructure research effort (which is described in more detail in the next chapter), various other ternary and quaternary compounds of (In,Ga,Al)P and (In,Ga)As have also been

investigated as epitaxial buffer layers. These buffer layers can be flexibly designed to provide lattice-matched "pseudo-substrates" having the lattice parameters of ZnSe, GaAs, as well as a wide range of (Zn,Mg)(S,Se) quaternary layers. Undoped GaAs and p-type GaAs:Be are by far the most common epitaxial buffer layers used in this study.

The n-type dopant source was solid $ZnCl_2$ (5N purity) contained in an effusion oven whose temperature typically ranged between 150-300°C. Either a cryogenically-cooled (Model CARS25) or a water-cooled (Model MPD21) RF plasma source from Oxford Applied Research was used as the nitrogen dopant source for acceptors. The plasma source is supplied with ultra-high purity nitrogen and hydrogen gases (ULSI grade, 5N purity). The nitrogen flow rate was monitored by an ionization gauge within the reactor (prior to the introduction of the H_2Se gas). RF powers ranging between 200 and 500 W have been used. The plasma emission intensity was monitored using a photodiode coupled to the interior of the quartz plasma chamber via an optical fiber. The exhaust temperature was regulated between -30 to -50°C in the cryogenically-cooled plasma source. Various aperture configurations have been used and resulted in nitrogen flows that produced chamber pressures between $5x10^{-7}$ and $2x10^{-5}$ Torr under the high brightness plasma mode of operation [76]. The surface stoichiometry was normally maintained near one-to-one for the Zn and Se fluxes as monitored by RHEED during nitrogen doping.

Film thicknesses were usually monitored *in-situ* using pyrometer temperature oscillations [77] and confirmed by selective etching and profiling of partially-masked ZnSe films. The pyrometer oscillation signals (caused by optical interference of blackbody radiation in the range of 2.0-2.6 μm between the low index ZnSe and the high index GaAs) provide a convenient real-time method for thickness monitoring. Together with the initial RHEED intensity oscillation information, thickness control of the ZnSe epilayer can be easily achieved. As an example,

Figure 3–1 below shows a typical pyrometer oscillation trace as a function of the elapsed growth time.

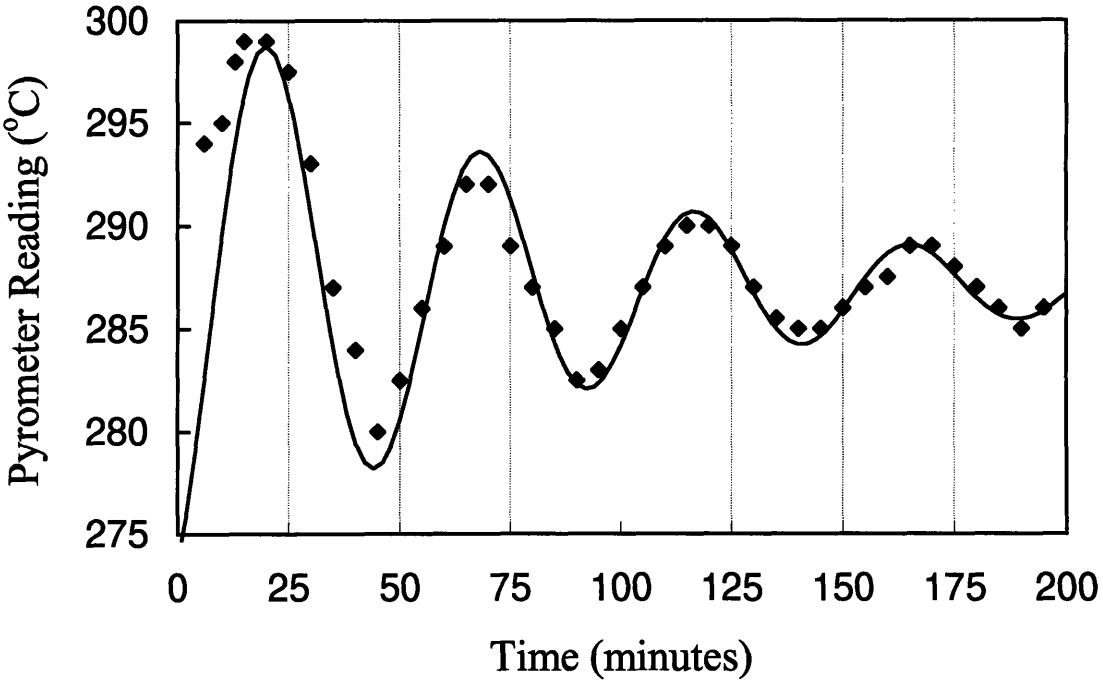

Figure 3–1 Pyrometer oscillation signals for ZnSe grown on epitaxial GaAs. The solid line is a damped sinusoidal function approximation to aid in the determination of the oscillation period.

Routine post-growth characterization of the as-grown films included Nomarski microscopy, PL, SIMS, as well as capacitance-voltage (C-V) measurements and Hall effect measurements (for n-type ZnSe). SIMS analyses (see Appendix A for a more detailed description) were primarily performed on Au-coated samples at Charles Evans & Associates using Cs^+ as the primary ion. The typical primary ion raster size was 150x150 μm^2, with the secondary ions collected from a circular image area of ~ 30 μm in diameter. Electron-beam flooding was employed in all measurements in order to minimize sample charging. Impurity concentrations were calibrated

using implanted nitrogen and deuterium profiles in ZnSe epilayers of known dosages and implantation energies. Two device geometries have been employed for the C-V measurements (please see Appendix B for a more detailed discussion of the C-V method and measurement geometries) depending on the conductivity type of the GaAs substrate and buffer layers. Lateral double-Schottky diodes were used for conductive ZnSe films grown on semi-insulating GaAs substrates. For ZnSe:N grown on p-type GaAs (with p-type GaAs:Be buffer layers), 500 μm-diameter Schottky contacts (Cr/Au) were used for measurement at 10 kHz. Typical ZnSe:N and ZnSe:Cl film thicknesses for electrical measurements were ≥ 2 μm.

Figure 3–2 shows RHEED photographs of: (a) a typical starting GaAs:Be epitaxial buffer layer after transfer into the II-VI chamber, and (b) ZnSe pattern near the end of GSMBE growth in two azimuthal directions. As shown in Figure 3–2(a), the *in-situ* transferred GaAs buffer layer exhibits sharp and streaky reconstruction patterns, indicating that the starting surface is monolayer-smooth. RHEED intensity oscillations were observed in nearly all cases of ZnSe growth on epitaxial GaAs buffer layers, indicating that the initial growth of ZnSe was proceeding in a two-dimensional, monolayer-by-monolayer fashion. The resultant ZnSe epilayer also showed well defined and streaky RHEED pattern (Figure 3–2(b)) at the conclusion of growth. These typical RHEED patterns of GSMBE growth films compare favorably to ZnSe films grown by conventional MBE under similar growth conditions.

Figure 3–3 shows a set of RHEED intensity oscillation traces for an undoped ZnSe epilayer grown by GSMBE on a 0.75 μm GaAs epitaxial buffer layer (c(4x4) reconstructed) and nucleated under ~ 1:1 stoichiometry with Zn pre-exposure. Over 100 RHEED intensity oscillation cycles have been recorded for GSMBE-grown ZnSe on epitaxial GaAs buffer layers.

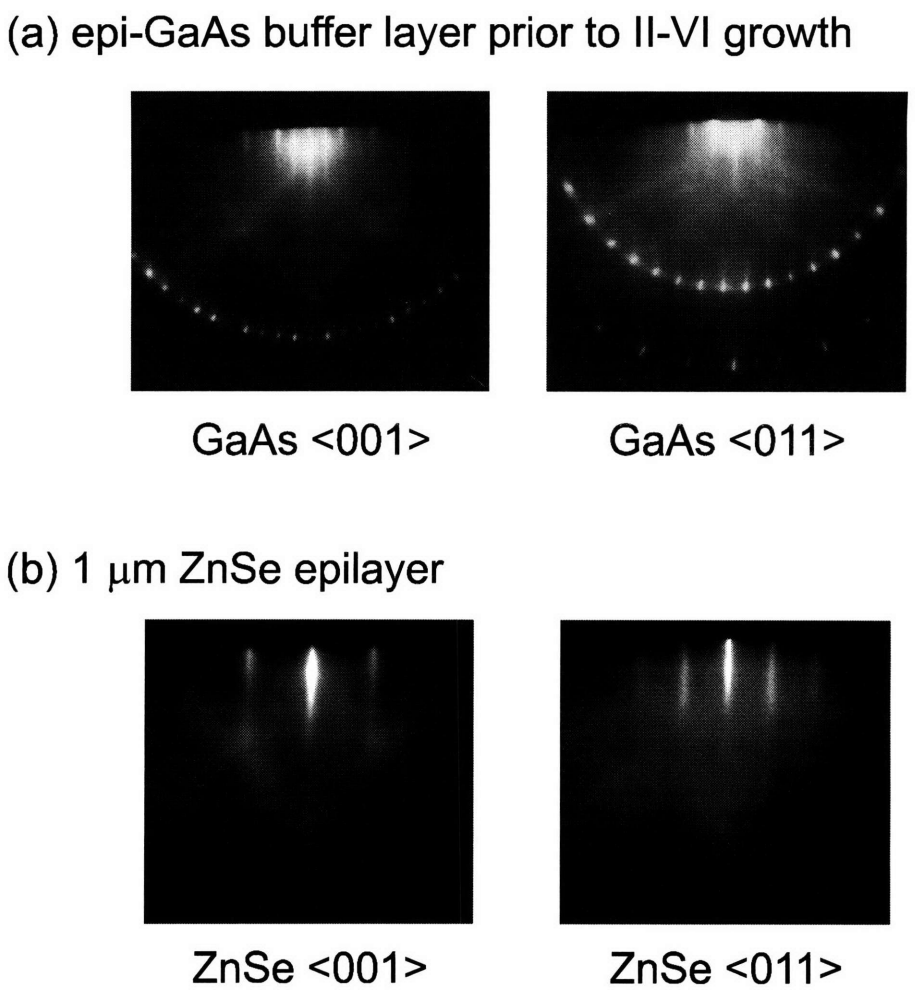

Figure 3–2 (a) RHEED patterns of epitaxially grown GaAs just before nucleation of the ZnSe layer in the II-VI chamber; (b) RHEED pattern of ZnSe just before the end of a 1 μm ZnSe epilayer.

PL spectra were measured by exciting the samples with the 325 nm line of a focused He-Cd laser, providing a power density of approximately 300 mW/cm^2. The samples' luminescence was analyzed using a 0.5 m spectrometer and a photomultiplier tube. As an example of the optical properties exhibited by GSMBE-grown ZnSe, Figure 3–4 shows the PL spectrum obtained from an 1.1 μm thick, undoped ZnSe layer grown on a InGaP buffer layer nominally lattice-matched to the GaAs substrate [78]. For the entire range of growth temperatures investigated, the low temperature (10 K) PL spectrum of undoped layers was typically dominated

by an intense donor-bound exciton feature (I_2) having an energy of 2.798 eV. As can be seen in Figure 3–4, the spectrum is dominated by a donor-bound transition and a free exciton (E_x) transition having nearly equal intensity. The Y_o transition at 2.602 eV and the I_v^o transition at 2.775 eV have been attributed to excitonic recombinations on extended defects, and are typically only observed in high purity ZnSe epilayers [79,80,81,82]. The transition at 1.938 eV is due to emission originating from the (In,Ga)P buffer layer. Based on the PL peak energy and SIMS analyses of the films, we speculate that the unintentional donor impurity was chlorine. The deep level defect-related luminescence band, which is broadly centered about 2.25 eV, is typically at least 100-1000X weaker in intensity than the near-bandedge features.

To elucidate the presence of the defect-related luminescence, photoluminescence was also obtained at 77K for films grown at various substrate temperatures. Figure 3–5 shows the 77K PL spectra for undoped ZnSe films as a function of the substrate temperature. The donor-bound exciton, I_2, remained as the dominant feature. A small amount of luminescence originating from deep levels was observed only at the growth temperature extremes examined in our experiments.

As another indication of the high quality of the ZnSe layers, the integrated PL intensity of the near-bandedge feature was found to decrease to only one-sixtieth of its 10 K value as the sample temperature was increased to room temperature. At room temperature, blue-green luminescence was easily observed by the naked eye.

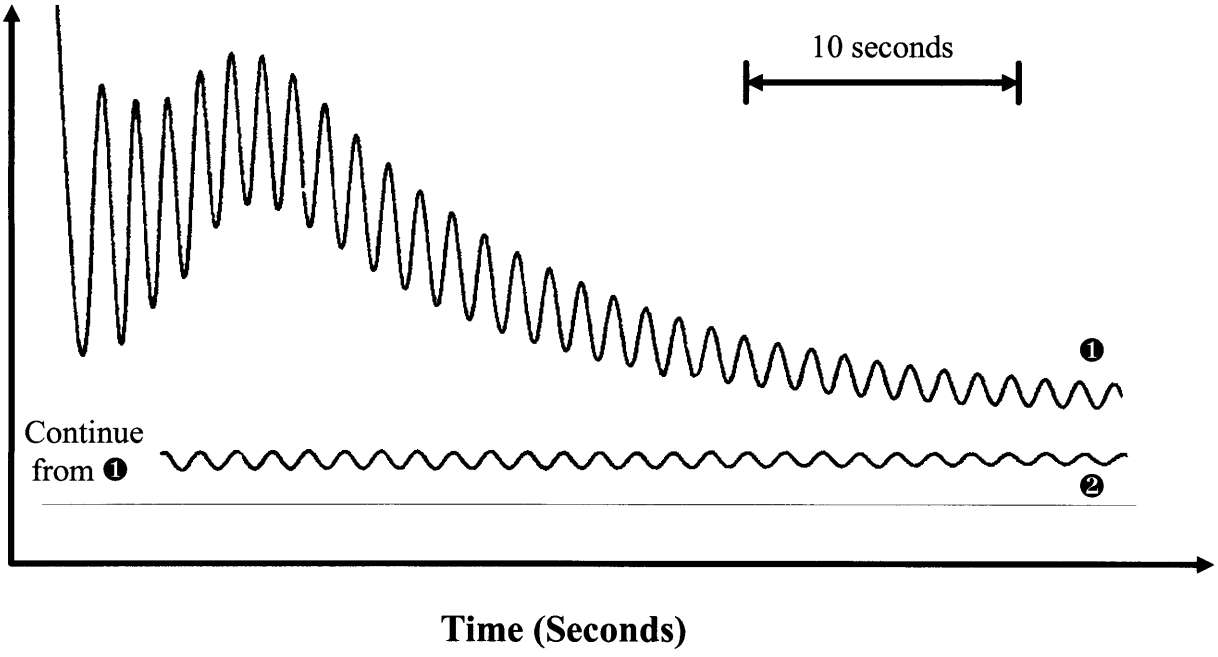

Figure 3–3 RHEED intensity oscillation trace of ZnSe nucleated on c(4x4) epitaxial GaAs buffer layer. The vertical intensity scale is in arbitrary units. The H_2Se cracking temperature was 600°C with 90 seconds of Zn flux pre-exposure before the ZnSe nucleation.

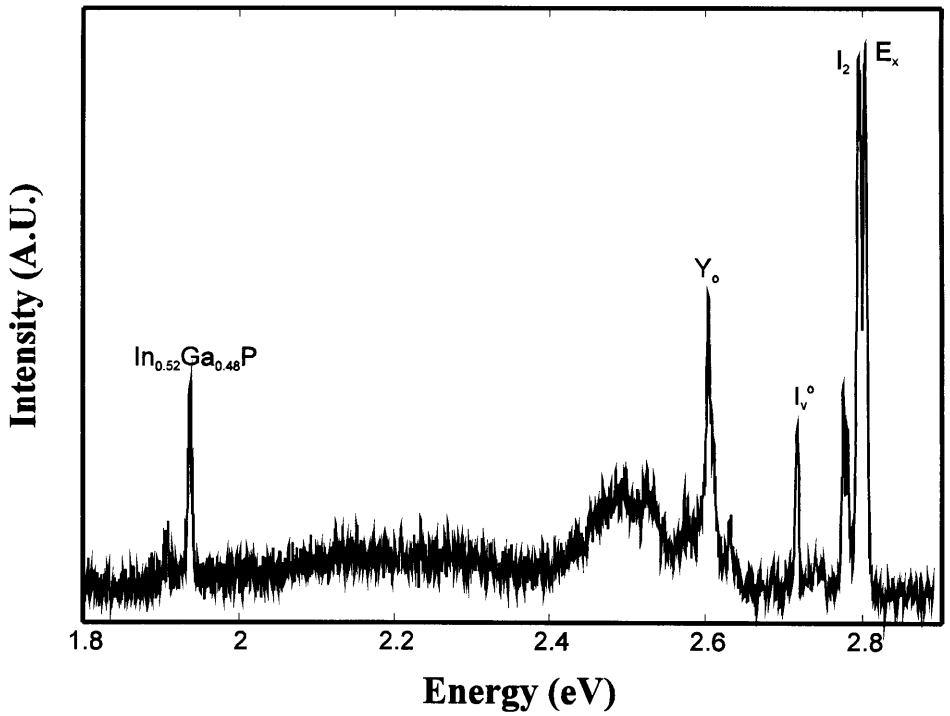

Figure 3–4 Photoluminescence of undoped ZnSe (~1.1 μm) grown on $In_{0.52}Ga_{0.48}P$ (partially relaxed, 4.3 μm) epitaxial buffer layer grown on GaAs. The feature at 1.938 eV is attributed to the luminescence from the $In_{0.52}Ga_{0.48}P$ buffer layer. Features at 2.803, 2.795, 2.776, and 2.603 are identified as the E_x, I_2, I_v^o, and Y_o, respectively.

In order to establish the background carrier type and concentrations in unintentionally-doped ZnSe, Hall effect measurements were carried out at room temperature. The Van der Paaw geometry was used for the measurement, with indium employed as the ohmic contact metal. All unintentionally-doped films were found to be lightly n-type; the free electron concentrations ranged from the mid 10^{15} cm^{-3} to the low 10^{17} cm^{-3}, and appeared to be influenced by the surface stoichiometry during growth. Slightly Zn-rich conditions (as opposed to Se-rich conditions) have been previously found to give rise to: (*i*) PL spectra exhibiting a stronger free-exciton feature, and (*ii*) a lower unintentionally-doped free electron concentration as determined using Hall effect measurements [83].

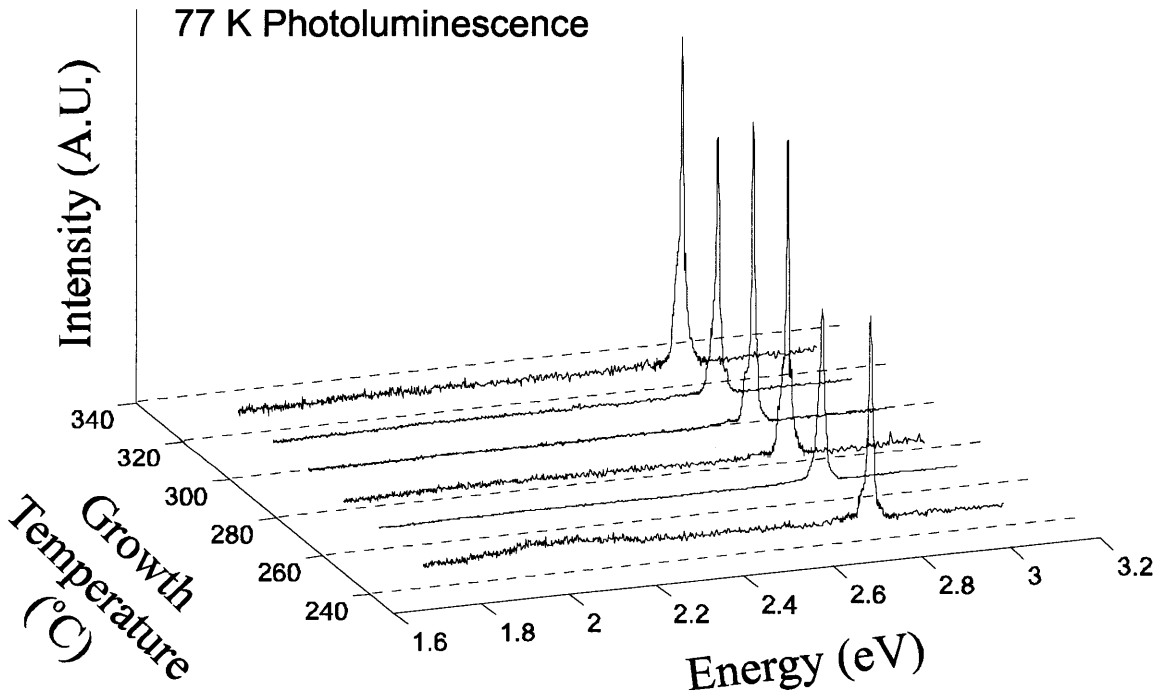

Figure 3–5 The 77K photoluminescence intensity as a function of energy for ZnSe epilayers grown at various substrate temperatures. The ZnSe film at a growth temperature of 284 °C was grown on an (In,Ga)P buffer layer. The spectra are dominated by donor-bound exciton (I_2) features at 2.790 eV.

3.3 N-type Doping Using $ZnCl_2$

Chlorine has been fairly well investigated in the context of n-type doping of ZnSe using the conventional MBE technique. Cl-doping using $ZnCl_2$ was found to be an effective method to obtain shallow n-type dopant for ZnSe, as well as for the wider bandgap (Zn,Mg)(S,Se) materials [84,85,86]. In our experiments, solid, anhydrous $ZnCl_2$ was used in an effusion source in order to achieve straightforward n-type ZnSe using GSMBE. Figure 3–6 shows the behavior of $ZnCl_2$ effusion source as a n-type dopant. The chlorine concentrations (hereafter denoted [Cl]) and growth rates were determined as a function of the $ZnCl_2$ effusion cell temperature, with all other growth parameters held constant. As shown in the top portion of Figure 3–6 (left vertical axis),

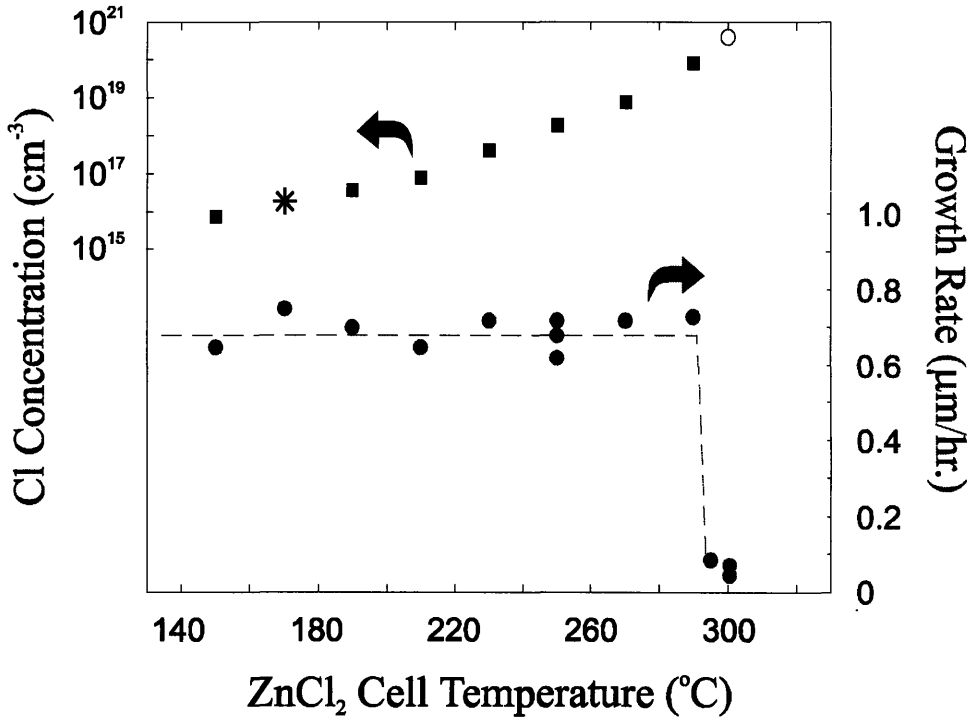

Figure 3–6 Growth rate and chlorine concentration as a function of the $ZnCl_2$ cell temperature for ZnSe:Cl grown by GSMBE. The open circle at a cell temperature of 300 °C is an extrapolated value. "*" denotes a carrier concentration from Hall effect measurements.

the chlorine concentration was found to increase with $ZnCl_2$ oven temperature in a well-behaved manner. In Figure 3–6, the [Cl] was primarily measured by means of SIMS for [Cl] values greater than the detection limit of Cl (~10^{17} cm^{-3}), whereas the free electron concentration obtained from Hall effect measurements were used for lower chlorine concentrations. For chlorine concentrations ranging from the low to the middle 10^{18} cm^{-3}, the free electron concentrations (as measured by Hall effect measurements) as well as $[N_D-N_A]$ values obtained from C-V measurements, all agree within the accuracy of the respective measurement techniques involved. For $ZnCl_2$ oven temperatures from 150 to 290°C, the [Cl] varied from $9x10^{15}$ to $8x10^{19}$ cm^{-3}, while the growth rate remained essentially constant as indicated from the bottom portion of Figure 3–6 (right vertical axis). At the heavily-doped extreme, however, an abrupt change in the growth rate was observed for effusion cell temperatures beyond 300°C. The mechanism for this phenomenon is presently unknown, but the sharp transition suggests the possible formation of a separate chemical phase involving the large [Cl] at the surface. These chlorine levels are comparable to the highest levels reported in n-type doped films grown by conventional MBE, or by MBE employing a selective planar doping technique [86].

The PL spectra of several ZnSe:Cl films are shown in Figure 3–7 as a function of increasing [Cl]. For doping levels resulting in [Cl] as high as $4x10^{18}$ cm^{-3}, the spectra were dominated by a single intense I_2 (donor bound exciton) transition. Negligible defect-related deep level emission was observed (at 100X magnification), which is indicative of the high crystalline quality of the doped films. The intensity of the I_2 feature increased as the [Cl] was increased and exhibited a maximum in intensity for a [Cl] of $1x10^{17}$ cm^{-3}. The I_2 intensity decreased as the doping level was increased further. At a [Cl] of $8x10^{19}$ cm^{-3}, the donor-bound exciton feature was no longer present, and the spectrum became dominated by a broad band of deep level emission extending

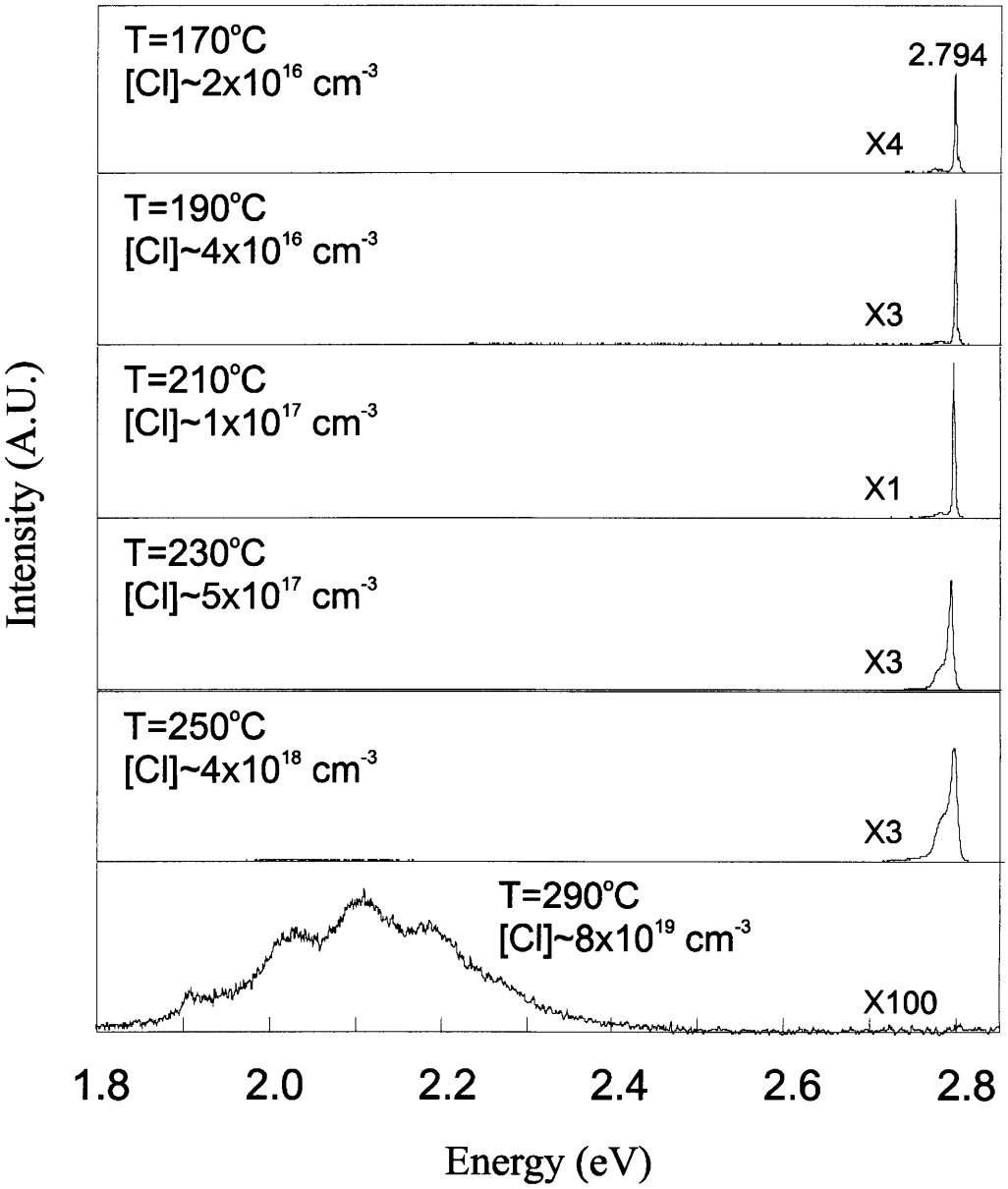

Figure 3–7 10K photoluminescence of Cl-doped ZnSe films having a progressively higher doping concentration from the top to the bottom subplots. The $ZnCl_2$ cell temperature, relative magnifications used to obtain the spectrum, as well as the [Cl] determined by SIMS are indicated in each case.

from 1.8 to 2.4 eV. The abrupt change in the PL spectrum is believed to be due to defect generation and compensation, and is similar to results reported at high doping levels achieved by MBE [85].

3.4 P-type Doping Using a Nitrogen Plasma Source

For many decades, the goal of p-type ZnSe proved unattainable for the many researchers in pursuit of II-VI materials for blue light emitters using conventional, bulk growth techniques. The advent of sophisticated non-equilibrium growth techniques such as MBE and MOVPE provided unprecedented atomic-level control and source flexibility in the growth and doping of II-VI compounds. Consistent and practical p-type conductivity of ZnSe, nevertheless, remained elusive for years. Although n-type conductivity of ZnSe was achieved early on, the strong tendency for "self-compensation" had prevented the achievement of p-type conversion in ZnSe. In general, acceptor self-compensation refers to the process where the increased inclusion of acceptors led to highly compensated (and resistive) resultant films instead of p-type, electrically active material. Early theoretical efforts originally argued that native donor-like defect formation, such as vacancies and interstitials, may electrically counteract the incorporated acceptors [87]. It is now believed that the compensation is caused by a large lattice relaxation around the acceptor site as originally proposed by Chadi and Chang based on first-principles energy calculations [88]. Chadi et al. also concluded that nitrogen would form sufficiently shallow acceptor states in ZnSe; other theorists later confirmed their findings [89]. But early attempts to introduce nitrogen had not been consistently successful: dopant precursors in the form of N_2 and NH_3 were found to have low sticking coefficients and thus difficult to incorporate [90]. It was not until the introduction of a plasma source of nitrogen during MBE, reported independently by Ohkawa et al. [91] and Park et al. [92], that *consistent and stable* p-type conversion of ZnSe became possible. Both experimental and recent theoretical evidence, however, indicate that self-compensation, in the form of compensating donors that are generated in response to high levels of nitrogen incorporation, limits the maximum achievable hole

concentration to be $\leq 10^{18}$ cm^{-3} for ZnSe [93,94,76,95], and still lower for wider bandgap quaternaries such as (Zn,Mg)(S,Se) [96,97]. These issues are presently being explored, and its resolution will be important for eventual success of the II-VI industry.

Since the initial breakthrough in p-type doping, the field of II-VI research has exploded, leading to both increased understanding of the doping and compensation process in ZnSe, as well as impressive achievements in blue-green laser devices. Based on the successes of nitrogen doping in MBE, a plasma source of nitrogen, identical to the ones used in the original MBE nitrogen doping experiments, was used for the growth of ZnSe:N by GSMBE. Figure 3–8 shows the progression of the PL spectra as a function of the chamber equivalent pressure of nitrogen flow for lightly-doped samples. In this figure, the 10 K spectra are shown for samples grown under identical growth conditions: the nitrogen gas flow was systematically increased to enhance the incorporation of acceptors into the lattice. As is seen in Figure 3–8, the characteristic PL features of the ZnSe:N films are seen to be strongly dependent on the degree of nitrogen incorporation. The growth conditions for this series of films were as follows: a 270°C calibrated substrate temperature, a slightly Se-rich surface stoichiometry, and a constant RF power of 100 Watts (using the water-cooled plasma source). The PL progression as a function of the increasing nitrogen flow was characteristic of increasing nitrogen incorporation, a trend similar to that reported by Ohkawa et al. for MBE-grown ZnSe:N [91]. For the sample grown with the lowest nitrogen flow (shown in Figure 3–8(b)), the near-bandedge transitions were dominated by the neutral N acceptor bound exciton peak at 2.793 eV. PL obtained from an undoped sample is shown for reference in Figure 3–8(a). The free electron-to-acceptor transition (FA) was present at 2.716 eV to suggest a nitrogen acceptor binding energy of 109 meV, assuming a 10 K bandgap energy of 2.825 eV [98]. The donor-to-acceptor-pair (DAP) transition peak at 2.698 eV and the

associated phonon replicas were also present. Further increases in the nitrogen flow resulted in a spectrum dominated by the FA and DAP transitions (and their LO phonon replicas), as shown in Figure 3–8(c). At the highest nitrogen gas flow investigated (Figure 3–8(d)) for this series of growth, the FA transition disappeared, while the DAP and phonon replicas merged into a single broad feature.

The structural characteristics of the nitrogen-doped ZnSe films were similar to the undoped layers. For example, the surface remained largely featureless for most doping conditions

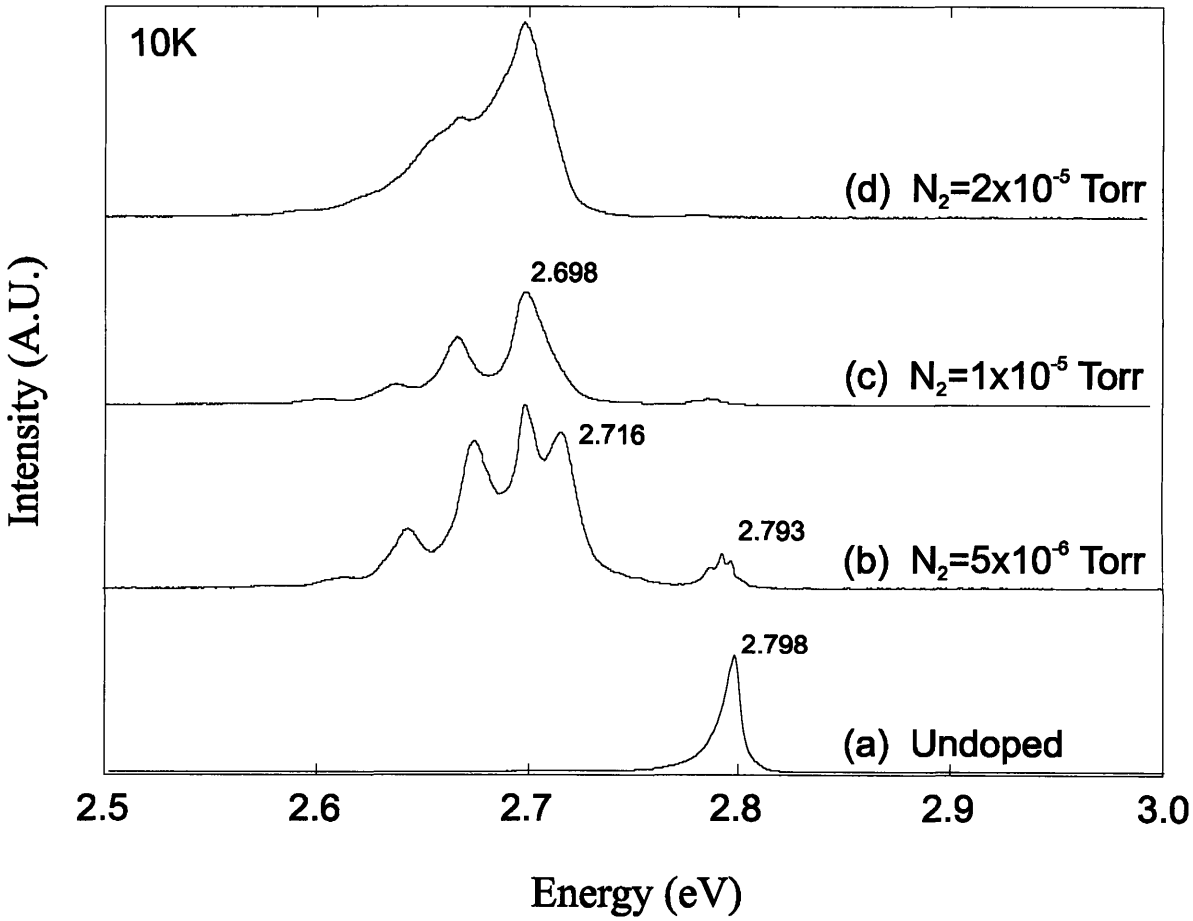

Figure 3–8 10K photoluminescence intensity as a function of energy demonstrating the evolution of the spectrum as the nitrogen gas equivalent pressure is increased from that obtained from a reference undoped sample (a). In (b)-(d) the nitrogen flow was increased to vary the incorporation of the nitrogen acceptor species.

explored thus far; the (400) peak of the rocking curves exhibited typical FWHM (~175-200") as described previously for undoped layers.

The effect of surface stoichiometry on the incorporation of nitrogen has also been investigated. The photoluminescence spectra shown in Figure 3–9 were obtained from two nitrogen-doped ZnSe films that were grown under identical growth conditions except that the surface stoichiometry was maintained as either Se-rich (Figure 3–9 (a)) or Zn-rich (Figure 3–9 (b)) (as monitored by RHEED reconstruction patterns) during the growth. In agreement with earlier reports, an increase in the nitrogen concentration is reflected in the PL spectrum as a merging of the DAP band and LO phonon replicas into a single peak [5,76,99]. Thus, for a given doping condition, a Zn-rich surface appeared to incorporate the nitrogen species more effectively

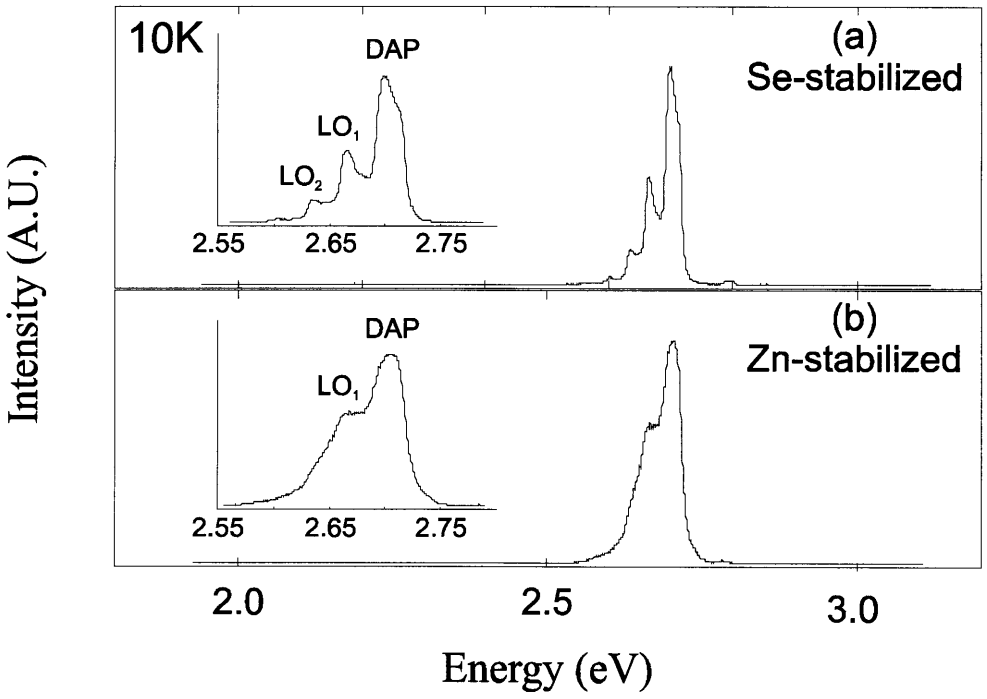

Figure 3–9 PL of (a) ZnSe:N epilayer where the growth was performed under Se-stabilized conditions throughout, and (b) ZnSe grown under otherwise similar conditions as (a), but under a Zn-rich condition instead. The insets show detailed near-bandedge spectra.

and was subsequently verified by SIMS.

By increasing the nitrogen flow using various combinations of aperture configurations as well as higher applied RF power, significant concentrations of nitrogen (as measured by SIMS) were found to be incorporated during the GSMBE growth of ZnSe.

Figure 3–10 shows the measured nitrogen concentration [N] as a function of the nitrogen doping parameter defined as the product of the RF power and the chamber equivalent pressure of nitrogen flow. The [N] is seen to increase proportionally with the doping parameter as either the RF power or the nitrogen flow is increased while maintaining the high brightness mode of operation. At higher doping levels ([N]$\geq 10^{18}$ cm^{-3}), the PL spectrum becomes progressively

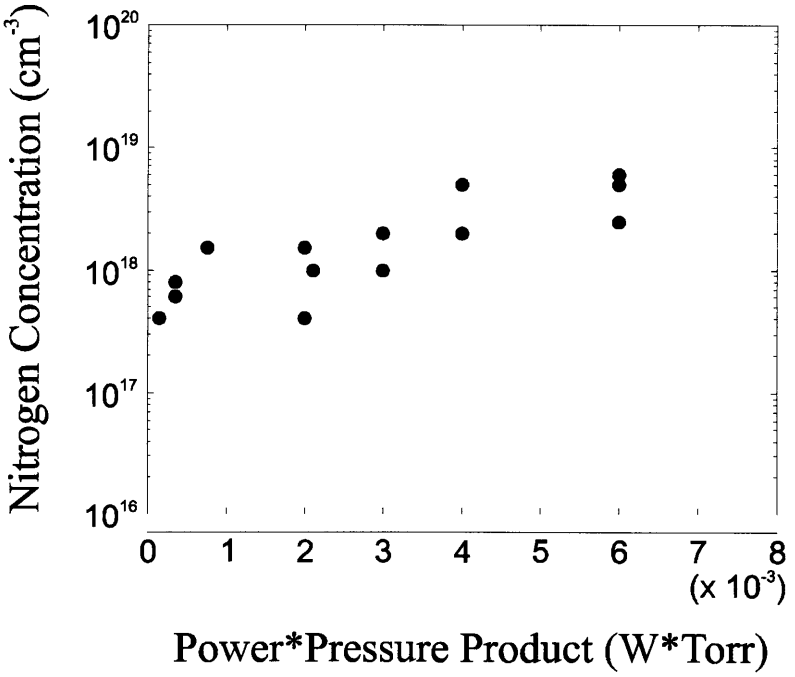

Figure 3–10 Incorporated nitrogen concentration, [N], as a function of the nitrogen doping parameter, RF power * gas pressure. Note that the plot does not delineate layers produced using various stoichiometries and temperature conditions.

broader and lower in energy; this is consistent with the current speculation that donor-defects of increasing depth from the valence bandedge appear as the ZnSe becomes more heavily-doped.

Electrical measurements of ZnSe:N grown by GSMBE, however, indicated that most of the films were highly resistive regardless of the actual incorporated nitrogen concentration or the appearance of PL spectra that is normally suggestive of p-type conversion. For example, PL spectra, as shown in Figure 3–8(c) and Figure 3–8(d), would be associated with ZnSe:N films grown using conventional MBE in our chamber that exhibit $[N_A\text{-}N_D] > 10^{17}$ cm^{-3}. As will be described in detail in the next section, the culprit of this observed electrical passivation of the incorporated nitrogen acceptors is now established to be the hydrogen molecules that are copiously present in the GSMBE growth environment.

3.5 Hydrogen Passivation

Hydrogen passivation of both donors and acceptors have been extensively reported for III-V compounds grown by MOVPE, as well as MOMBE [100,101,102,103,104]. There also exists a substantial body of papers dealing with hydrogen in the Si material system [105]. Recent results for ZnSe grown by MOVPE [106,107], as well as experiments where ZnSe was intentionally hydrogenated with deuterium [76], suggest that hydrogen is electrically and optically passivating the nitrogen acceptors in ZnSe:N. Unlike hydrogen in III-V and Si material systems, its counterpart in nitrogen-doped ZnSe is differentiated by the relative difficulty in reversing the passivation behavior by thermal treatments. In most cases, post-growth thermal treatment at or above the normal growth temperatures for a significant length of time is required to modify the behavior of the incorporated hydrogen.

Because of the large amount of hydrogen that is present in the GSMBE growth environment, most as-grown ZnSe:N films were found to be highly resistive due to hydrogen passivation. In order to investigate the relationship between the hydrogen and the nitrogen concentration that is incorporated, a variety of structures have been grown that contained intentional variations in the nitrogen concentration.

Figure 3–11 shows a SIMS profile of a ZnSe:N layer grown on p-type GaAs by GSMBE.

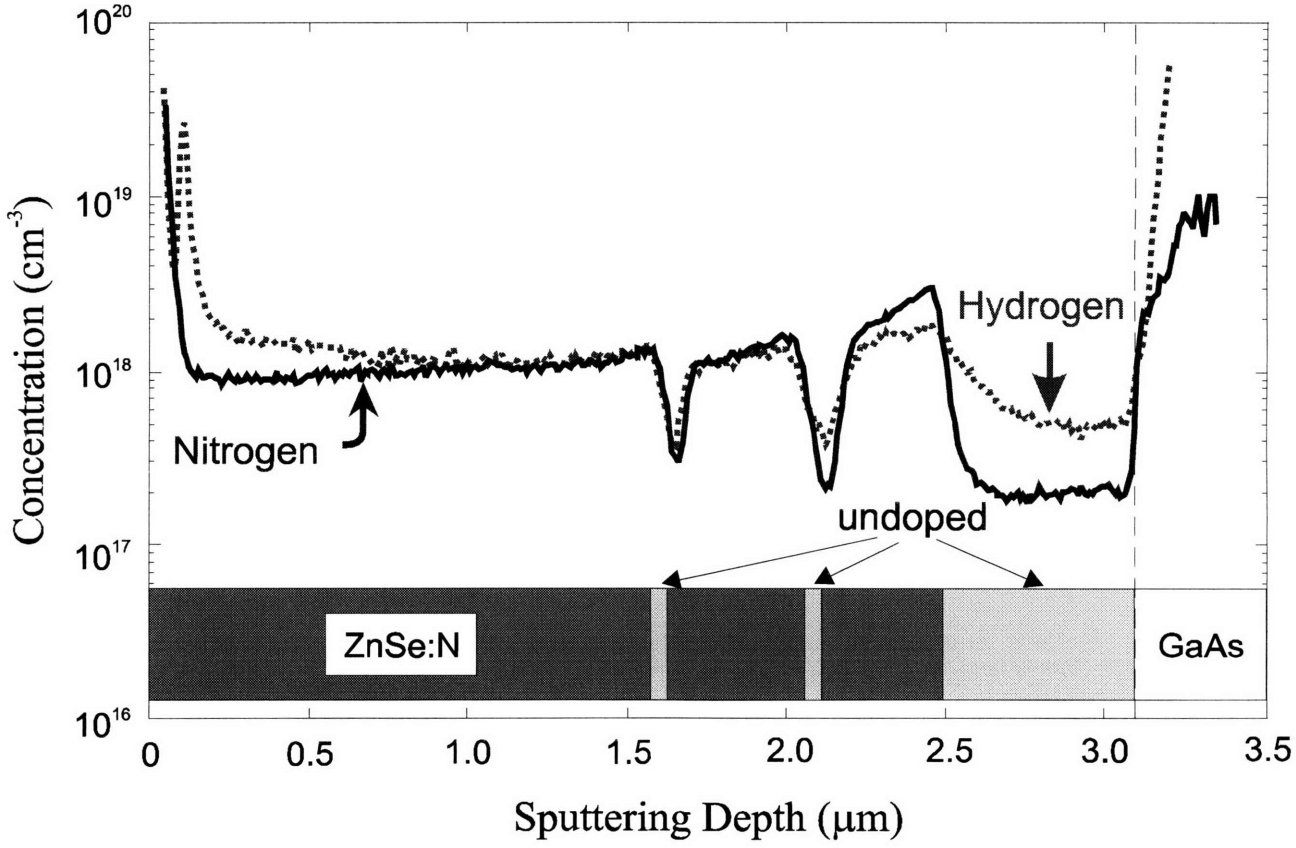

Figure 3–11 SIMS depth profile obtained from a uniformly-doped ZnSe:N epilayer grown by GSMBE on an undoped ZnSe buffer layer. The undoped ZnSe layers, as indicated in the schematic, provide references for the background concentrations of [N] and [H]. The synergistic correlation between [N] and [H] is clearly seen. The dramatic increase in the signal at the surface and at the ZnSe/GaAs interface are due to surface effects and an artifact of the data normalization procedure, respectively.

The particular structure depicted contains several undoped ZnSe regions (that enable the determination of the background levels of [H] and [N]) in an otherwise uniformly nitrogen-doped ZnSe film having [N] ~10^{18} cm^{-3}. Several striking features are apparent in the figure: (*i*) the extraordinary tracking behavior of [H] with the variation in [N]; (*ii*) both [N] and [H] decreased to their respective background levels in all of the undoped regions; and (*iii*) in the ZnSe:N region, the ratio [N]/[H] was nearly unity. Similar tracking behavior between [H] and [N] has been observed for ZnSe:N films grown under a wide variety of GSMBE growth and doping conditions [108,109]. These facts suggest that the observed incorporation of hydrogen is directly related to the presence of nitrogen. Nearly all of the as-grown films are highly resistive as determined by C-V measurements, further suggesting that the nitrogen acceptors have been effectively passivated by hydrogen. These results are in agreement with spectroscopic data obtained for nitrogen-doped ZnSe grown by MOVPE, where direct evidence of the N-H bonds has been reported [106,107].

For ZnSe:N films grown by conventional MBE under similar corresponding growth conditions (surface stoichiometry, substrate temperature and incorporated [N]) in the same chamber, the hydrogen concentration was found to remain below the detection limit of the SIMS instruments we employed, suggesting that incorporation of hydrogen from the UHV background is negligible. Net acceptor concentration [N_A-N_D] of up to 6x10^{17} cm^{-3} have been obtained as measured by C-V measurements. Further improvement is expected by fine-tuning of the MBE growth, plasma doping, and nucleation conditions. Figure 3–12 shows a typical set of C-V profiles: (a) the measured capacitance as a function of voltage, and (b) the calculated $1/C^2$ vs. the applied voltage, and (c) the derived [N_A-N_D] as a function of the depletion depth. The shape of the curve in Figure 3–12(b) is indicative of positive carriers and was verified to be mirror images

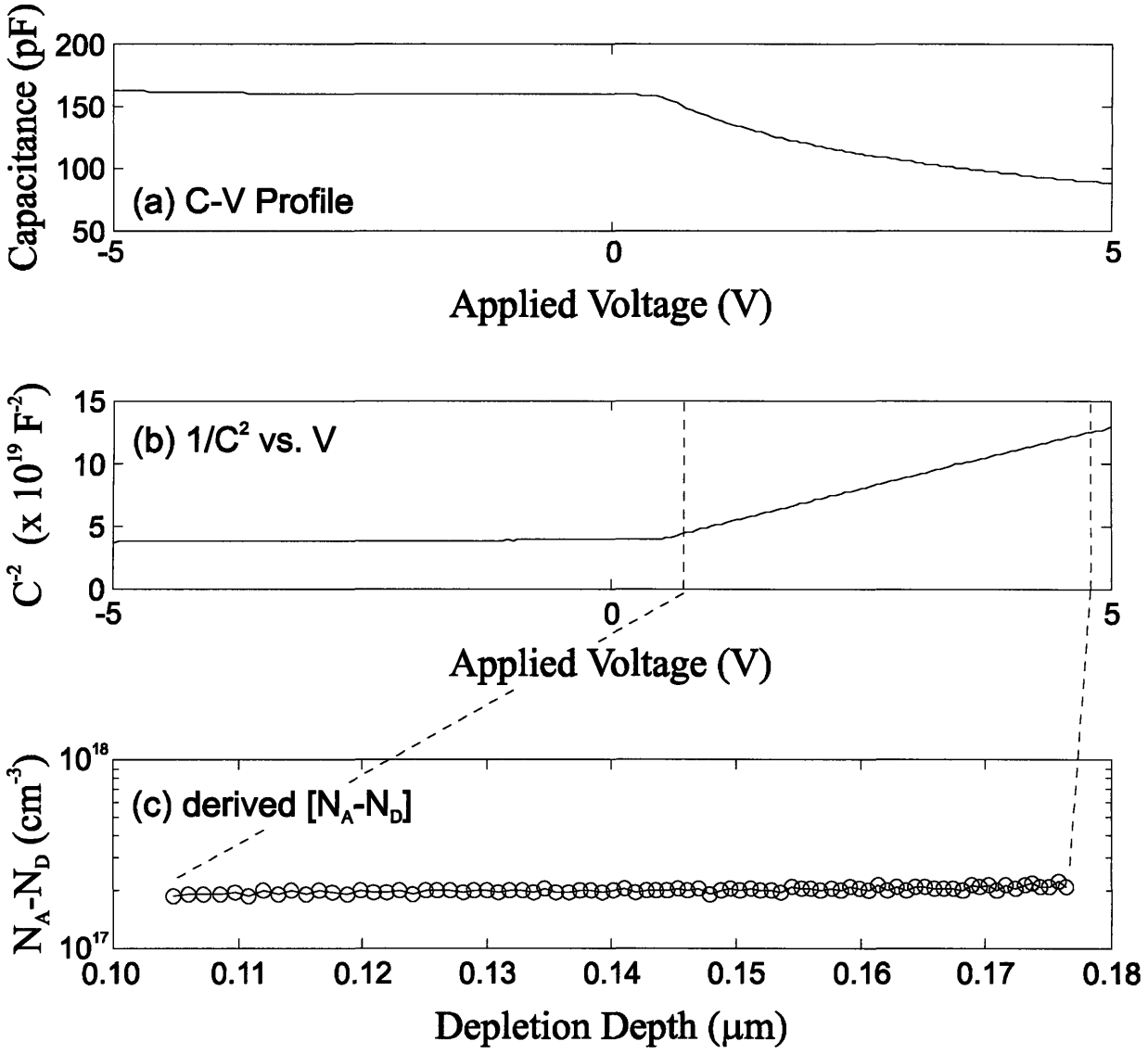

Figure 3–12 (a) Typical C-V profile of a ZnSe:N grown by MBE on a p-type GaAs substrate without intentional hydrogen injection. The vertical section of the $1/C^2$ vs. V curve between the dashed lines in (b) was used to derived the $[N_A\text{-}N_D]$ shown in (c).

of n-type ZnSe C-V profiles (whose electron conductivity was confirmed using Hall measurements). This particular sample was found to have a $[N_A\text{-}N_D]$ of ~ $2\text{x}10^{17}$ cm^{-3} using a vertical through-wafer measurement with a 500-μm diameter Schottky diode.[†]

[†] See Appendix B for more detailed discussion of the C-V method as applied to ZnSe.

For Cl-doped ZnSe sample grown by GSMBE, significant hydrogen passivation of the donors was not observed. Figure 3–13 shows a SIMS profile of a structure containing regions of chlorine-doped ZnSe grown by GSMBE for comparison. The undoped region near the ZnSe/GaAs interface serves again as the reference for the background levels of [H] and [Cl] for this analysis. As the [Cl] is intentionally varied, the [H] remained near the background level throughout the structure, increasing to a large value near the surface due to surface contamination. In stark contrast with the ZnSe:N films grown by GSMBE, the absence of the coherent tracking behavior between the dopant [Cl] and [H] also resulted in a negligible amount

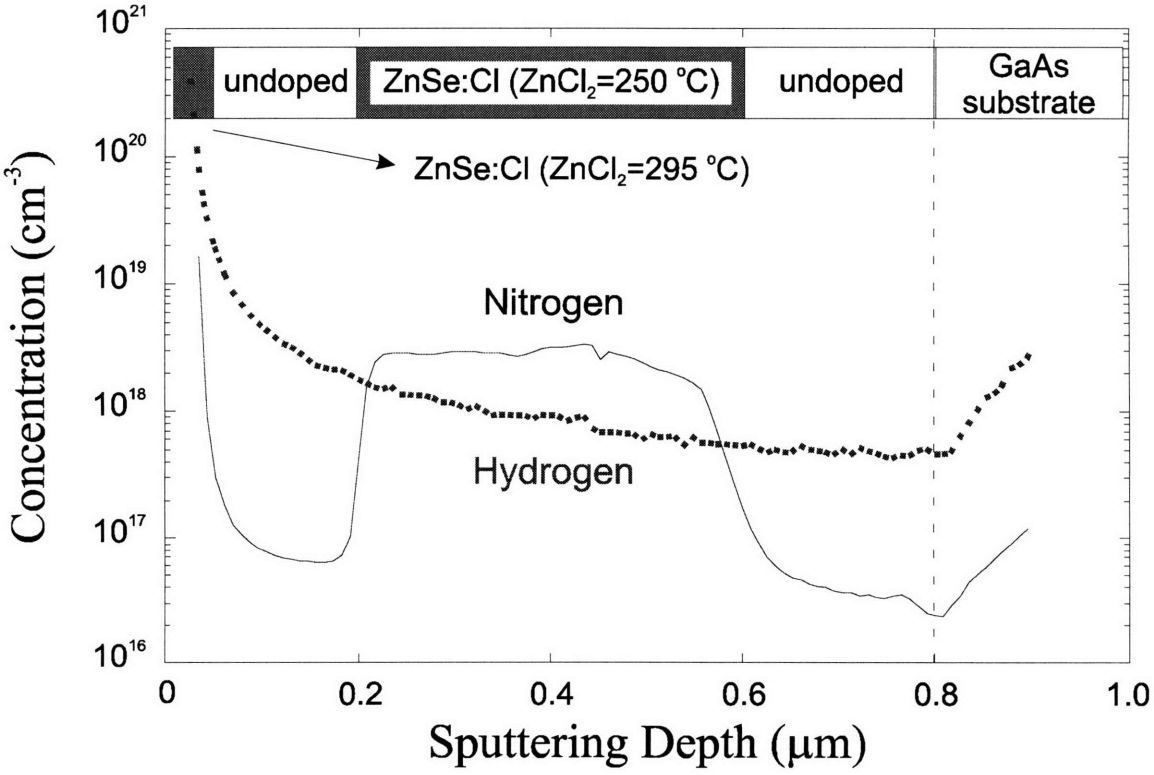

Figure 3–13 SIMS depth profile of a structure containing two Cl-doped regions separated by undoped regions (as references for the background concentrations of [Cl] and [H]). The $ZnCl_2$=295 °C layer was grown for the same amount of time as the $ZnCl_2$=250°C layer. The significantly reduced layer dimension for the higher cell temperature reflects the greatly diminished growth rate at high chlorine doping levels.

of electrical passivation. These two observations strongly suggest that the observed hydrogen that is incorporated is directly associated with the presence of the nitrogen acceptor species.

Our earlier thermal decomposition, or "cracking", studies using *in-situ* QMS indicated that molecular hydrogen is the major by-product of the H_2Se pyrolysis. Figure 3–14 shows the QMS signal intensity (left vertical axis, in uncalibrated units of detector current) as well as the

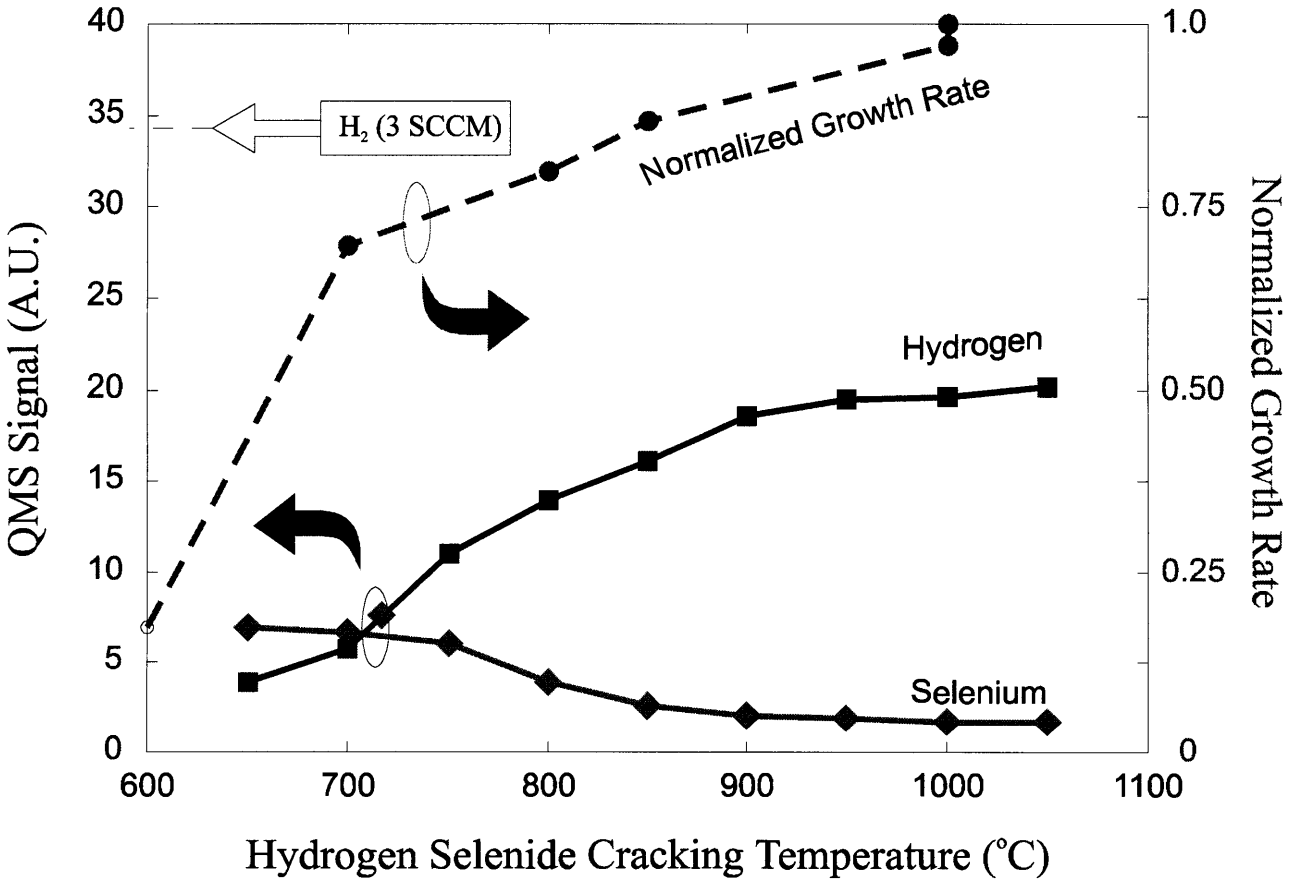

Figure 3–14 Comparison of the H_2 and elemental selenium signals (left vertical axis) as seen by a QMS that is generated as a by-product of the H_2Se cracking; also shown is the signal obtained by 3 SCCM of intentionally introduced H_2 gas. The right vertical axis depicts the relative growth rates (normalized to neutralize the effect of varying group II fluxes) as a function of the H_2Se cracker cell.

normalized growth rate (right vertical axis, per SCCM of H_2Se scaled to unity for the highest growth rate obtained at 1000°C) as a function of the H_2Se cracking cell temperature. The growth rate increases dramatically above 600°C, indicating the onset of H_2Se decomposition. The hydrogen signal is also seen to increase above 600°C with increasing cracker temperature and is accompanied by a corresponding decrease in the H_2Se signal, further suggesting the onset of H_2Se decomposition into H-Se radicals or Se_x molecules. The arrow at the upper left corner of Figure 3–14 indicates the level of QMS signal when 3 SCCM of H_2 is injected into the chamber. Hence, it can be reasoned that during the typical GSMBE growth of ZnSe, the amount of H_2 generated as a decomposition by-product of H_2Se is similar to that measured by the intentional introduction of ~ 1-2 SCCM of hydrogen gas.

3.6 Comparison with Intentionally Hydrogenated ZnSe by MBE

An important question that remains to be answered concerns the passivation that is observed during the GSMBE growth of ZnSe doped with a nitrogen plasma source, i.e., is the *dominant* source of electrical passivation derived from molecular hydrogen that is produced by cracking, or from hydrogen radicals still attached to the Se precursor? In order to quantify the role of molecular hydrogen in the passivation mechanism of nitrogen acceptors, experiments were carried out where various amounts of hydrogen were introduced into the chamber during conventional MBE growth. Figure 3–15 shows a SIMS profile of a structure containing intentionally hydrogenated layers (shaded regions in the structure schematic) where different amounts of molecular hydrogen were introduced. The structure also contains undoped layers (regions with line shading) as well as a doped region that was not exposed to a flux of hydrogen.

The main features to note in Figure 3–15 are as follows: (*i*) similar to GSMBE-grown ZnSe:N, [H] is seen to closely track [N], with both impurities decreasing to near their background levels in all of the undoped regions; (*ii*) a clear increase in [H] coincident with the addition of 1 SCCM H_2 (from the schematically indicated "ZnSe:N" region to the "ZnSe:N + 1.0 SCCM H_2" region) indicates that *nitrogen-induced hydrogen incorporation* has occurred; and (*iii*) the [N]/[H] ratio in the "ZnSe:N + 1.0 SCCM" region appears to be greater than the [N]/[H] in the "ZnSe + 3.5 SCCM H_2" region which is consistent with the assumption that the observed increase in [H] is directly related to the amount of injected H_2.

The apparent increase in [H] at the interface of the "undoped ZnSe" and "ZnSe:N" regions is due to residual levels of hydrogen in the shared hydrogen/nitrogen gas manifold that supplies the RF plasma cell at the time of the hydrogenation experiment. Some background level of passivation were therefore present in these particular experiments, even though H_2 was not intentionally introduced via the cracker. Furthermore, the hydrogen concentration in Figure 3–15 was obtained by a background subtraction procedure where a constant hydrogen background signal (determined at the undoped region) was subtracted from the measured hydrogen signal during the quantitation process. This procedure has a tendency to disproportionally magnify signals that are only slightly greater than the background signal used for subtraction (please see Appendix A for more details of the background level subtraction process). The presence of this low level, but uniform, passivation should not alter in any way the conclusions described above, as it is the *relative* concentrations of [H] that is of significance.

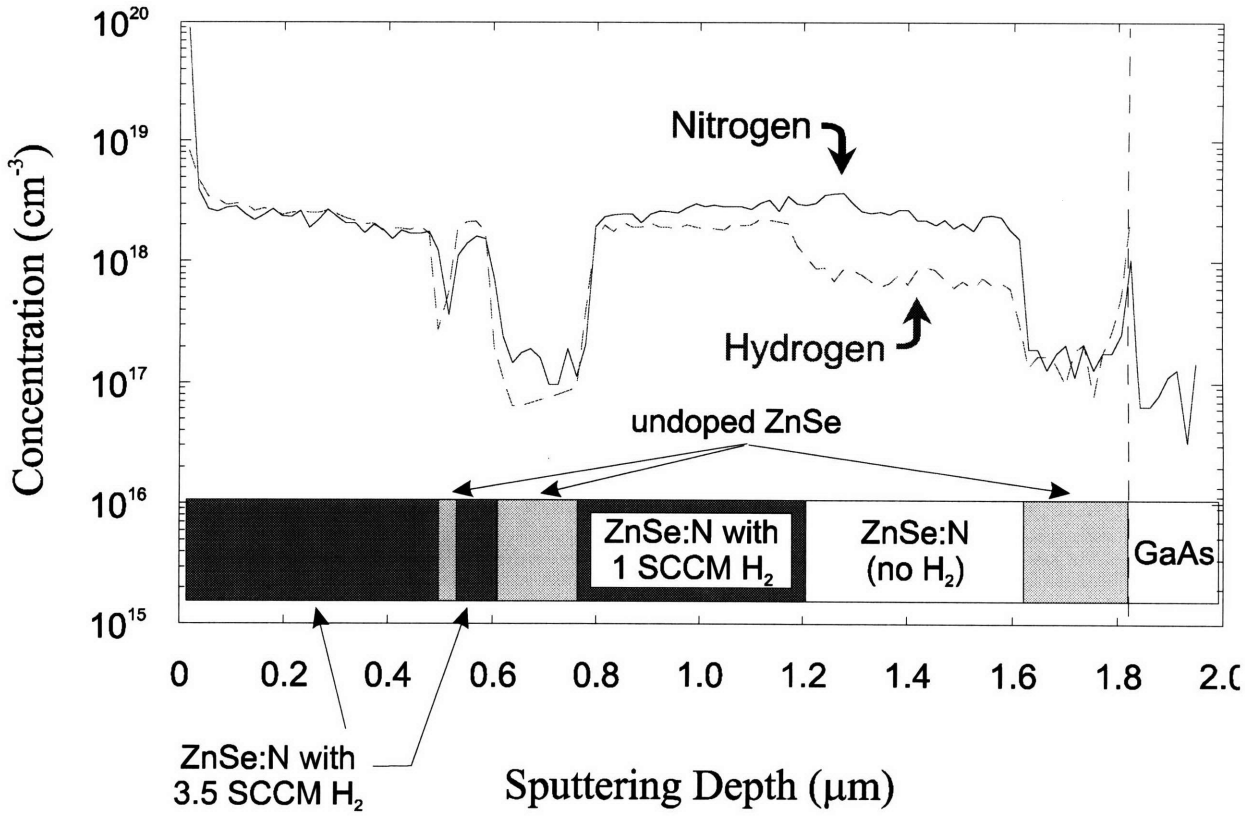

Figure 3–15 SIMS profile of a ZnSe:N layer grown by MBE on an undoped ZnSe buffer layer (on GaAs). As the depth into the ZnSe layer increases, various amounts of H_2 were introduced to the growth front, with three undoped regions as indicated. Variations in the H_2 flow are as indicated in the figure.

A comparison of C-V measurements performed on un-hydrogenated ZnSe:N films (reference films without H_2) and intentionally hydrogenated films (ZnSe:N + various amounts of H_2) lends further support to our hypothesis that molecular hydrogen acts to passivate the nitrogen acceptors in MBE using a nitrogen plasma cell. Several series of nitrogen-doped films were grown by MBE, both with and without intentional hydrogen, using identical growth and doping conditions; C-V measurements were subsequently performed on all samples. With $[N_A\text{-}N_D]$ of ~ $2\text{x}10^{17}$ cm^{-3} for the un-hydrogenated reference samples (typical MBE growth), it was generally found that a significant decrease in $[N_A\text{-}N_D]$ occurred for films that were grown with injected hydrogen. As

an example of the magnitudes of passivation that was observed, 25% and 60% passivation were measured for flow rates of 1 and 2 SCCM of H_2, respectively, as compared to the reference (un-hydrogenated) MBE-grown samples (where passivation is taken to be the 0% reference). This particular set of hydrogenation runs were grown at 280°C, under slightly Se-rich conditions with the following RF source parameters: 400 W power and 2.2×10^{-5} Torr chamber background N_2 pressure.

The precise amount of passivation was found to depend on the growth and doping conditions, as well as the hydrogen flow rates that were used. Figure 3–16 shows a "normalized

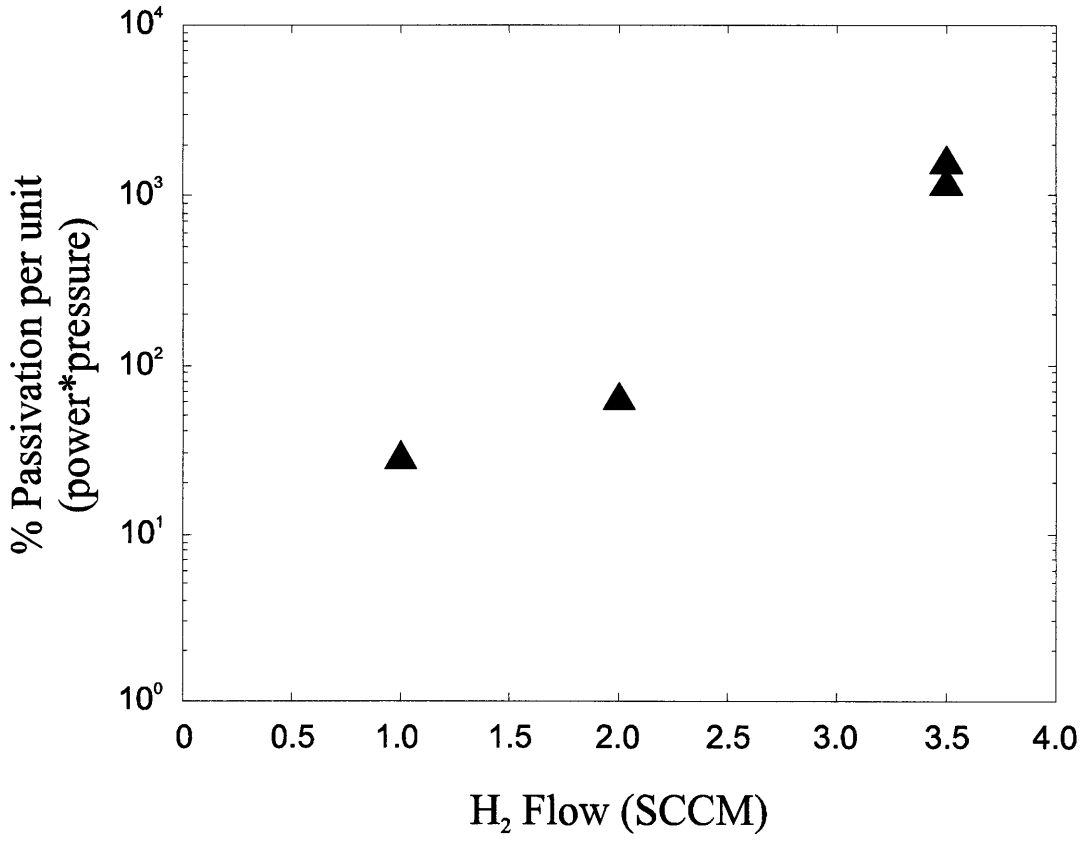

Figure 3–16 The percentage of acceptor passivation (normalized by the doping parameter previously defined as the product of "power * pressure") as a function of the intentionally injected H_2 flow rate in SCCM.

percent passivation" (normalized by the nitrogen doping parameter defined earlier) as a function of the hydrogen flow rate used during the hydrogenation experiments. The positive slope in Figure 3–16 highlights a result that we would reasonably expect: that more hydrogen present at the surface *for a given amount of active nitrogen* species gives rise to a larger degree of observed passivation. Note again that it is the relative amount of passivation that is of interest here and not the absolute magnitudes.

The result embodied in Figure 3–16 can also be stated in a corollary manner: the amount of electrical passivation depends on the amount of active nitrogen present for a *given flow of hydrogen*. These results and postulates advanced above are consistent with recent data on thermal annealing of MOVPE-grown ZnSe:N films obtained by Ogata et al. [110], where annealing of ZnSe:N epilayers (possessing an initial net acceptor concentration of 2.0×10^{17} cm^{-3}) in an H_2 ambient at 350°C was found to provide significant electrical passivation of the nitrogen acceptors. More detailed studies are required to quantitatively understand the passivation relationship between the active nitrogen species and the H_2 present at the growing surface.

As shown in the previous H_2Se cracking experiments, 2 SCCM of injected H_2 provides a background hydrogen signal (as detected using QMS) that is approximately equal to that normally encountered during normal GSMBE growth. Since the degree of electrical passivation of GSMBE-grown ZnSe:N samples is found to be much more significant than those measured for the MBE + H_2 counterparts exposed to similar H_2 background levels, we speculate that at least an equally important mechanism for nitrogen acceptor passivation is related to the incompletely cracked Se-H fragments. It is expected that hydrogen passivation during GSMBE growth can be *minimized* by cracking the H_2Se precursor as completely as possible; however, our results seem to indicate that some passivation is inevitable due to the presence of H_2 under normal growth and

stoichiometric conditions. This reasoning might also play a part in reconciling our present results with other seemingly contradictory results [111,112], where hydrogen passivation has been reportedly absent in GSMBE-grown ZnSe:N using the same precursors. We believe that the hydrogenation behavior described here has significant implications for the GSMBE, as well as MOVPE, growth of ZnSe:N where multiple pathways for hydrogen incorporation may exist. Further experiments are currently underway to study the effect of growth and surface stoichiometry conditions on hydrogen incorporation under both MBE and GSMBE growth conditions. It is our belief that further and fundamental understanding of the surface kinetic reactions that occur with hydrogen during GSMBE and MOVPE will ultimately dictate the usefulness of GSMBE and MOVPE for achieving practical and reproducible p-type conductivity in wide bandgap II-VI's with nitrogen acceptors.

3.7 Effect of Annealing

It thus appears that hydrogen can be easily incorporated into ZnSe:N when hydrogen or hydrogen-containing radicals are present during the growth of ZnSe (either by GSMBE or MBE) over a wide variety of growth conditions. A natural question that arises is whether or not the passivating hydrogen can be just as easily dislodged by thermal annealing. We have investigated the effect of thermal annealing (using both long term and rapid-thermal heating) on the PL and [H] of ZnSe films grown by both GSMBE and MBE+H_2. Long term thermal annealing was carried out in a heated quartz tube under a nitrogen ambient for up to 2 hours; rapid thermal annealing (RTA) was performed using a heat lamp in 2-minute increments. ZnSe caps were used to cover the samples being annealed in order to minimize Se out-diffusion. It had been

previously observed that samples with annealing cap suffered less PL degradation compared to uncapped samples under the same annealing conditions.

For GSMBE-grown samples having moderate [N] of mid 10^{17} cm^{-3}, annealing in a N_2 ambient up to 500°C for 1 hour was found to have negligible effect on the PL properties (see Figure 3–17). Similarly, RTA treatment of samples with comparable [N] also showed no degradation in PL up to 500°C for 2 minutes. At 600°C annealing for 1 hour, however, some degradation of the PL was observed. Figure 3–18 shows the results of the subsequent SIMS analysis of the as-grown and the annealed samples, revealing [N] and [H] profiles that are

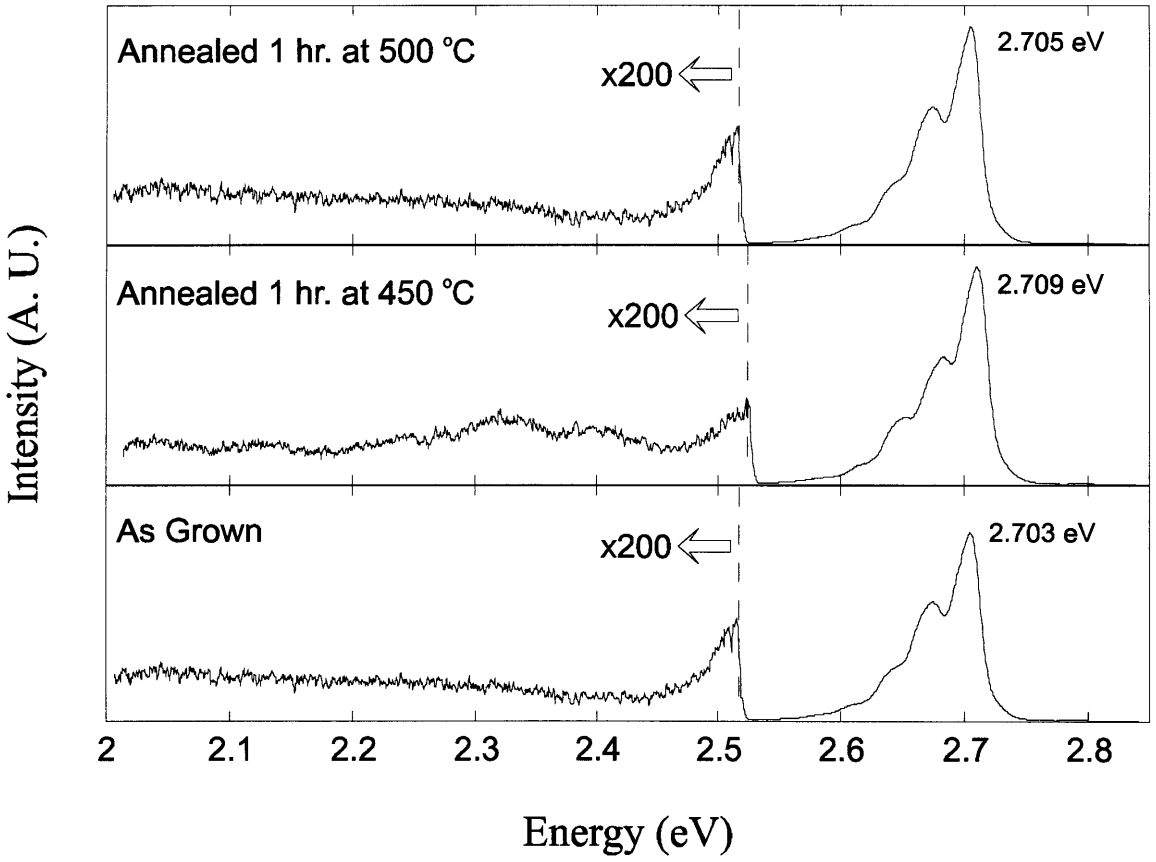

Figure 3–17 The effect of long term annealing on the photoluminescent properties of ZnSe:N grown by GSMBE under different annealing temperatures.

suggestive of decreased [N]/[H] ratio with annealing. However, C-V measurements on these samples were unable to confirm a change in conductivity. In light of the fact that only 1 or 2 samples showed a sizable separation in [N]/[H] ratio and the error margin inherent in SIMS measurements (especially the quantitation of [H]), these results should be taken together to be "inconclusive" at best.

In order to better quantify the effect of thermal annealing, intentionally hydrogenated MBE samples were also annealed to evaluate its effect on photoluminescent and electrical properties.

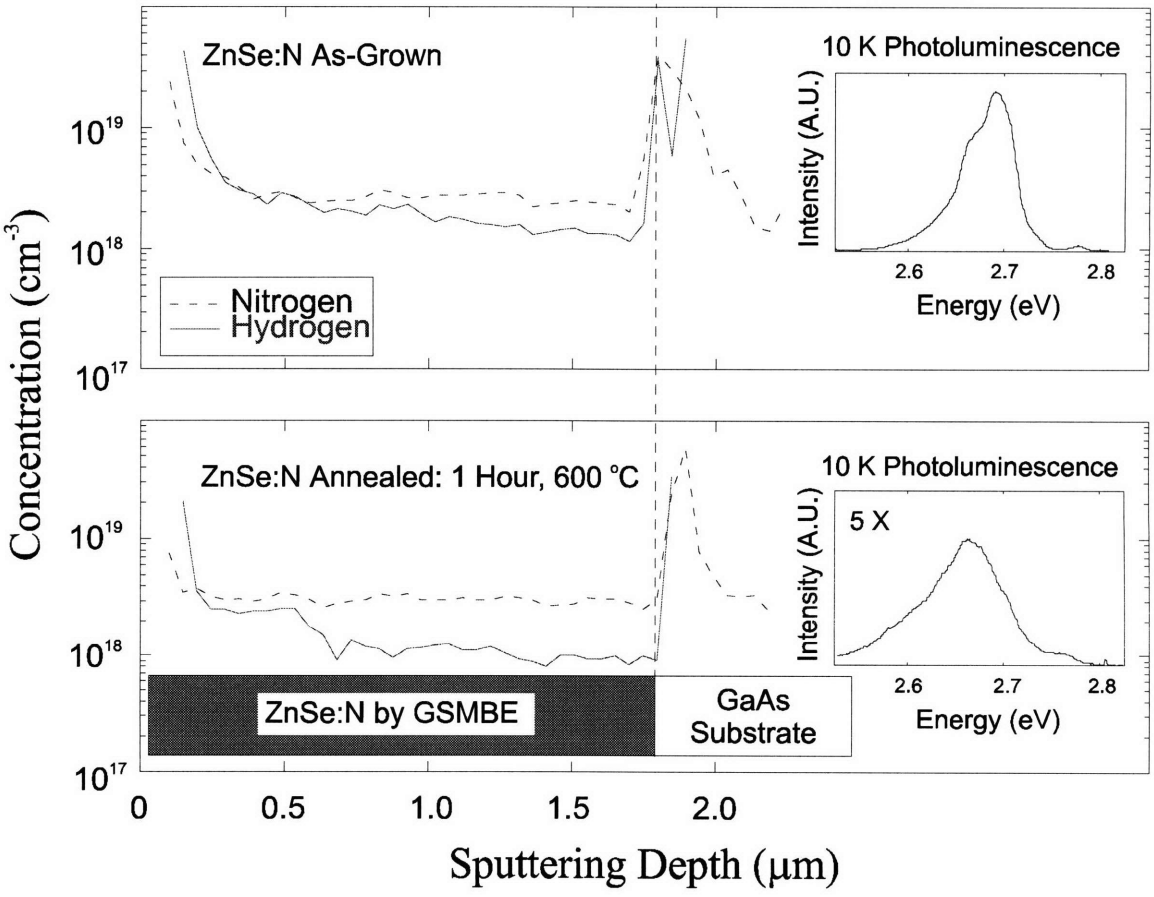

Figure 3–18 SIMS profile and photoluminescence (insets) of ZnSe:N grown by GSMBE (a) before and (b) after 600 °C long term annealing for 1 hour. The post-anneal SIMS profile suggests possible widening of the separation between the [N] and [H] as a result of annealing.

The as-grown (but hydrogenated) samples were found to have a measured net acceptor concentration of ~ $1.5x10^{17}$ cm^{-3} prior to thermal treatment for two hours in a nitrogen ambient. As seen from Figure 3–19, the electrical properties were essentially unaffected up to an annealing temperature of 400°C. At 500°C annealing for two hours, a large drop in the net acceptor concentration of approximately one order of magnitude was observed, indicating the onset of electrical degradation. The similarity in the annealing behavior of the ZnSe:N reference sample (■) and ZnSe:N with intentional hydrogenation (▲) suggests that the thermally-induced degradation dominates over any recovery effect that may have occurred as a result of the dissociation of the passivating hydrogen. Comparisons of the PL also indicated a change in the spectra occurred between 400 and 500°C. A more detailed and systematic study between 400-500°C is required to further elucidate this issue.

The discrepancy between the above annealing results of both the GSMBE and MBE+H_2 samples, and those reported in the literature regarding the reactivation of hydrogen-passivated ZnSe:N samples grown by MBE as well as MOVPE, cannot be reconciled at this point. It has been reported that MBE samples can be reversibly passivated and reactivated by heating to 300-400°C in hydrogen and nitrogen ambient, respectively [110]. There have also been reports indicating that as-grown and highly passivated ZnSe:N grown by MOVPE can be annealed to yield moderately conducting p-type samples [13].

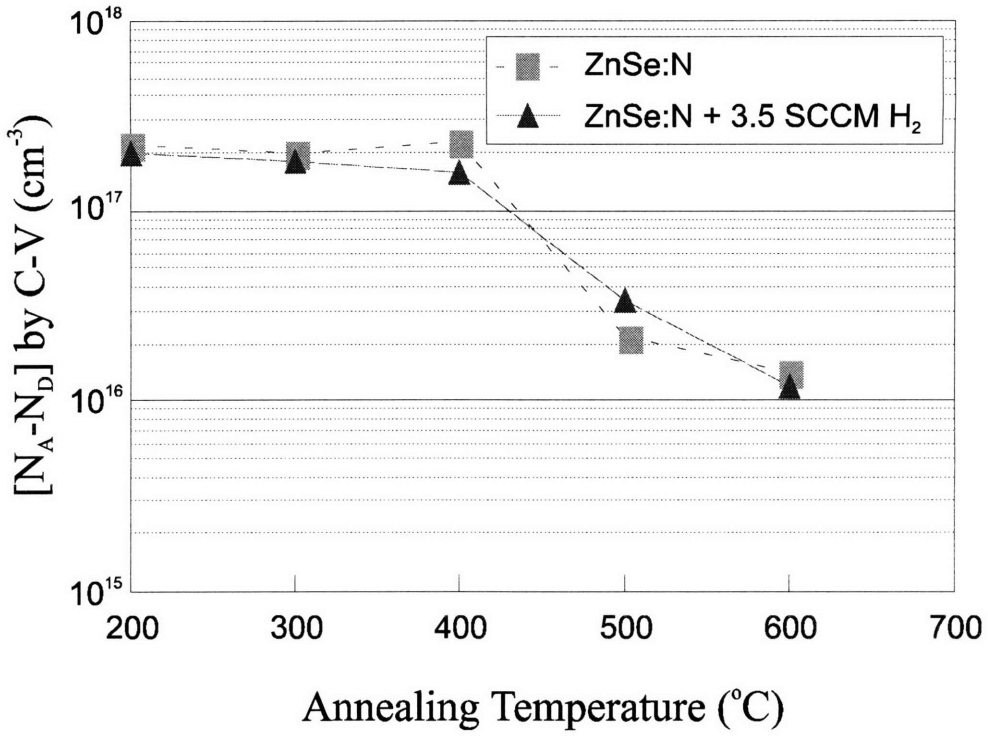

Figure 3–19 Net acceptor concentration of MBE-grown ZnSe:N (■) and ZnSe:N with intentional hydrogenation (▲) as a function of the annealing temperature.

3.8 Summary

The use of alternative non-equilibrium growth approaches, as applied to wide bandgap II-VI binaries, ternaries, and quaternaries, is clearly highly desirable, particularly to facilitate flux control of high vapor pressure species. This is the identical motivation that motivates the large number of researchers working on the MOVPE growth of the II-VI's. The anticipated benefits of the II-VI GSMBE approach are expected to parallel the advantages recognized and enjoyed by the III-V community for the growth of (In,Ga)(As,P) materials employing GSMBE and MOMBE. Similarities that exist include multiple high vapor pressure of the constituent species

(Zn, Se, S, Te $\leftrightarrow$ As, P) and the need to utilize quaternaries for lattice-matching and for bandgap engineering of sophisticated electronic and photonic devices. Significant contrasts in the growth of the II-VI's and the III-V's, however, include substantial differences in the growth temperatures (~ 300°C for ZnSe compared to ~ 600°C for GaAs), and the fact that the II-VI elements do not have unity sticking coefficients (as does Ga during the growth of GaAs). The similarities and contrasts between the growth of II-VI's and III-V's impose new constraints in the application of different growth techniques for each material family. Regardless of material family, however, the application of new techniques requires a great deal of research and investigation to discover the appropriate operating parameters required to optimize device performance. It is at this stage of research that we are investigating the advantages and the potential barriers to the utilization of gaseous source UHV epitaxy technologies for the growth of wide bandgap II-VI materials. The issue of source purity and hydrogen-containing organic chains, combined with the low substrate temperatures necessary for the II-VI's, suggest that novel metalorganic precursors [113,15] are important directions to pursue.

In the case of GSMBE, we have demonstrated that hydrogen plays an important role in passivating nitrogen acceptors in ZnSe. It is important to emphasize that our result not only applies to GSMBE techniques where hydrides are used, but also to MOVPE techniques where the use of hydrogen carriers are common in addition to the myriad of hydrocarbon species that may be present. Additional research will be necessary to determine the surface kinetic processes that can inhibit the incorporation of hydrogen, eliminating the need to resort to post-growth annealing treatments. In fact, interesting results [111,112] reporting p-type conductivity in as-grown ZnSe:N GSMBE and the fabrication of optical devices are very encouraging, and suggest that hydrogen incorporation during growth can be minimized if not avoided. An area that has

received very little attention involves the thermal decomposition behavior of II-VI precursors, both metalorganic- and hydride-based, as well as the surface reactions of these molecules in an ultrahigh vacuum environment. Clearly, much more work is necessary before we can determine the suitability of these new growth approaches for wide bandgap II-VI materials, and thus a very rich and interesting field still awaits development.

3.9 Outstanding Issues and Suggested Future Work

In more specific terms, several groups of experiments can be carried out to complement the results already outlined above:

(1) Post-growth hydrogen dissociation: As mentioned previously, hydrogen is known to be easily driven from (or made electrically inactive in) the host semiconductor by thermal annealing at moderately low temperatures compared to normal device processing thermal budgets. Our annealing results with GSMBE-grown ZnSe:N thus far seem to indicate that ordinary thermal annealing in a nitrogen ambient is insufficient to obtain activation of the nitrogen acceptors. Paradoxically, some MOVPE-grown ZnSe:N have been shown to respond to thermal annealing between 350 - 400°C to yield moderately p-type material ($[N_A\text{-}N_D] \sim 1x10^{17}$ cm^{-3}); however, we have shown that thermal annealing of MBE-grown ZnSe:N samples begins to cause changes in the PL accompanied by a reduction in $[N_A\text{-}N_D]$ when annealed for 1 hour around 400°C (see Figure 3–19). It is speculated that the near complete passivation of the GSMBE-grown ZnSe:N (as well as some MOVPE samples that were shown not to respond to annealing) may render them difficult to activate due to

the competing defect generation processes that appear to accompany thermal annealing. It may be possible to affect the balance of these two processes using field-assisted annealing. We have recently just begun a collaborative effort with a group in Iceland to study field-assisted thermal dissociation of ZnSe:N samples grown by GSMBE as well as MBE with intentional hydrogen passivation. These results should be able to elucidate what difference that may exist between hydrogen passivation in the MOVPE, GSMBE, and MBE samples.

(2) Although there is no compelling evidence so far to believe that the hydrogen passivation mechanism in GSMBE is different from those reported for MOVPE-grown ZnSe:N [106,107], it would still be of interest to confirm this fact using some site-sensitive techniques such as optically detected magnetic resonance (ODMR) or Raman spectroscopy. Early ODMR work carried out at our laboratory was largely unsuccessful at room temperatures due to the poor signal-to-noise ratio encountered. A direct comparison using any one of the above spectroscopic techniques between MOVPE, GSMBE and MBE+H_2 samples should yield important information about the nature of the hydrogen passivation on a microscopic level.

(3) The original H_2Se low pressure, high temperature cracker utilized in our studies have presumably been designed and optimized for hydrides of arsenic or phosphorous. Although we have substantially modified the cracker by changing the arrangement of the tantalum baffles, size and configuration of the aperture of the exit baffle, and have also inserted a large amount of high purity tantalum foil in the cracker to increase the active surface area, further modification into a high pressure cracker (which is expected to dissociated the H_2Se in a different kinetic regime) has proven

to be difficult. Adding a second H_2Se cracker cell designed to perform under internal high pressures (~ Torrs) will provide important supplementary avenues to explore the condition in which *minimum passivation* can be obtained under the GSMBE environment.

(4) One additional approach to the hydrogenation issue takes clues from our earlier MOMBE work as well as the fact that the few reported MOVPE p-type activated ZnSe:N results were grown under photo-assistance (achieve with [13] or without [15] thermal annealing). We have shown that photo-assisted growth (as well as electron-beam-assisted growth) provides an effective way to affect the detailed chemistry at the growth surface. It is possible that, similar to the photo-assisted growth rate enhancements observed in MOMBE of ZnSe using ethyl-sources, the electron-hole pairs generated can beneficially influence the incorporation of hydrogen (for example, through the anti-bonding properties of holes that are swept toward the growing surface).

The type of experimental apparatuses at our disposal thus far has limited our results to a "macroscopic" understanding of the hydrogenation problem. The above suggestions stem partially from the motivation to further understand the problem at hand in its "microscopic" manifestation. When these results can be integrated with the knowledge base thus far accumulated, amphoteric conduction of ZnSe, and thus the practical application of GSMBE to ZnSe, can perhaps be achieved.

4. II-VI/III-V Heteroepitaxy

4.1 Motivation for the use of Epitaxial III-V Buffer Layers

To date, most II-VI optical devices have been built on GaAs by necessity due to the lack of suitable and commercially available ZnSe substrates. Although impressive LED and LD results have been recently reported for ZnSe structures grown on ZnSe substrates [114,115,116], the availability of such high quality ZnSe substrates [23,24] at the present appears to be severely limited and to involve great cost. Consequently, GaAs became (and remains) the uncontested substrate of choice because of its high quality and the relatively close lattice-match (0.27%) with ZnSe. Device designers are consequently required to abide by the lattice constant of GaAs, or otherwise must contend with the small but nonetheless deleterious effect of the lattice mismatch. Studies have further shown that the use of epitaxial GaAs buffer layers can substantially improve the quality of the II-VI/III-V interface and the subsequent II-VI layer quality [117,118,119]. The state-of-the-art, ZnSe-based injection laser diodes that operated under CW conditions at room temperature [34,35,36], for example, were primarily lattice-matched structures grown on GaAs substrates with GaAs buffer layers. Hence, understanding the nature of the ZnSe/GaAs (and in general, the II-VI/III-V interface), and perhaps of even more practical importance, repeatably obtaining ZnSe overlayers with low defect densities, are some of the key determinants in the eventual success of the II-VI field. Recent device degradation studies on II-VI injection optical devices have led to a growing consensus among researchers that defects arising from the GaAs

buffer/II-VI layer interface presently play the limiting role in the short device lifetimes observed in today's laser diodes [120, 121].

The use of alternative epitaxial III-V buffer layers *in-situ* transferred to an UHV-interconnected II-VI chamber for subsequent growth of ZnSe offers several tantalizing possibilities for improved material and device qualities:

(1) Using In, Al, and P in addition to Ga and As, a large degree of freedom in terms of bandgap and lattice constants is possible. Figure 4–1 revisits the familiar E_g versus a diagram showing the range of alloys possible using combinations of the above elements (shaded area ①). A large number of binary, ternary and quaternary II-VI compounds can be used to provide lattice matching over a wide range of

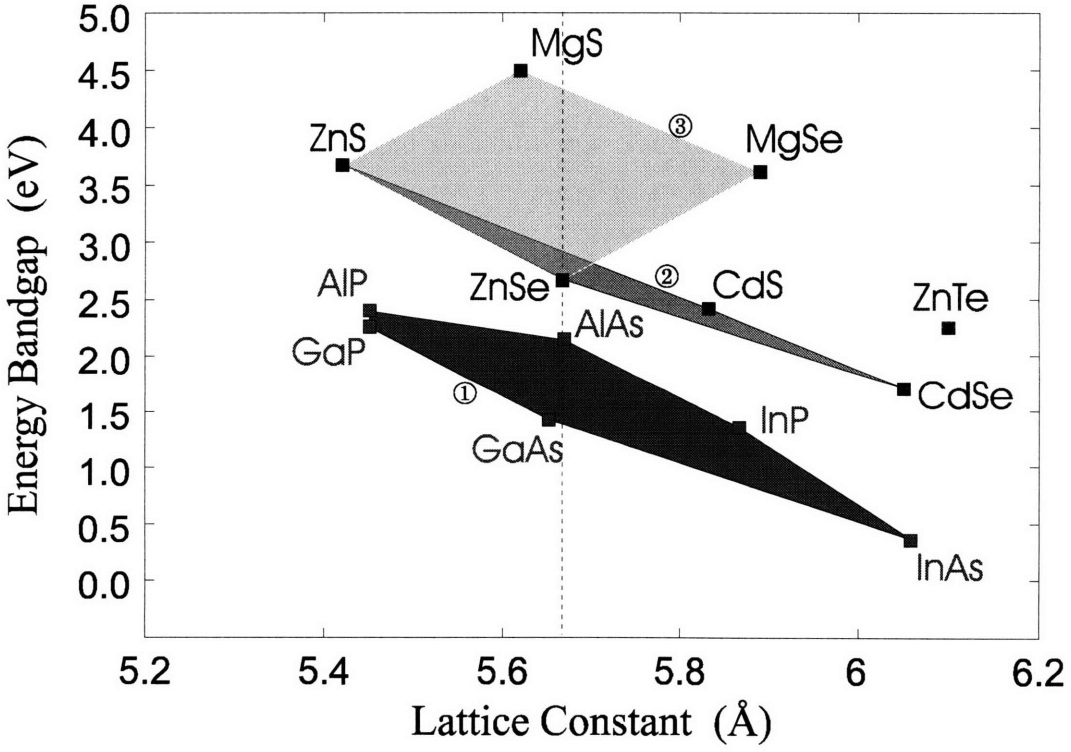

Figure 4–1 Energy versus lattice constant diagram emphasizing the relationship of possible III-V buffer layers and II-VI compounds.

(Zn,Cd)(S,Se) (shaded area ②), as well as (Zn,Mg)(S,Se) compositions (shaded area ③). For example, using InGaP or InGaAlP buffer layers, nominally pseudomorphic II-VI quantum well structures with binary ZnSe well regions can be used to achieve true "blue" laser diodes.

(2) By exploring the different interfacial chemistries afforded by various III-V buffer layers, it may be possible to affect the number of interfacial defects and/or reduce their influence on the active regions of optical devices. For example, it has been reported that the addition of small amounts of indium may serve to reduce the generation and multiplication of dislocations in GaAs [122,123].

(3) III-V buffer layers can also be bandgap-engineered to reduce the large valence band discontinuity that exists between p-type ZnSe and p-type GaAs (see Figure 4–2 (a)). The p-type contact has traditionally been a large obstacle for wide-gap II-VI materials because of the lack of suitable contact metals having sufficiently large work functions. The resultant large valence band spike occurring at the p-ZnSe and metal interface (or other homo-type junctions) increases the operating voltage of injection devices. The problem is further exacerbated by the difficulties in achieving high hole concentrations in ZnSe:N in order to take advantage of tunneling transport. Although important advances have been made in forming low-resistance contacts to p-ZnSe [124,125], it is nevertheless desirable to develop methods for forming low resistance contacts between p-type ZnSe:N and p-type GaAs substrates. This will also allow for the fabrication of devices on p-type III-V buffers and substrates, while a readily achievable ohmic contact can be made to the n-side top contact layer *ex-situ*. By using III-V buffer layers of intermediate bandgaps, or alternatively, by

smoothly grading the alloy compositions from the bandgap of ZnSe to GaAs, the hole injection barrier can be reduced. Figure 4–2 (b) shows some of the single-layer, step-bandgap III-V buffer layers that have been fabricated. The performance of the III-V hole injection layer can be further improved by smoothly grading the composition of the buffer layer from InGaP near the GaAs substrate ($a_{InGaP}=a_{GaAs}$) to InAlP near the ZnSe ($a_{InAlP}=a_{ZnSe}$) as shown in Figure 4–2 (c).

Heteroepitaxy of ZnSe on Ge was the first set of materials to be studied because of the higher quality of the Ge wafers that were available at the time compared to GaAs, as well as its close lattice match with ZnSe. Difficulties arising out of polar on non-polar epitaxial growth, coupled with the advances in III-V epitaxial technologies and the advent of high quality GaAs substrates, soon shifted interest away from Ge.

To date, there has been a handful of reports on the use of alternative (i.e., other than GaAs) epitaxial III-V buffer layers for the growth of ZnSe with the specific aims of: (*i*) providing a lattice-matched starting surface, and/or (*ii*) to reduce the hole-injection barrier between the GaAs substrate and ZnSe-based structures. MBE growth of ZnSe on partially relaxed AlAs/GaAs [126,127], InGaAs/GaAs [126,128], InGaP (lattice-matched to GaAs and *ex-situ* transferred) [129,130],InGaAlP [131], as well as ZnSe on bulk InGaAs substrates [126] have been reported. At least one group has also taken the approach of growing a band-offset reduction layer of InAlP on top of the ZnSe epitaxial layer by MOVPE as a contact layer to p-type ZnSe [132,133]. We have also preliminarily reported high quality ZnSe epilayers on InGaAs and InGaP buffer layers (*in-situ* transferred) with lattice parameters that ranged from those of GaAs to ZnSe by both GSMBE and MBE [78,134]. ZnCdSe/ZnSe-based laser diodes have been recently demonstrated

successfully on InGaAs [128], as well as InGaP [135] and InGaAlP [136] buffer layers, where decreased operating voltages were observed due to the reduced hole injection barriers.

In addition, several reports on the MOVPE growth of ZnSe on InP have also been reported [137,138,139] where ZnSe was used as the widegap pseudo-insulator gates in field effect transistor devices. Motivation for the use of ZnSe in this case is to reduce the trap state densities that is possible with an epitaxial insulator, and to utilize the high Schottky barrier (e.g., >1 eV for Au-ZnSe) that can be easily obtained for the metal-ZnSe junction. MOVPE-grown ZnSe/Ge/GaAs and ZnSe/InGaAs/GaAs heterojunction bipolar transistors have also been demonstrated [140], making use of the large valence band offset offered by ZnSe when used as the emitter material.

However, a clear and causal illustration of the structural benefits that the various types of buffer layers (including the use of ZnSe bulk substrates) actually provide, e.g., reduced threading dislocation densities or prolonged device lifetimes, remain to be demonstrated. As part of our on-going studies of the II-VI/III-V heteroepitaxial growth process, ZnSe has been grown by GSMBE and MBE on various III-V epitaxial buffer layers on GaAs substrates. The following sections will describe the growth, as well as some preliminary results on the characterization of these heterostructures. In particular, the use of cathodoluminescence imaging as a mean of providing fast feedback on the structural qualities for these heterostructures grown under various conditions, will also be described.

(a) schematic band-alignment of ZnSe and GaAs

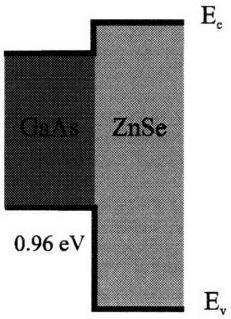

(b) abrupt-junction layer exploiting different surface chemistries offered by various III-V buffer layers

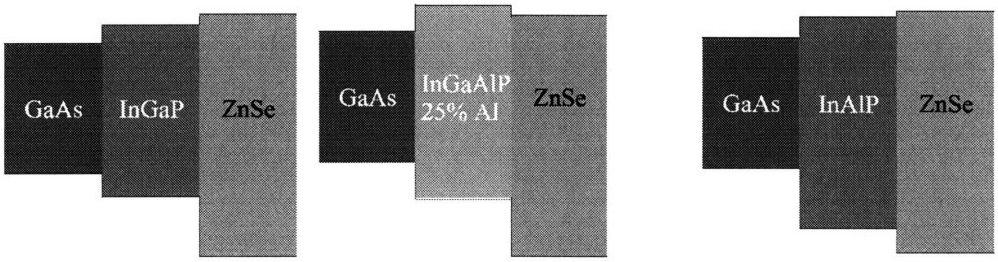

(c) graded-junction (In,Ga,Al)P buffer layer as hole injection layer

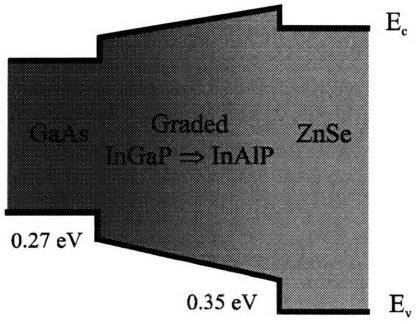

Figure 4–2 Energy bandgap alignment of ZnSe and GaAs and various proposed structures aimed at reducing hole injection barrier to p-ZnSe.

4.2 Growth and Characterization of ZnSe on III-V Buffer Layers

4.2.1 Experimental Procedure

As previously described in Chapter 3, the epitaxial buffer layers were grown in a Riber-CBE32P GSMBE chamber dedicated to the growth of III-V materials. Except for some earlier experiments where As passivation was used, nearly all of the samples were transferred *in-situ* in ~10^{-9} Torr vacuum into the II-VI chamber for subsequent ZnSe growth by MBE or GSMBE. Special surface treatment other than As- or P-overpressure was normally not used after the termination of the III-V buffer layers. Care was taken to ensure that the epitaxial GaAs grown in the III-V chamber maintains a stable RHEED pattern throughout the sample transfer process. RHEED intensity oscillations were nearly always obtained for ZnSe grown on *in-situ* transferred GaAs. Both of the above facts suggest that the transfer process does not significantly alter the surface condition of the GaAs epilayer. For other III-V buffer materials, it has been more difficult to correlate the RHEED pattern observed at the end of the III-V growth with those observed in the II-VI chamber after the transfer process. Some preliminary evidence suggests that surfaces containing a high Al-fraction may have a higher likelihood of exhibiting degraded RHEED patterns after the transfer process into the II-VI chamber. Nevertheless, in nearly all cases, RHEED intensity oscillations were still observed, indicating that the surface is still in a monolayer-smooth condition that allows for the layer-by-layer growth mode.

Table 4-1 shows a summary list of the various III-V layers that have been used as epitaxial buffer layers for the nucleation of ZnSe. Characterization methods that have been used include PL, X-ray as well as cathodoluminescence.

4.2.2 Photoluminescence Characterization

10K photoluminescence measurements indicated that the optical properties of the ZnSe layers grown on all types of buffer layers were typically comparable to or better than those observed for ZnSe grown on epitaxial GaAs. Figure 4–3(a) shows a typical PL spectrum of a pseudomorphic ZnSe (~ 1200 Å) grown on an InAlP buffer layer. The bandedge radiation that dominates the spectrum consists of an intense free exciton (E_x) feature and a weaker donor-bound exciton (I_2) feature with negligible deep level emissions. Note that under certain growth conditions, the E_x intensity was observed to be stronger than I_2. Qualitatively similar PL features were observed for undoped ZnSe grown on InGaP, InGaAs, and InGaAlP buffer layers. Because the entire structure as shown in Figure 4–3 is pseudomorphic, defects generated as a result of strain relaxation are not expected to play an important role in the observed optical properties. These results indicate that ZnSe of high optical quality can be compatibly grown on the various buffer layers without significant difficulties in nucleation even when In, Al and P atoms are present on the surface. This is further reinforced by the consistent observation of RHEED intensity oscillations which signifies that the ZnSe growth is occurring in the desirable layer-by-layer mode.

The PL of relaxed and undoped ZnSe films (film thicknesses much greater than the critical thickness of ZnSe) such as that of ZnSe grown on InAlP in Figure 4–3 (b) (as well as the spectrum shown previously in Figure 3–4 for ZnSe grown on partially relaxed InGaP), show the existence of weaker lines such as Y_o in addition to the normal bandedge features E_x and I_2. The existence of the extended defect-bound excitonic feature Y_o has been postulated to be indicative of the high structural quality of the ZnSe layers, which allows the excitons to be trapped and recombine on extended defects such as misfit dislocations [79,80,81,82]. Similar spectra have

Table 4-1 Listing of the various III-V epitaxial materials that have been used as buffer layers for the nucleation of ZnSe. The locations Z_1 and Z_2 are defined in the drawing below (a is the lattice constant).

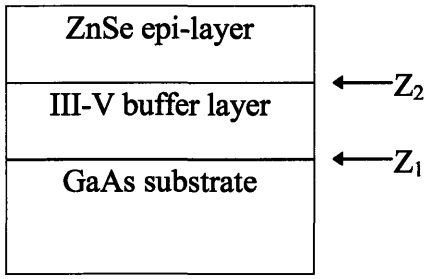

III-V Material	Transition	II-VI Material	a at Z_1	a at Z_2
bulk and epitaxial GaAs	-	ZnSe, pseudomorphic to 5 μm	a_{GaAs}	a_{GaAs}
InGaP	abrupt	ZnSe, pseudomorphic and 1 μm	a_{GaAs}	a_{GaAs}
InGaP	abrupt	ZnSe, pseudomorphic and 1 μm	a_{ZnSe}	a_{ZnSe}
InGaP	graded	ZnSe, pseudomorphic and 1 μm	a_{GaAs}	a_{ZnSe}
InGaAs	abrupt	ZnSe, pseudomorphic and 1 μm	a_{GaAs}	a_{GaAs}
InGaAs	abrupt	ZnSe, pseudomorphic and 1 μm	a_{ZnSe}	a_{ZnSe}
InAlP	abrupt	ZnSe, pseudomorphic and 1 μm	a_{ZnSe}	a_{ZnSe}
InAlP	graded	ZnSe, pseudomorphic and 1 μm	a_{GaAs}	a_{ZnSe}
InGaAlP	abrupt	ZnSe, pseudomorphic and 1 μm	a_{ZnSe}	a_{ZnSe}
InGaP->InAlP	graded	ZnSe, pseudomorphic and 1 μm	a_{GaAs}	a_{ZnSe}

been observed for ZnSe grown on InAlP (abrupt and graded), InGaAs (abrupt), as well as on graded InGaAlP buffer layers.

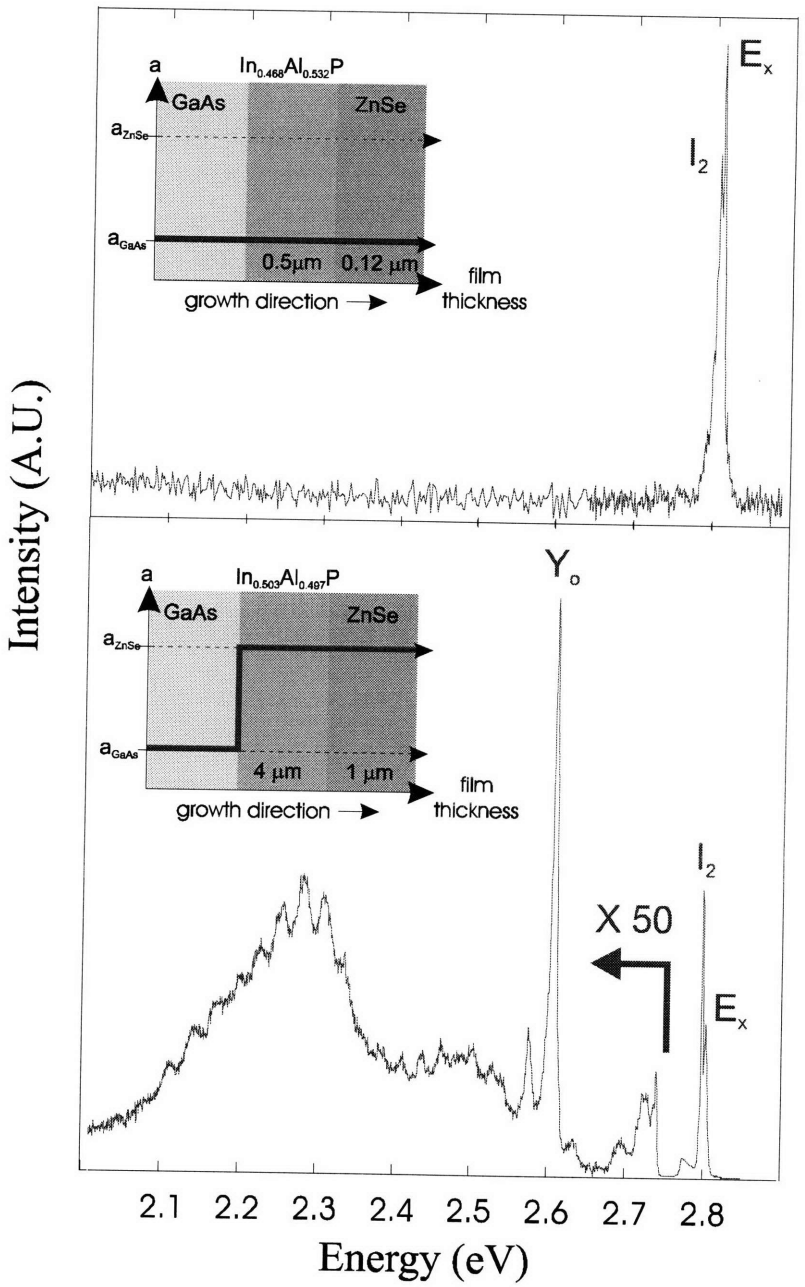

Figure 4–3 (a) 10K PL of pseudomorphic (0.12 μm) ZnSe on $In_{0.468}Al_{0.532}P$ buffers layer lattice-matched to GaAs (b) 10K PL of 1 μm ZnSe on 4 μm $In_{0.503}Al_{0.497}P$ buffer layer lattice-matched to ZnSe. The inset in each pane shows the schematics of the lattice constant variation as a function of layer thicknesses.

4.2.3 Cathodoluminescent Studies

Cathodoluminescence (CL) is a powerful and highly visual characterization technique that can be readily implemented in a standard electron microscopy apparatus. CL takes advantage of a focused electron beam's ability to generate a high density of electron-hole pairs in a solid state material, a portion of which may subsequently radiatively recombine. By providing for a means of efficient light collection while the instrument is operated in the SEM mode, two-dimensional luminescence information can be obtained. Coupled with a monochromator, various characterizations can be performed, including spectral analysis and wavelength specific luminescence mapping. The use of electrons of different accelerating energies further allows one to vary the depth in which the bulk of the electron-hole pairs are generated, thereby providing depth-resolved information. All of the CL data have been obtained on a JEOL JSM6400 SEM at MIT. Appendix C at the end of this thesis contains a more detailed discussion of the CL phenomenon, as well as some particulars of the CL apparatus used in this study.

For consistency, groups of samples to be compared with each other were usually mounted onto the same SEM sample holder using silver paint. Unless otherwise stated, most analyses were performed at an incident electron beam voltage of 20 keV, with typical probe currents ranging from 2-50 nA. The interaction volume of 20 keV electron beam was found to be > 2 μm for ZnSe under normal incidence (see Appendix C). Lateral resolution, although un-quantified, are thus believed to be on the order of 2 μm as well. An optical filter is normally placed at the entrance of the monochromator to block infrared radiation. A thermal-electrically-cooled photomultiplier with useful sensitivity range between 300-900 nm is used to detect the output from the monochromator; typical acceleration voltages for the photomultiplier are between 1000-1200 volts. Since it was possible to readily switch between the CL and SEM images, physical

features (such as sample edges and dust particles on the surface) were routinely used to ascertain the reasonableness of the obtained CL images, as well as to calibrate the brightness and contrast settings (see, again, Appendix C for more details). Most images and spectra were taken at room temperature; little additional spectral information were found at low temperatures using a 4 K cold stage.

Figure 4–4(a) shows a typical spectrum of a 1 μm thick undoped ZnSe layer grown on a bulk GaAs substrate (with its oxide thermally desorbed at ~ 580°C without an As-overpressure) by MBE, along with a two-dimensional map of the CL (Figure 4–4(b)) at the peak wavelength indicated by the arrow in Figure 4–4(a). Since the activation energy of the acceptors (E_A) is greater than that of the donors (E_D), the dominant feature in Figure 4–4(a) is most likely a FA (free-to-acceptor) feature at room temperature. Low temperature CL typically revealed spectra that were in general similar to those observed under PL excitation; however, fine structures observable by PL was typically not observed in low-temperature CL. This difference is attributed to the difference in the details of the excitation process, as well as the possible differences in the local excitation densities.

The characteristic pattern of bright background punctuated by arrays of dark regions as shown in Figure 4–4(b) has been observed for the majority of the ZnSe layers grown; the relative coverage of dark/white region, the orientation, density of the patterns, and the relative sizes of the dark and bright features differ depending on the growth and nucleation conditions. By analyzing the etch pit structures and their dependence on beam voltage and electron beam-induced current (EBIC) defect image contrasts, Schreiber et al. has concluded that it was possible in some cases to distinguish the different types of defects based on CL and EBIC image contrasts [141]. Bromine-based defect etch [142] carried out in our laboratory has indicated that typical ZnSe

films grown on GaAs contained ~ 10^6-10^7 etch pits per cm^2 (or EPD). These values are consistent with literature results for ZnSe grown on GaAs bulk and epilayers without special nucleation procedure. By assuming that the defect contrast manifested in Figure 4–4(b) consists of surface perpendicular dislocations which were shown to have point-like contrasts under CL [141], the "defect density" calculated in this manner is roughly 10^7 cm^{-2}. This agrees reasonably well with our EPD study results. Note, however, that because of the inherent limitation in lateral resolution during CL imaging, each of the "dark spots" could, in principle, consists of one or more closely spaced threading dislocations.

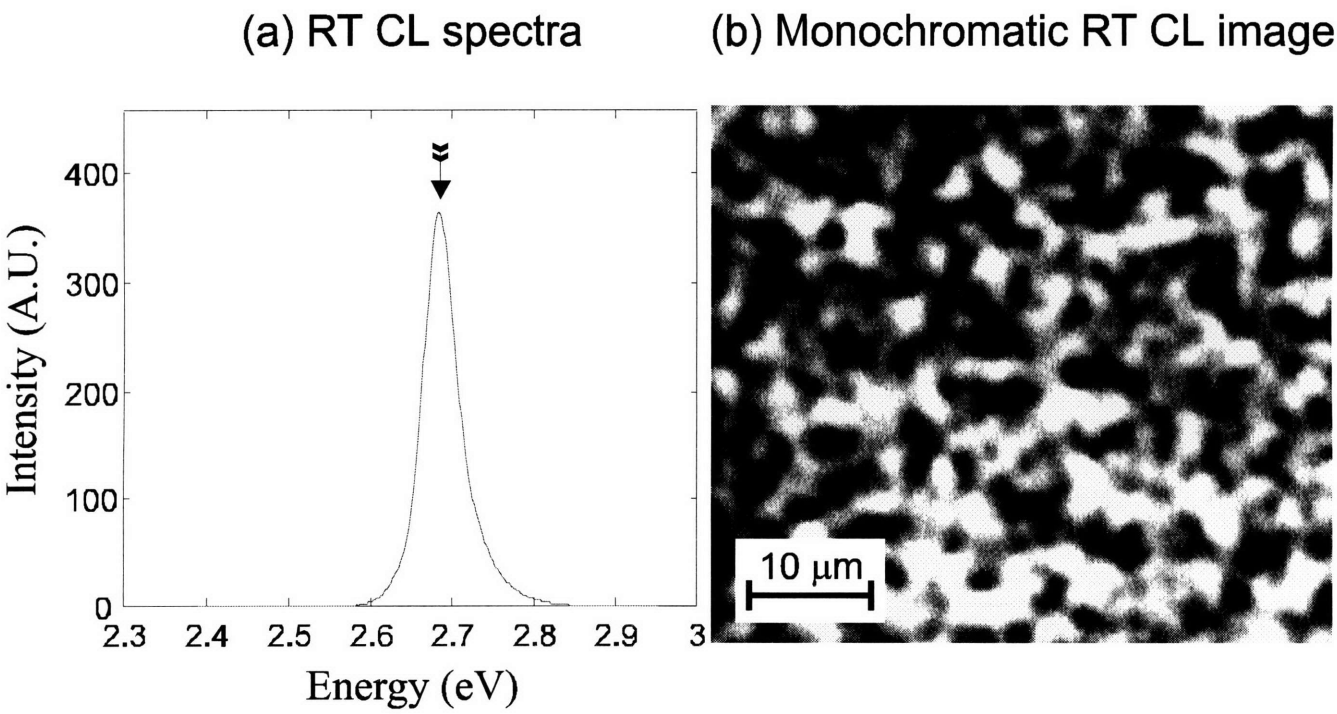

Figure 4–4 (a) Typical room temperature CL spectra of an unintentionally-doped ZnSe grown on GaAs epitaxial buffer layers by MBE. (b) Monochromatic 2-D CL map at the peak wavelength indicated by the arrow in (a).

Simultaneous TEM/CL observation of defect contrast [143] represents the ideal method to establish a direct correlation between the observed CL contrast pattern and actual defect arrangements that exist in the film, as well as spectral assignment of different defect-related luminescence. As this capability was not at our disposal, samples with known defect densities as revealed by EPD studies and confirmed by plan-view TEM imaging were obtained from Purdue University. Films examined were ZnSSe/ZnCdSe/ZnSSe quantum well injection laser structures with ZnMgSSe optical confinement layers. The entire structure was pseudomorphically grown on GaAs substrates with MBE-grown epitaxial GaAs buffer layers. Figure 4–5 shows the CL of two samples with large confirmed differences in their defect densities. The CL image as shown in Figure 4–5(b) was found to have nearly no observable contrast, suggesting that the defect density is $3x10^4$ cm^{-2} or below based on the magnifications used. The qualitative difference between the contrasts observed in the two images is clear. The estimated "point-like" defect densities were found to agree within a factor of 2-3 with the reported EPD's. These results demonstrate that CL imaging can be used to provide a non-destructive means of qualitative (or even semi-quantitative) feedback on the structural qualities of the ZnSe epilayers.

For ZnSe grown on the various III-V buffer layers under stoichiometric growth conditions, two effects are considered to be primary in determining the defect densities:

(1) The strain due to lattice mismatch between the in-plane lattice constants of the surface of the buffer layer and ZnSe. The relief of strain is expected to cause various extended defects in the ZnSe layer such as misfit dislocations, threading dislocations, as well as stacking faults at the ZnSe/buffer layer interface. Strain can also be introduced due to the difference in the thermal expansion coefficients of the two

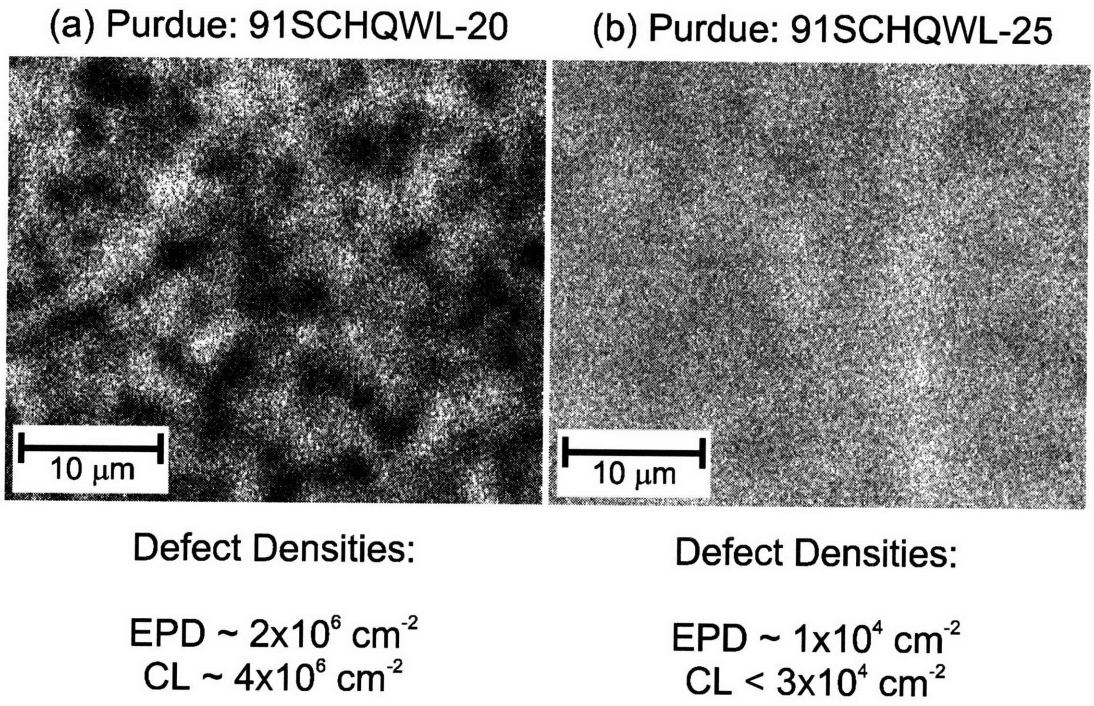

Figure 4–5 CL images of two pseudomorphic quantum well structures grown on GaAs epitaxial buffer layers obtained from Purdue. CL spectra were obtained under room temperature at their respective quantum well emission peaks under the following conditions: 30nA probe current and 20 kV acceleration voltage.

materials, as lattice matching conditions can only be precisely met at one temperature.

(2) The nucleation conditions of the ZnSe on the buffer layer surface can also lead to dramatically different defect densities. Nucleation conditions depend on numerous detailed parameters of the buffer layer surface, including smoothness, reconstruction patterns, chemical nature of the surface elements, etc.

Of course, growth conditions of the ZnSe overlayer, as well as surface contaminants at the III-VI/II-VI interface can also affect the observed defect densities: these conditions are assumed to be easily controllable and are not considered here. ZnSe films generally exhibit the best structural (by X-ray FWHM's) and optical (by PL) properties when the flux conditions are

approximately 1:1 (which is characterized by a mixture of 2x1 and c(2x2) RHEED reconstructions). Growth conditions that result in the three-dimensional mode of growth have been shown to proceed via an island formation/coalescence process which was speculated to lead to a large number of dislocations [144].

The effect of the lattice mismatch on the defect densities of the overlayer is generally well recognized: layer thickness beyond which the strain can be elastically accommodated will lead to defect formation in order to reduce the strain. Considering that both lattice mismatch strain and nucleation phenomenon can lead to the formation of defects, minimum defect densities are likely to be achieved most easily in a lattice-matched system of materials. Consequently, all laser diodes demonstrated thus far in the II-VI system have been nominally pseudomorphic systems based on the lattice constant of the GaAs substrate in order to minimize strain-related defects. The effect of the nucleation condition on the defect densities of the ZnSe, however, still lacks a clear consensus among researchers, as evidence by the sometimes contradictory reports in the literature. Perhaps the most comprehensive studies thus far reported of the effect of surface stabilization on defect formation are collaborative efforts of the 3M Company and University of Maryland [117,145,146]. In their studies, lattice-matched or near-lattice-matched ZnS_xSe_{1-x} were grown by MBE in order to minimize the contribution from lattice-mismatch related defects. Using TEM to analyze the effect of Zn- or Se-treatment on Ga- or As-stabilized epitaxial or bulk GaAs, the authors claimed that the lowest stacking fault densities of ~ 10^4 cm^{-2} were obtained using Zn-treatment on As-stabilized epitaxial GaAs surface. The authors believed that with Zn-treatment of an As-rich GaAs surface, the defect density can be minimized through the prevention of the formation of a Ga_2Se_3 thin layer which contains vacancies that can serve as sites for stacking fault nucleation at the interface.

Ruvimov et al. has also reported stacking fault densities in the 10^4-10^5 cm^{-2} range for ZnSe grown on As-terminated GaAs substrates by MOVPE [147], although it was performed without intentional Zn-treatment. Studies of the deep level defects have further shown that the 1.9-2.0 eV self-activated defect (which has been associated with Zn-vacancies and Ga atoms on Zn sites [148,149]) generated by thermal annealing is enhanced by Se-rich nucleation conditions but retarded by Zn-rich ones [150]. Other authors, however, have reported that a Se-stabilized GaAs surface exhibits stronger excitonic near-bandedge PL [151,152] as well as narrower linewidths [153]. In one study, As-deficient GaAs epilayers were found to result in structures having lower interface state densities at the ZnSe/GaAs interface compared to As-rich starting surfaces [154].

Although the evidence thus far seems to indicate that the contribution to defect formation associated with nucleation conditions can be minimized by the use of As-terminated epitaxial GaAs, further complication arises when one considers the electrical properties of the ZnSe/GaAs structure. A set of studies have concluded that the valence band offset, ΔE_V, can be tuned between 0.6 and 1.2 eV if the stoichiometries of the first few nanometers of ZnSe were grown under Se-rich or Zn-rich conditions, respectively [152,153,155]. The low ΔE_V of the Se-rich nucleation conditions will be beneficial for devices requiring hole injection across the ZnSe/GaAs heterobarrier, but may prove to yield structures with higher defect densities that can adversely affect the device lifetime.

We have also performed some preliminary investigations studying the effects of nucleation conditions and lattice-mismatch strain on defect densities as observed by CL. Although different epitaxial III-V buffer layers lattice-matched to ZnSe have been used, nearly all of the ZnSe grown on these samples showed characteristic patterns of dark spots on a bright background, indicating that a substantial amount of threading-type dislocations exists. Because most of these films were

grown without special surface treatment, we believe that nucleation-related defects are dominating over the beneficial effects of the lattice-matched buffer layers. In other words, when special care was not taken during the nucleation stage, the nucleation-related defects are sufficient in number such that the preferred misfit dislocations are not formed. Since misfit dislocations are not expected to be present in a lattice-matched ZnSe/III-V buffer system, the observed CL contrasts were believed to be directly related to nucleation-induced defects. It is worthwhile to point out that unless special care is taken to preserve the RHEED reconstruction patterns of the freshly-grown III-V layers, the high vapor pressure of the hot Se cell may introduce a sufficient amount of Se at the surface to always yield a Se-decorated III-V surface. For example, transition from a c(4x4) to a 2x1 reconstruction in GaAs have been observed when the GaAs surface was intentionally exposed to a Se flux.

By varying the nucleation conditions of the starting GaAs surface, dramatic changes in the RT CL have been observed. Figure 4–6 shows a comparison of a "spotty" pattern with point-like contrast that we typically observe (Figure 4–6(a)) with some other noteworthy CL images that were found to be qualitatively different. Notice that in Figure 4–6(a), a substantial number of threading-type dislocation contrast features are observed even though the linearly graded InGaP→InAlP buffer layer was found to be closely lattice-matched to the undoped ZnSe overlayer. Figure 4–6(b) shows a CL image taken under similar conditions for undoped ZnSe grown on a InGaAs buffer layer lattice-matched to ZnSe. The system of dark lines is believed to result from misfit dislocations at the ZnSe/InGaAs interface oriented along two orthogonal <110> directions. As misfit dislocations are not expected to be prevalent in lattice-matched systems, it is possible that the defect contrast in the ZnSe that is observed here is influenced by

the morphology of the underlying InGaAs buffer layer, which was found to exhibit strongly cross-hatched surface morphological features oriented along the same directions.

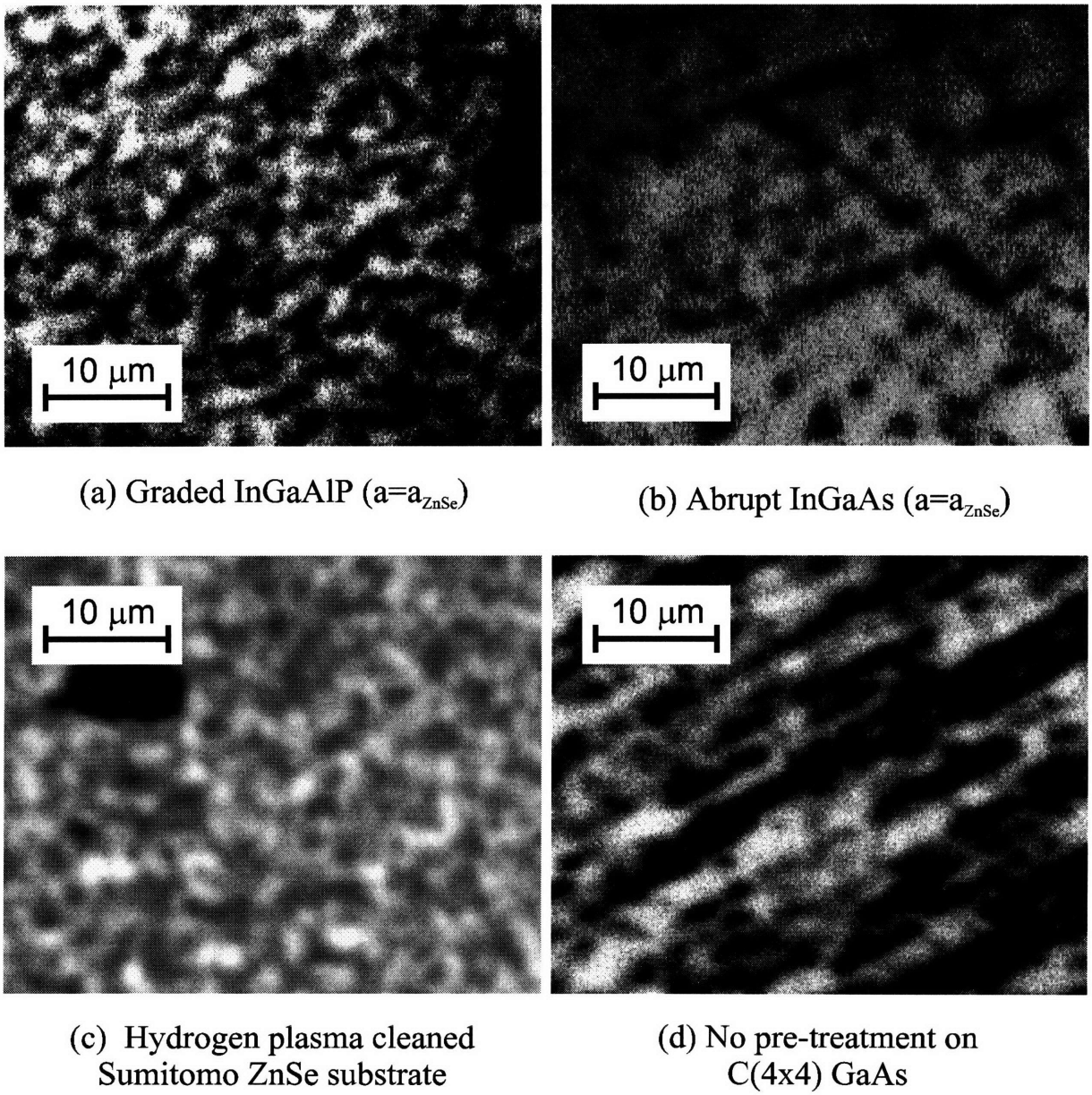

(a) Graded InGaAlP ($a=a_{ZnSe}$)

(b) Abrupt InGaAs ($a=a_{ZnSe}$)

(c) Hydrogen plasma cleaned Sumitomo ZnSe substrate

(d) No pre-treatment on C(4x4) GaAs

Figure 4–6 Comparison of various CL images taken at room temperature, recorded at the wavelengths of the dominant peaks observed in the CL spectra. All ZnSe samples were undoped and approximately 1 μm thick. Images were taken under the following conditions: 20 kV acceleration, and ~ 30 nA probe current. The large dark spot in (c) near the 10 μm marker is due to a surface contaminant (confirmed by SEM imaging of the same area) and is useful as a reference for a non-emissive or "dark" region.

Figure 4–6(c) shows the CL image for a homoepitaxially-grown ZnSe on a hydrogen plasma-cleaned Sumitomo ZnSe bulk substrate. Since homoepitaxially-grown ZnSe is not expected to have dark line contrasts, the "spotty" image as seen in Figure 4–6(c) indicates that nucleation-related defects are abundant in the film. The CL contrast as shown in Figure 4–6(d) is believed to be composed of mostly misfit dislocations that are generated at the ZnSe/GaAs interface as a result of strain accommodation. In this particular film, a sharp c(4x4) (~ 100% As-covered) reconstructed GaAs epilayer was maintained until just before the ZnSe nucleation by simultaneous exposure of Zn and Se fluxes. The increased segment length of the misfit dislocations suggest that the threading-type dislocation densities may be reduced.

Figure 4–7 shows CL images taken at 10K and at room temperature for an undoped ZnSe film containing an interfacial layer (4-5 monolayers) of ZnSe grown at a low-temperature (~

ZnSe on Zn-exposed, low temperature nucleated C(4x4) GaAs

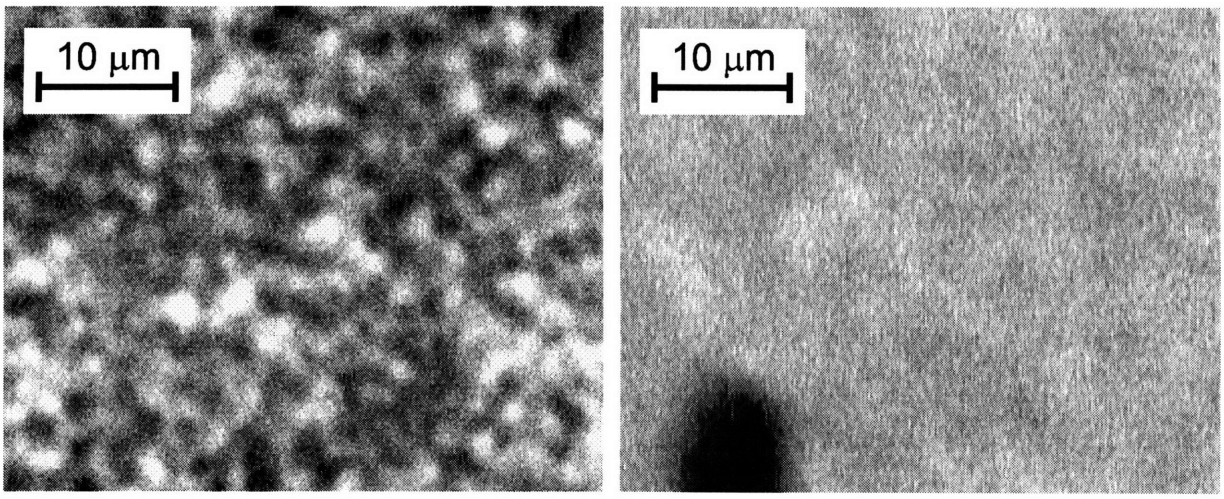

(a) ~10 K (b) ~ 300 K

Figure 4–7 CL Images of a low temperature nucleated and Zn-exposed ZnSe grown on C(4x4) GaAs at (a) 10K and (b) 300K.

210°C). The remaining 1 μm was then grown at an elevated growth temperature of ~ 280°C, which is a typical temperature for undoped ZnSe. Compared to the CL images of other films at room temperature, Figure 4–7(a) appears generally brighter, with less dark/white contrasts. These differences were even more dramatic during low temperature CL imaging (Figure 4–7(b)), where a nearly featureless image was obtained. The resolution of the CL technique is expected to be significantly degraded at low temperatures due to several effects: (*i*) the increased minority carrier diffusion length; (*ii*) the reduced non-radiation recombination around the dislocation cores; and (*iii*) increased radiative lifetime of the excitonic emission mechanisms. Comparisons of the apparent changes in resolution among different films at low and room temperatures, however, suggest that this particular film may be microstructurally somewhat different from the rest. It has been speculated that nucleation at lower-than-usual substrate temperatures, coupled with special nucleation procedures, may be promising in reducing the defect densities as determined by EPD analyses [156]. The reason for the dramatic differences in the CL images as shown in Figure 4–7 is unclear and currently under investigation.

Our most recent results of systematic nucleation studies have been highly encouraging. In a set of ZnSe growths on epitaxial GaAs with controlled nucleation, several parameters have been systematically varied to understand their effects on defect properties. These parameters include: (*i*) the use of Zn or Se pre-exposure; (*ii*) c(4x4) or 2x4 reconstructed GaAs buffer layers; and (*iii*) the use of migration enhanced epitaxial (MEE) nucleation layers. The most important conclusions derived from these experiments are embodied in Figure 4–8. For comparison, Figure 4–8(a) shows the room-temperature CL image of a 1 μm ZnSe film grown on c(4x4) GaAs buffer layer using 120 seconds of intentional Se pre-exposure before normal ZnSe growth with simultaneous supply of Zn and Se fluxes. Upon Se pre-exposure, the GaAs buffer layer

reconstruction typically changes from a sharp c(4x4) to a fainter 2x1 pattern. Because of the high vapor pressure of Se, prolonged exposure of GaAs buffer layers to the background fluxes in the II-VI chamber prior to growth often results in similar reconstruction patterns. The CL image as shown in Figure 4–8(a) can be seen to be qualitatively similar to those films grown without special nucleation procedures (for example, see Figure 4–6(a)). In Figure 4–8(b), the use of ~ 40 monolayers of MEE-grown ZnSe at a slightly lower growth temperature (20°C below normal) clearly led to reduced dark spot defect densities in the CL image. Furthermore, formation of some misfit dislocation segments can also be observed. These results are in agreement with reports where ZnSe films grown using MEE were found to have superior structural properties compared to films grown using simultaneous supply of Zn and Se fluxes [157,158].

As shown in Figure 4–8(c), the most dramatic difference in the CL images were obtained when 120 seconds of Zn pre-exposure were used on a 2x4 reconstructed GaAs epilayer[‡] (which is less As-rich compared to a c(4x4) GaAs). Characteristic defect contrast was not observed in repeated imaging of the immediate vicinity of the area shown in Figure 4–8(c). Using the fact that no observable defect contrast can be seen in the figure, the defect density is expected to be « 10^5 cm^{-2}. Note that the two large dark spots in the upper right-hand portion of Figure 4–8(c) are dust particles (confirmed using simultaneous SEM imaging). Another film grown under similar conditions was found to exhibit a similarly featureless CL image. It is still unclear what physical mechanism is responsible for the dramatic changes observed in films grown on Zn-exposed 2x4 GaAs buffer layers. Work is currently underway to further investigate this issue and to extend these results to other III-V buffer layers that can be lattice-matched to ZnSe.

[‡] We are grateful to Professor Fitzgerald for his suggestion that 2x4 GaAs may lead to different defect properties.

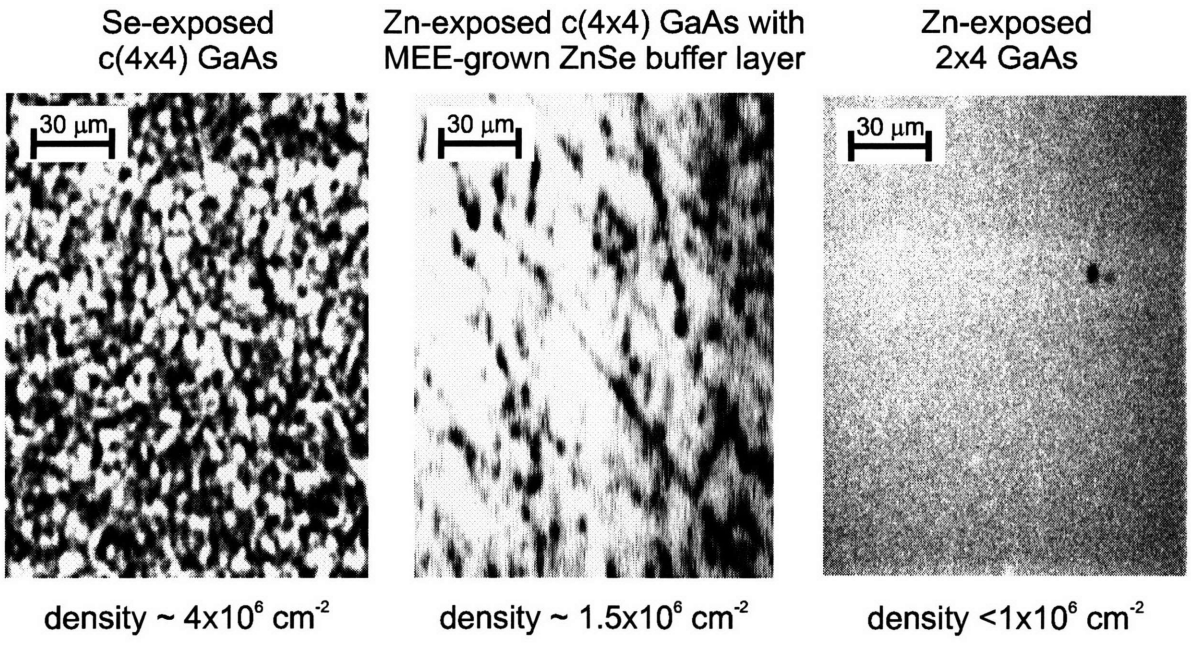

Figure 4–8 Effect of different nucleation procedures on the defect properties of ZnSe grown on GaAs epitaxial buffer layers: (a) c(4x4) GaAs pre-exposed with Se for 120 seconds; (b) ~30 monolayers of MEE-grown nucleation layer grown at ~ 20°C before normal growth temperature; (c) 2x4 GaAs pre-exposed with Zn for 120 seconds.

Our preliminary results thus far can be summarized as the following:

(1) Those films where the growth did not proceed in a layer-by-layer manner (as indicated by RHEED intensity oscillations) generally resulted in highly "spotty" or "point-like" contrasts with high (>10^7 cm^{-2}) apparent CL defect densities.

(2) Thermally-induced Ga-rich surface exposed with Se, as well as those films that were allowed to become decorated by Se in the II-VI chamber regardless of the lattice matching conditions of the buffer layer, also showed highly "spotty" and "point-like" contrasts, with CL defect densities ranging from 10^6 cm^{-2} and above.

(3) Under the proper nucleation conditions, defects that are mostly of the misfit dislocation type can be obtained. In these cases, the CL images are composed of dark-line contrasts of various lengths.

(4) The nucleation condition was found to play a crucial role in determining the defect properties of the ZnSe films grown on GaAs. Best results as determined by CL imaging have thus far been obtained for ZnSe grown on Zn-exposed, 2x4 reconstructed GaAs epitaxial buffer layers.

Control and minimization of the two crucial defect generation mechanisms, i.e., strain- as well as nucleation-induced defects, will be pivotal for the successful application of III-V hole-injection buffer layers to II-VI light emitting devices, as any threading dislocations that reach the active layer of a laser diode will be detrimental to its lifetime. Further studies are underway to ensure the repeatability and to extend our preliminary results to other III-V buffer layers. It is believed that the defect density (particularly those due to threading dislocations) of ZnSe grown on GaAs buffer layers can be substantially decreased by using optimal nucleation conditions; minimum defect densities are expected when these growth and nucleation procedures are applied to ZnSe grown on III-V epitaxial buffer layers designed to minimize lattice-mismatch strain.

4.3 Suggestions for Future Work

Although we have not yet been able to demonstrate the primary goals of the II-VI/III-V heteroepitaxy study using alternative buffer layers, i.e., reduced hole injection barriers and minimized defect generation, our results do show that ZnSe layers of high optical and structural quality can be achieved. It is also clear that substantial opportunities lie ahead in the search and

characterization of an "ideal" buffer layer: this "ideal" buffer layer would have the desirable properties such as good lattice-matching to ZnSe, compatible thermal expansion coefficient, compatible chemical surface for the nucleation of ZnSe, and can be grown such that the surface presented for ZnSe nucleation has minimal threading dislocations that could propagate into the II-VI active regions.

Short- to medium-term recommendations for the II-VI/III-V heteroepitaxial work is briefly discussed as follows:

(1) More detailed and systematic studies should be carried out to confirm and expand on the very encouraging results observed thus far for the nucleation studies of ZnSe on GaAs. The effect of variations in the duration and the substrate temperature of Zn-exposure treatment should be examined. Additional insights into the mechanism for the dramatic effect of the starting GaAs surface on CL images may also be gained by using GaAs wafers with different miscut angle and orientations. Comparison with other microstructural characterization techniques such as cross-sectional and plan-view TEM and EPD studies should be carried out to confirm that the defect densities are indeed low.

(2) The motivation for the initial studies on GaAs has been twofold: First is to add to the existing body of data pertaining to the growth of ZnSe on GaAs. It is important to keep in mind that few epitaxial systems are equipped with dedicated and interconnected UHV growth chambers, and that most blue-green II-VI laser diodes are presently grown on GaAs buffer layers. The second reason is that results on GaAs epilayers should be transferable to other buffer layers such as InAlP and InGaP buffer layers that are expected to be effective hole injection layers. If a 2x4 GaAs

starting surface with Zn-pretreatment is confirmed to be optimal for ZnSe growth on GaAs, similarly optimal nucleation procedures should be found for other material combinations such as InGaP and InAlP. An alternative approach would be to grow just enough pseudomorphic GaAs (8-10 monolayers) on other III-V buffer layers lattice-matched to ZnSe in order to obtain the desired surface reconstruction. In this manner, surface chemistry can be removed as a parameter while simultaneously achieving lattice-matching to ZnSe.

(3) After an optimal nucleation method has been affirmed, the obvious next step would be to fabricate simple diode structures for I-V studies to demonstrate the effectiveness of these alternative buffer layers. As it has been reported that the band offsets at a heterojunction can be tailored by changing the nucleation conditions [152,153,155], similar studies should be carried out in these III-V hole injection buffers to further minimize the valence band offsets without compromising structural quality. Investigations into the use of strain-layer superlattices may also bear fruit in controlling the defect formation of the II-VI overlayers.

(4) CL image analysis described above has been shown to be a fast, direct, and effective method to characterize the defect properties of the ZnSe epilayers. Systematic studies of the effect of buffer layer surface reconstruction, pre-exposure, and the effect of doping on misfit dislocation formation [145,159,160], lend themselves easily to CL comparisons. Coupled with TEM and EPD studies, opportunities abound in advancing our knowledge of heterointerface nucleation properties on these novel buffer layers.

As the future longevity of the II-VI research field is by now inexorably tied to the longevity of the II-VI laser diodes which, in turn, depends in a large part on the interfacial quality of the II-VI/III-V buffer layer, the successful application of these novel buffer layers should represent a major boost to the future viability of the II-VI devices.

5. *Concluding Remarks*

Motivated by the success of the alternative gaseous source techniques in the growth of III-V compounds, particularly those containing high vapor pressure elements such as arsenic and phosphorous, we have investigated the growth of the archetypical wide bandgap II-VI compound ZnSe using MOMBE and GSMBE. Combining the ability to perform various *in-situ* characterizations in an UHV background with the ability to deliver precise gaseous fluxes of the high vapor pressure sulfur and selenium (both vapor pressures being greater than arsenic or phosphorous), both of these alternative gaseous methods may hold the key to reproducible growth of various II-VI compounds requiring precise lattice matching with the underlying substrate material.

Our investigation into the MOMBE of ZnSe using diethyl metalorganic sources was initially met with the puzzle of extremely low growth rates, despite the wide variety growth conditions employed. Photo- and electron-beam illumination during growth, however, was found to be an effective method of relieving the ethyl-blockage phenomenon that is believed to be the culprit of the low growth rates. The large growth rate enhancement ratios observed suggest that selective epitaxy, as well as the very low temperature growth of ZnSe, are possible under the appropriate conditions. However, for large-area epitaxy of ZnSe, the use of ethyl-based precursors is at best cumbersome. The viability of this epitaxial technique as applied to the II-VI materials was ultimately limited by source purity considerations at the time of the research. These source purity issues led us to the use of hydride sources as group VI precursors because of their proven purity. Together with the use of the more well-behaving elemental Zn, we then migrated our efforts to

the GSMBE growth and doping of ZnSe. ZnSe epilayers with high optical and structural qualities were obtained by GSMBE, as were highly n-type ZnSe:Cl films using $ZnCl_2$ as the dopant source. Extension of the plasma nitrogen doping that has been proven to be moderately successful in MBE-grown ZnSe:N, however, was found to yield curiously different results. Hydrogen was quickly identified to passivate the incorporated nitrogen acceptors, with clear evidence derived from both electrical and SIMS measurements. Coupled with results from intentionally hydrogenated MBE-grown ZnSe:N, it was pointed out that not only does the sub-hydride species contribute to the observed electrical passivation, sufficient amount of ambient H_2 can also provide substantial passivation. Variation in the growth and cracking parameters was found to be unable to reliably produce samples with sufficient hole conductivity. The chemical simplicity afforded by the GSMBE technique, compared to metalorganic-based ones, appeared in this case to have transposed from an asset into a liability, in the sense that one is limited in terms of what can be done to affect the hydrogen incorporation chemistry at the growing surface. These results have wide ramifications for the application of not only the GSMBE techniques, but also to other MOVPE techniques where a large amount of H_2 ambient may be present.

In light of these GSMBE and the intentional hydrogenated MBE results, complete avoidance of the hydrogen passivation for as-grown samples may be extremely difficult. Minimization of the growing surface's exposure to hydrogen or hydrogen containing species during nitrogen doping, along with the appropriate post-growth thermal treatment, may be the best procedure to achieve highly conducting p-type ZnSe. Microstructural studies of the variously hydrogenated sample and modification of the H_2Se cracking conditions are expected to shed more light on the hydrogenation problem in future works.

Meanwhile, rapid advancement has been made in the nitrogen p-type doping of ZnSe and injection diode performances, although an upper p-type doping limits in ZnSe of mid to high 10^{17} cm^{-3}, and laser lifetimes on the order of hours, still confront the II-VI community. Coupled with strong competition from III-V nitrides, it appears that the field of II-VI research is now at a critical juncture in its development such that its future viability is at stake. Much of the community's attention has since been redirected back to several basic but critical issues: injection of holes into the II-VI structures, increasing the p-type doping ceiling of the ZnSe-based II-VI's, and the details of the II-VI/III-V interface defect formation. As part of our continuing and parallel investigations into II-VI/III-V heteroepitaxy, we have also investigated the use of various III-V epitaxial buffer layers for the heteroepitaxy of ZnSe. The two-pronged aim of these studies aspires to provide not only reduced hole injection barrier by the use of lattice-matched III-V buffer layers, but also to understand what effect these chemically novel surfaces have on defect formation in the ZnSe overlayer. The flexibility afforded by the use of lattice-matched, linearly graded buffer layers, or even strained superlattices holds much promise for understanding the basic issues of heteroepitaxy. Further enhancing the flexibility is the fact that the ZnSe layers can in principle be grown using metallic, hydride, or even metalorganic sources in a single chamber. Combined with available characterization methods such as AES, X-ray diffraction, SEM/TEM, PL and CL and various electrical measurements, ample opportunity still exists for exciting and original contributions to the advancement of the widegap materials arena.

Appendix A Secondary Ion Mass Spectrometry

A.1. Introductory Comments

Secondary ion mass spectrometry (SIMS) has gained prominence in the last two decades as the de-facto compositional analysis technique of choice for the field of semiconductor research and development. Elemental sensitivity is in the parts-per-million range (p.p.m, or 10^{-6}), with improvement to the part-per-billion (p.p.b.) range possible under optimal conditions. This is to be compared with other composition-sensitive techniques such as Auger Electron Spectroscopy (AES), X-ray Photoelectron Spectroscopy (XPS) and Electron Probe Microanalysis (EPMA) where typical sensitivities are in the 10^{-3} to 10^{-4} range. To help place the SIMS method in perspective with its myriad of particle microprobe siblings, Table A.1 shows the probe ("input")

Table A.1 Comparison of Analytical Particle Beam Techniques

Techniques	*Acronyms*	*Probe Species*	*Detected Species*
Secondary Ion Mass Spectrometry	SIMS	Ion	Ion
Secondary Neutral Mass Spectrometry	SNMS	Ion	Ionized Neutral
Fast Atom Bombardment	FAB	Neutral Atoms	Ion
Laser Microprobe Mass Analysis	LAMMA	Photon	Ion
Scanning Electron Microscope	SEM	Electron	Electron
Cathodoluminescence	CL	Electron	Photon
X-ray Photoelectron Spectroscopy	XPS	X-Ray	Electron
Transmission Electron Microscope	TEM	Electron	Electron
Electron Probe Microanalysis	EPMA	Electron	X-Ray
X-ray Fluorescence	XRF	Photon	X-Ray

and the detected ("output") species for some popular analytical techniques[§]. All of these methods (including the cathodoluminescence technique to be described later) depend upon the detection of the by-products of an energetic particle beam with the host material; the optimal choice of a particular technique depends on the type of information desired. A large body of empirical and (to a lesser extent) theoretical knowledge base is available today pertaining to the SIMS technique in the scientific literature. Interested readers are referred to references [161,162,163,164] for in-depth discussions of the SIMS technique.

The advantages of the SIMS (and SIMS-related) technique as applied to semiconductor compositional or impurity analysis may be summarized as follows:

(1) SIMS has high elemental sensitivity in the p.p.m. to p.p.b. range.

(2) SIMS is a mass spectrometric method; all elements and their isotopes can be analyzed. This is particularly important in the analysis of hydrogen, which is normally difficult to detect.

(3) SIMS is inherently surface specific, as the exit depth of the sputtered particles is only a few atomic layers from the impact surface.

(4) SIMS can also be used to obtain depth profiles by sputtering away successive atomic layers using a high flux of primary ions.

(5) Similar to the principles of SEM, two-dimensional ion images can be obtained when the instrument is operated in the ion-microscope mode, where an optimally focused ion beam (with diameter as small as 40 nm) is rastered across the surface.

[§] For an excellent comparison overview of SIMS with other surface-sensitive analytical techniques, see Chapter 7 of Reference 162.

Therefore, SIMS is a versatile, highly sensitive and conceptually simple analytical tool for many types of analyses, including surface, bulk and chemical-structural analysis. But unfortunately, there are prices to be paid for such flexibility. The disadvantages of the SIMS (including the SIMS-variant techniques) include:

(1) The analysis process is generally destructive, although in the static-SIMS mode, the monolayer lifetime can be made sufficiently long to complete measurement by lowering the beam current significantly and improving the secondary ion collection efficiency.

(2) The sputtering process that generates the secondary ions is not well understood theoretically, although a large body of experimental and empirical knowledge exists.

(3) The complexity and the lack of sufficiently accurate modeling of the sputtering process result in difficult quantitation (conversion from instrument ion counts to actual atomic concentrations) of the raw data. This task is further complicated by the fact that ion yields depend on a wealth of parameters and can vary by as much as six orders of magnitude. Thus, a system of *consistent implementation* of standards is critical for accurate analysis.

(4) Due to the wealth of secondary ions, ion clusters, and background impurities that might be present in the analysis environment, one must always be aware of the possibility of mass interference (due to signals having similar mass/charge ratios) in interpreting the mass spectra.

(5) Although insulating samples can in principal be analyzed, avoidance of deleterious sample charging effects can be quite difficult in practice.

The following section will discuss these topics in more detail.

A.2. Basic Principles of SIMS Analysis

A simple conceptual description of the SIMS process can be stated as follows: A sufficiently bright source of high energy primary ions (PI) are produced, optionally energy- and mass-filtered, and focused onto a solid or liquid sample. These primary ions (with energies up to tens of kilovolts) collide with atoms in the sample, causing cascades of other collisions in the immediate vicinity of the PI impact site. The primary ions, after imparting their energy to the host sample to create a wealth of interaction by-products, are typically stopped within tens of nanometers of the surface. Some of the secondary collision cascades eventually cause various species to leave the sample surface (normally from the first few surface layers only), including neutral atoms and clusters, ionized atoms and clusters, as well as secondary electrons, x-rays, photons, etc. This is in essence the process of sputtering. The positive or negatively charged secondary ions (SI) are collected and passed through a mass spectrometer, which is usually of the magnetic sector, quadrupole, or time-of-flight variety. The properly selected species is then counted by an ion counter such as a Faraday cup or an electron multiplier. The ion beam can be rastered over a sample area to provide two-dimensional ion information, or displayed as secondary ion images analogous to secondary electron microscopy (see Figure A.1). In *dynamic SIMS*, the primary ion current is sufficiently high to cause enough material to be eroded as the beam is rastered over an area to provide depth-resolved information. On the other hand, using a low current, well-focused primary ion beam and efficient secondary ion collection, the *static SIMS* mode of operation is possible where the area under study is not significantly altered before the analysis is completed.

From these basic modes of operation, variants have since been devised to address specific problems associated with the SIMS measurement and quantitation processes. For example, fast atom bombardment (FAB) mode utilizes a beam of neutral atoms to produce ionized secondaries in order to decrease the effect of sample charging by the primary ions. Secondary neutral mass spectrometry (SNMS) aimed to circumvent the problem of the wide variability in the SI yield by collecting the neutral sputtered species and post-ionizing them prior to detection.

Figure A.1 shows a simplified schematic of a typical SIMS apparatus. Common to all SIMS apparatuses are several key components: the primary ion source, the sample manipulation stage and the mass spectrometer/ion counter. For detailed discussions of each of the key components as well as discussions of the present state-of-the-art in the understanding of the complex

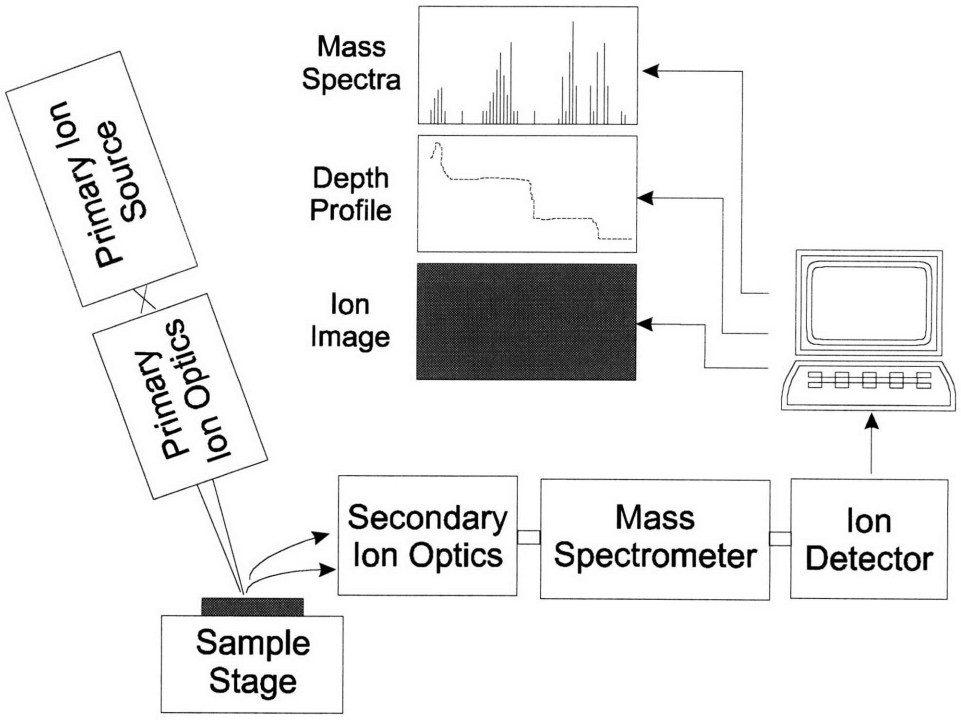

Figure A.1 Building-block schematics of a typical dynamic SIMS system showing only the essential components.

sputtering process, readers are again referred to the general references cited in the previous section. Electro-magnetic or electro-static lenses are used to focus and to collect the primary and secondary ions. Some machines are equipped with low energy electron guns (<1 keV) to combat sample charging. For dynamic SIMS, where high sensitivity (equates with high SI yield) is required, a Cs^+ surface ionization source or oxygen plasma source of O^- or O_2^+ are commonly used. These PI's can greatly increase the yield in some matrices through reactive chemical effects. When a liquid Ga source is available, it is possible to reduce the focused ion beam diameter to tens of nanometers for improved lateral resolution. The ions emerging from the sources are sometimes passed through a mass and/or energy dispersive filter to reduce contamination and provide ions with a uniform energy.

The requirements of the sample manipulation stage are straightforward: provide the basic necessary translational movement; must not outgas significantly; and must be electrically grounded. The choice of sample stage geometry can also affect the detection limit (the signal level below which a desired mass signal is not separable from noise) of the SIMS apparatus. The detection limit can be improved, for example, by mounting the sample slightly elevated relative to other exposed surfaces of the mounting stage.

The three commonly used mass spectrometric techniques of magnetic sector, quadrupole, and time-of-flight, have different operating characteristics that make them suitable for different applications. Table A.2 shows a comparison of the three common mass spectrometric techniques and their particular advantages and disadvantages. The choice of spectrometer for a particular type of analysis depends on the mode of SIMS being used, the nature of the matrix (the host material in which the desired impurities are embedded), and the species to be detected. For example, in semiconductor impurity analysis where low-mass elements may be present, magnetic

Table A.2 Comparison of Mass Spectrometric Techniques used in SIMS Instruments

	Quadruple	**Magnetic Sector**	**Time-of-Flight**
Mass Resolution m/Δm	10^2-10^3	10^4	$>10^3$
Mass Range (a.m.u.)	$\leq 10^3$	$>10^4$	10^3-10^4
Transmission*	1-10%	10-50%	50-100%
Advantages	Fast switching between mass peaks; simple to operate; low cost	high mass resolution	parallel mass detection; high SI transmission
Disadvantages	limited mass range; low mass resolution; low energy acceptance window for SI	Requires careful alignment of SI optics to achieve good transmission	Requires pulsed generation of SI

* fraction of the selected ions that can pass through the spectrometer.

sector mass spectrometers may be the most suitable candidate; for biological, organic, or polymeric samples, time-of-flight spectrometers may be the most suitable.

The remainder of this section will discuss some of the difficulties (or at least processes that a well-informed consumer of SIMS-for-hire service should be aware of when interpreting the SIMS results) that are inherent in the SIMS measurement and quantitation processes. The next section will single out those issues that are particularly important in the SIMS analysis of hydrogen, nitrogen and chlorine in ZnSe samples.

Secondary Ion Yield

In theory, given the secondary ion yield Y for a particular species in a material, the absolute concentration can be unambiguously calculated. Nevertheless, Y has been known to vary over six orders of magnitude depending on, among other things, the detected species, the structural, chemical and even the electronic state of the matrix. The most important determinants of yield

are qualitatively summarized in Table A.3. Notice that although there is a distinction between the sputtering yield (amount of material removed per incident ion) and the secondary ion yield (which further involves ionization probabilities), factors that affect the sputter yield also affect the secondary ion yield and thus are included in Table A.3. In addition to those given in the table, the efficiencies of the ion collection optics, the transmission of the mass spectrometer, and the efficiency of the ion-counting detector will further influence the number of SI eventually detected. It should be clear from the table that *consistent* determination of effective yield is critical if one wishes to obtain accurate SIMS results.

Quantitation: Use of Standards and the Relative Sensitivity Factors

The problems of quantitation (or quantification), i.e., the process of going from the instrument-dependent raw ion counts to absolute concentrations, are compounded by the lack of a comprehensive model for the complex sputtering process capable of predicting SI yields. Coupled with the potential extreme variability in the SI yield during an actual experiment, the SIMS research community has resorted to the use of standards and relative sensitivity factors (RSF's) for quantitation. RSF is defined as the conversion factor from the secondary ion intensity to atom density for a given impurity residing in a specific matrix. It can be defined in the general relationship:

Table A.3 factors that can affect secondary ion yields when a primary ion beam is incident on a target.

Factors	Effect on Secondary Ion Yields (Y)
Primary Ion Energy and Current	• Y is proportional to both PI energy and current, although in a highly non-linear fashion. • Y can also depend on the angle of incidence depending on the crystallographic nature of the target. • Reactivity: Ionization probabilities are highly dependent on the reactivity of the PI with the target. For example, use of O^- or O_2^+ can lead to oxidation of the immediate vicinity of the impact area, leading to orders of magnitude increase in SI yield.
Physical State of the Target	• Crystallinity: The sputter yield (and thus Y) is sensitive to the crystallinity of the target. Large Y variation can result from sputtering of different exposed crystallographic planes. • Surface Roughness: Roughness that is comparable to the dimensions of a cascade collision event generally leads to higher yields, whereas porous structures can lead to re-trapping of the secondaries and lower Y. • Atomic Number: Periodic changes in the sputtering yield can be related to the surface binding energies of the elements [165]. • Preferential Sputtering: In multi-element alloys, the sputtering rate can vary for different constituent elements, leading to preferential faster sputtering.
Chemical or Electronic States of the Target	• Ionization potential: For positive ions, there is an inverse exponential dependence of ion yield on the ionization potential of the target [166]. Similar dependence of negative ion yield on electron affinity has also been found [167]. • Electronic States: surface chemical states of the target can also greatly influence ion yields. For example, the adsorption of a complete coverage of CO on a transition metal has been found to raise the positive ion yield by 1-2 orders of magnitude [168]. Oxidation of a metal surface (such as Si) has also been found to increase by factors of 10^2-10^4 with the presence of oxygen near the target surface [169].
Other Extraneous Effects	• Surface Charging: Charging of targets can deflect positive ions beyond the acceptance energy window of the mass analyzers. Negative secondary ions can be inhibited or totally suppressed for positive surface potential.

$$\rho_i = \frac{I_{SI}}{I_M} RSF \qquad \text{Equation A-1}$$

where ρ_i is the impurity atom density in cm^{-3}, I_{SI} is the impurity isotope secondary ion intensity in count/s, I_M is the matrix isotope secondary ion intensity in count/s, and RSF's are in the units of $atoms/cm^3$. RSF's are typically obtained either by calibration using an uniform sample of known impurity concentration, or calculated using implant standards with known dosage and peak implantation depth information. The latter is usually used because of the sophistication and accuracy in which one can predict the range and the straggle of a controlled impurity profile in a matrix by ion implantation. Fairly extensive databases of RSF's exist in the industry for popular impurities in common matrices and can be found in the literature (for example, see Appendix E of Reference 163). For new material combinations, an implant standard with the desired impurity is profiled with SIMS to obtain raw ion count profiles. Given the dosage ($counts/cm^2$) and the implant energy (and thus peak depth), the measured profile can be fitted with the implant parameters to obtain a proportionality factor which is the RSF. For systems using both a Faraday cup (for strong signals) and an electron multiplier (for weaker signals), the difference in their counting efficiencies must also be taken into account. Notice that, in principal, the RSF derived in this manner should have all instrumentation-specific parameters canceled out such that the results are universally applicable (assuming the implantation parameters are accurate).

An additional complication may arise when previously obtained RSF's are to be used. The relative isotope abundance has to be taken into account if the actual monitored species is different from the isotope used to derive the RSF's. In the case of elemental isotopes, only a constant scaling factor needs to be used. If the actual monitored species is a molecular ion (such as Se_3^+ or SeN^-), then an additional relative yield factor (usually based on the ratio of their

respective average ion counts in a uniform region during profiling) is required. As the process of molecular ion cluster production is even less understood, care must be taken to ensure that this relative yield factor does not vary significantly during the profiling of multi-layer structures.

Sample Charging

As previously mentioned, sample charging can cause changes in the SI emission as well as the collection efficiencies. There are two primary contributors to sample charging: (*i*) charging due to the impinging positively charged PI, and (*ii*) the induced emission of secondary electrons by the PI. Therefore, sample surface potentials tend to be positive in most cases. Secondary electron yield (number of secondary electrons per incident PI) is normally greater than one and can lead to a net positive surface charge state even in conducting samples. For non-conducting or moderately conducting samples, a thin (tens of nanometers) coating of Au is normally used to reduce the charging effects. Another method used to reduce charging problems includes the use of a source of low energy electrons (hundred of eV in energy). However, in systems where a high SI extraction voltage is present (as in magnetic sector mass analyzers), maintaining a stable supply of low-energy electrons may be difficult. A direct-current sample bias can also be used sometimes to successfully counter the buildup of sample surface potential. If all else fails, charging can usually be reduced by going to a smaller PI current, or by decreasing the rastered area.

Depth Resolution

In principal, the depth resolution of dynamic SIMS depends on a variety of parameters such as the sputtering rate, the range of the PI implantation, the extent of locally induced chemical change due to PI bombardment, the degree of recoil mixing of knock-in (where matrix atoms are pushed deeper into the sample by the incident PI), and the surface uniformity of the starting

target surface. In practice, the sputtering rate and the sputtered crater uniformity typically dominate the determination of depth resolution. A rough or inclined starting surface and spatial non-uniformity in the target as a function of depth result in a loss of depth resolution that can usually be detected by surface profilometry or electron/ion beam image examination. Uneven crater-edges can also lead to significant loss of depth resolution. In general, depth resolution is improved with decreasing PI current. Electronic gating techniques are often used to minimize the crater-edge effect. The ion detectors are "electronically blanked" to record SI intensity only when the ion probe is in a pre-defined center portion of the rastered area. Resolution and SI intensity can therefore be traded off to improve depth resolution.

Mass Interference

Since mass analyzers can only separate species having differing mass/charge ratio, combinations of ambient and surface impurities, mixed with the desired trace impurities, matrix elements, and the primary and secondary ion species can lead to similar values of mass/charge ratio and cause mass interference. One must carefully choose a proper species to monitor by anticipating the range of other probable mass/charge products (including isotopic combinations) that could be present. Magnetic sector and time-of-flight mass analyzers, because of their high mass resolutions, are well suited for applications that result in highly complex mass spectra.

Surface Effects

Several surface effects can sometimes lead to erroneous interpretation of a SIMS profile. The presence of oxides on the surface can significantly change the positive secondary ion yield. Contamination due to surface hydrocarbons and their subsequent recoil mixing into the sample can require a significant amount of careful pre-sputtering before reliable data can be obtained. Moreover, when highly volatile species are present in the chamber during slow sputtering, re-

adsorption and subsequent recoil mixing can occur and give rise to spurious signals. Clean handling of the samples (also during the conductive coating process) as well as a good understanding of the surface conditions of the samples to be analyzed, are therefore very important when accurate surface analysis is required.

A.3. SIMS Analysis of ZnSe: Practical Considerations

SIMS analyses of GSMBE- and MBE-grown ZnSe doped with Cl and N have been primarily performed at Charles Evans and Associates (CE&A) in Redwood City, CA. Analysis sessions have been largely interactive; a member of our laboratory has been physically present during several analysis sessions. SIMS service has also been obtained from Evans East (EE), albeit with minimal intervention or input from us. The following sections will discuss the particular problems encountered, specific quantitation procedures, and the necessary precautions recommended for future SIMS of ZnSe. Profiling of hydrogen and nitrogen will be emphasized as hydrogen passivation of nitrogen acceptors has been (and remains) the focal point of our preoccupation in II-VI GSMBE research.

Instrumentation

The bulk of our ZnSe SIMS data has been obtained using an IMS Cameca 4f ion microscope equipped with magnetic sector mass spectrometer at CE&A. Typical experimental conditions for both analyses at CE&A and EE are compared in Table A.4. Samples were normally Au-coated using RF-plasma sputtering at the respective SIMS facilities prior to loading into the SIMS system. At CE&A, up to nine samples can be loaded at one time; samples are loaded into a sample holder with square apertures in a metallic mask. One should keep in mind that due to the sensitive dependence of the background impurity levels on pumping conditions and sample

cleanliness, samples to be compared should be loaded simultaneously in the same sample holder and remain evacuated as long as possible before the analysis.

Various combinations of negative and molecular ion complexes involving the PI have been used to monitor the desired trace elements based on predictions of possible mass interference.

Table A.4 Typical SIMS Experimental Conditions for SIMS analysis at Charles Evans & Associates and Evans East.

Charles Evans & Associates	
Instrument	• Cameca 4f
Mass Spectrometer Type	• Magnetic Sector
Primary Ions	• Cs^+, nominal current: 30~100 nA • nominal beam energy: 14.5 keV
Secondary Ions	• Negative Secondary Ion Spectrometry
Analysis Area	• Raster region: 200-250μm square • Gating reduces acceptance of secondaries from a 30 μm diameter centered in the rastered region.
Typical Detection Levels for Commonly Used Elements	Nitrogen: low 10^{17} cm^{-3} Hydrogen: low 10^{18} cm^{-3}, best case to mid 10^{17} cm^{-3} Chlorine: low 10^{15} cm^{-3}
Nominal Quoted Resolutions	Lateral: 0.5 μm Depth: 0.5 - 30 nm

Evans East	
Instrument	• Perkin-Elmer 6300
Mass Spectrometer Type	• Quadrupole
Primary Ions	• Cs^+, nominal current: ~200 nA • nominal beam energy: 5 keV
Secondary Ions	• Negative Secondary Ion Spectrometry
Analysis Area	• Raster region: 300 μm square • Gating reduces acceptance of secondaries from a 90x90 μm area centered in the rastered region.
Typical Detection Levels for Commonly Used Elements	• not specified, but believed similar to CE&A.

For the selenium matrix signal, $^{80}Se^-$ (80 a.m.u. isotope of Se), $^{80}Se_3^-$, $^{82}Se^-$ (82 a.m.u. isotope of Se), and $^{82}Se_3^-$ have been used; H^- and Cl^- were used for the determination of hydrogen and chlorine concentrations, respectively. Other common impurities such as carbon and oxygen have also been monitored (using published RSF's), but were found to be near or below their respective detection limits in the bulk regions of ZnSe. Concurrent monitoring of the As^- matrix signal was used to delineate the ZnSe/GaAs interface for termination of depth profiling. Total time required to profile through 2-3 μm samples ranges from 2-20 minutes depending on the depth resolutions required and the extent of charging.

Data Quantitation

Data quantitation was performed using deuterium and nitrogen implanted in ZnSe epilayers grown on GaAs. The implantation parameters (performed by IICO Inc.) are as follows: deuterium dosage of $2x10^{15}$ cm^{-2} and implantation peak at 0.807 μm, nitrogen dosage of $1x10^{15}$ cm^{-2} and implantation peak of 0.456 μm. Figure A.2 shows typical SIMS profiles of nitrogen- and deuterium-implanted ZnSe standards. By matching the measured depth and the concentration profile with those expected from known implantation conditions, RSF's can then be calculated. When the selenium species used during profiling of the implant standard is the same as the species monitored during the actual analysis, the equation for quantitation (using point-to-point normalization) is simply:

$$\frac{C}{M} \cdot RSF = Concentration \qquad \text{Equation A-2}$$

where C is the impurity ion count in count/s, M is the selenium matrix count in count/s, and "*Concentration*" is the quantified atomic concentration in atoms/cm^3. If the selenium species

monitored during the actual analysis is different from the one used to derive the RSF, additional factors will need to be included:

$$\left(\frac{C}{M}\right)\cdot\left(S_{EM/FC}\right)\cdot\left(R_M\right)\cdot RSF = Concentration \qquad \text{Equation A-3}$$

where the factor $S_{EM/FC}$ is a small relative sensitivity factor for SI detection (1.024 for the Cameca 4f) and R_M is a factor accounting for either the relative isotope abundance (when different isotopes of selenium have been used) or the ratio of the average ion count of the actual monitored selenium molecular ions (such as $^{82}Se_3^-$) to the average ion count of the selenium species used in RSF determination. For example, if $^{80}Se^-$ was used for RSF determination and $^{82}Se^-$ was used during actual impurity analysis, then R_M would be 0.092/0.497 or 0.185, the ratio

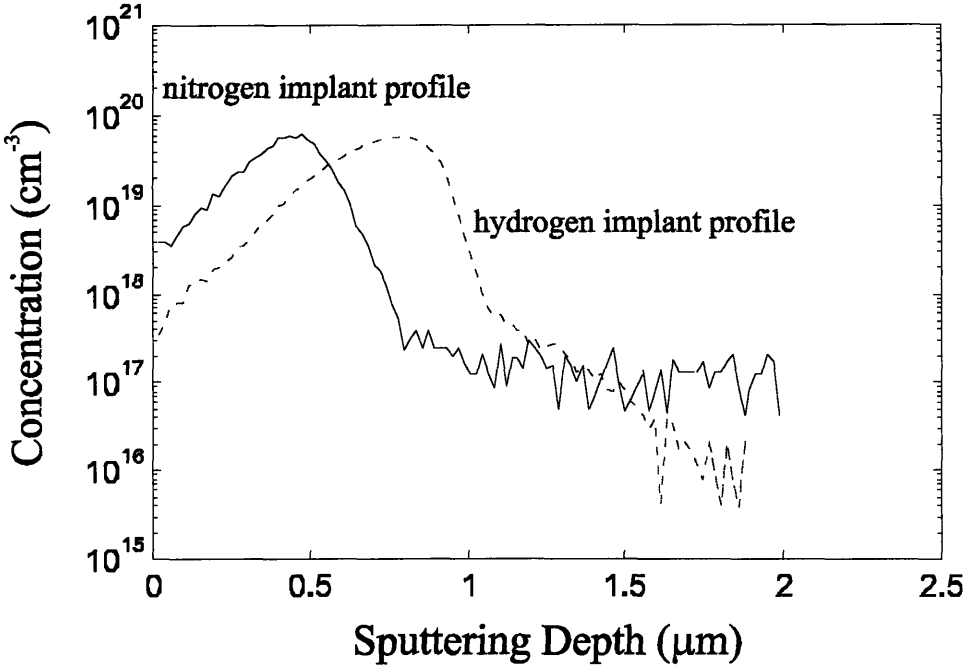

Figure A.2 SIMS profile of deuterium and nitrogen implants in ZnSe epilayer for quantitation of impurity ion counts. The use of deuterium provides a lower background signal while the SI yield is expected to be similar to that of hydrogen.

of the relative abundance of ^{82}Se to ^{80}Se. If $^{82}Se_3^-$ was used instead during the actual impurity analysis and $^{80}Se^-$ during RSF determination, then R_M would be the ratio of the average SI count of $^{82}Se_3^-$ over the average SI count of $^{80}Se^-$ also taken during the impurity analysis. The ratio $S_{EM/FC}$ is necessary because often times the main selenium isotope, $^{80}Se^-$, is used during RSF determination for maximum signal/noise ratio. Because of the matrix signal strength, Faraday cup is normally used to collect the $^{80}Se^-$ SI signals. During impurity analysis, however, the more sensitive electron multiplier is normally used; switching between the two detectors on the Cameca 4f, for example, introduces transient noise in the measurement and should be avoided.

Note that it is important to perform the implant calibration for each set of experiments to minimize the influence of environmental, procedural and instrumentational biases. In addition to the use of implanted standards, it is often prudent to include a reference sample that has been previously analyzed for the desired impurity concentrations. This allows verification of the quantified data as well as comparison of the background impurity levels. The RSF's derived from the implant standards for nitrogen and hydrogen have been shown to vary individually by at most a factor of approximately three to four. The maximum variation in the ratio of the hydrogen and nitrogen RSF's has always been less than two, suggesting the possibility that some systematic bias may exist in the procedures used to determine the RSF's. The reduced variation in the ratio of the RSF's is important in our studies of ZnSe:N with hydrogen passivation because of the emphasis placed on the ratio of the hydrogen concentration relative to the nitrogen concentration.

As previously discussed, charging and other effects can cause unpredictable changes in the secondary ion yields. Variations in the matrix signal (in this case, various forms of Se) are usually indicative of charging or other instrumentation-related changes in the SI collection

efficiency; any single crystalline and reasonably stoichiometric ZnSe is expected to have a constant matrix signal. In nearly all of the quantitations performed, the desired impurity ion counts (such as $^{1}H^{-}$ and $^{94}SeN^{-}$) are usually normalized (point-to-point ratio) by the selenium matrix ion counts to reduce these extraneous effects.

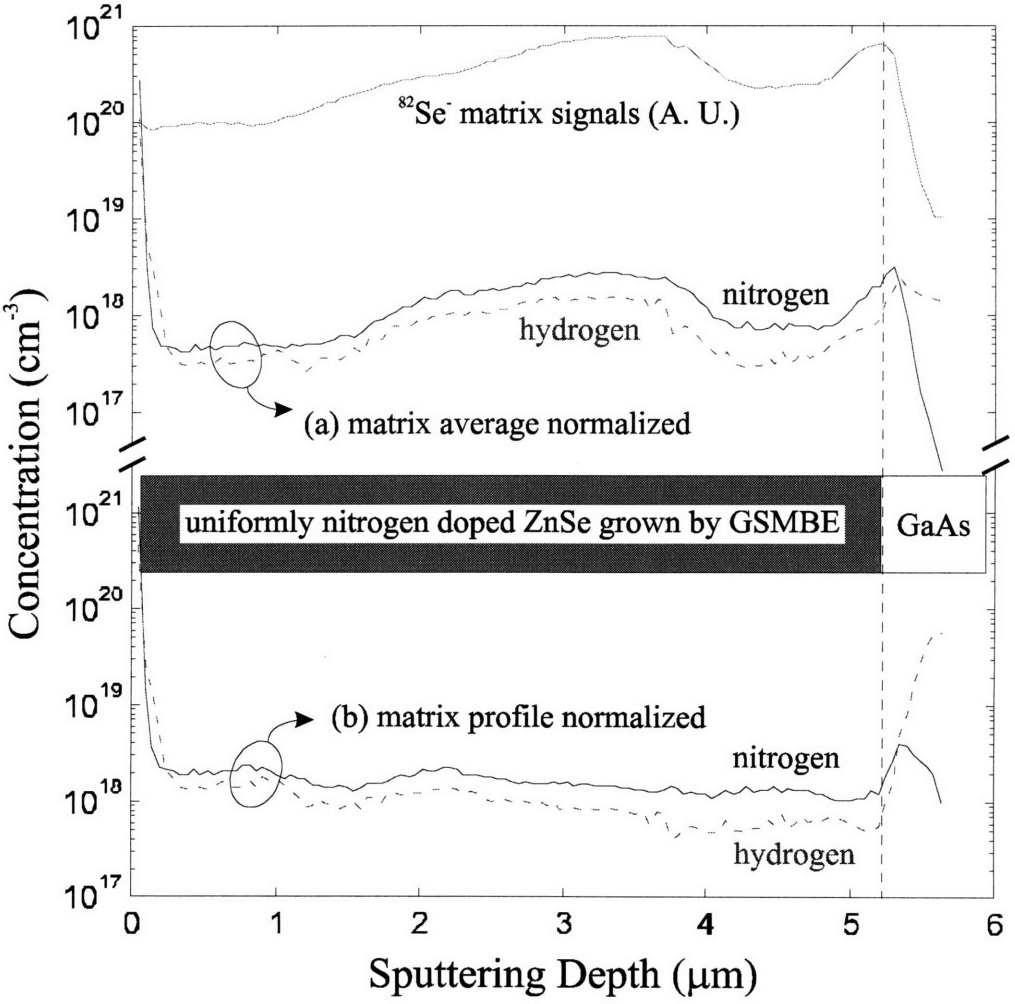

Figure A.3 SIMS profile of uniformly nitrogen-doped ZnSe grown on GaAs illustrating the effect of (a) single point normalization of the impurity profile using average matrix signal counts, and (b) point-by-point normalization of the same raw data using the entire matrix profile. The apparent structure in (a) was removed by proper data normalization to cancel out the effect of charging and other instrument related changes in the SI collection efficiency. Note, however, that other normalization-related artifacts can be introduced (such as the rising hydrogen signal in the GaAs layer) and should be interpreted carefully.

As a demonstration of the necessity of this normalization procedure, Figure A.3 shows two quantified depth profiles that are (a) normalized by an average selenium matrix count, and (b) point-to-point normalized by the selenium matrix signal. Since the particular sample used was uniformly-doped, the physical phenomenon that caused the changes in the matrix as well as the impurity signals introduced false structures in the SIMS profile which can be removed by proper data normalization. Note that because of the presence of the Se matrix signal term in the denominator in the normalization process, an artificial increase in the impurity signal should be expected after the sputtering has penetrated into the GaAs region.

Due to the logarithmic nature of the ion count, a small impurity signal that is only slightly above the background level can be highlighted by performing a background level subtraction after quantitation. This can be especially useful when analysis of elements that are also residual contaminants in the SIMS vacuum system is desired. The proper choice of the background level becomes critical and should be based both on the observed background levels in each as well as previous experiments, and any a-priori information about the expected behavior of the impurities. Figure A.4 compares two processed plots (a) without and (b) with background subtraction for hydrogen (background subtraction was not performed on the nitrogen concentration). The effectiveness of the subtraction process is clearly demonstrated in this case. Note that because of the subtraction process, the "apparent background level" in the undoped regions is now meaningless. Furthermore, in comparing impurity concentrations at different locations in the same profile, one must also keep in mind that any slight difference in ion counts across the profile are now greatly enhanced and depend on the choice of the impurity background level.

Reducing Charging Effects

As discussed, sample charging can cause measurement inaccuracies, especially for highly resistive samples. Charging during the analysis of hydrogen-passivated ZnSe samples is particularly problematic because they are usually highly resistive. Furthermore, because of its low mass/charge ratio, hydrogen can be easily deflected from the acceptance window of the SI

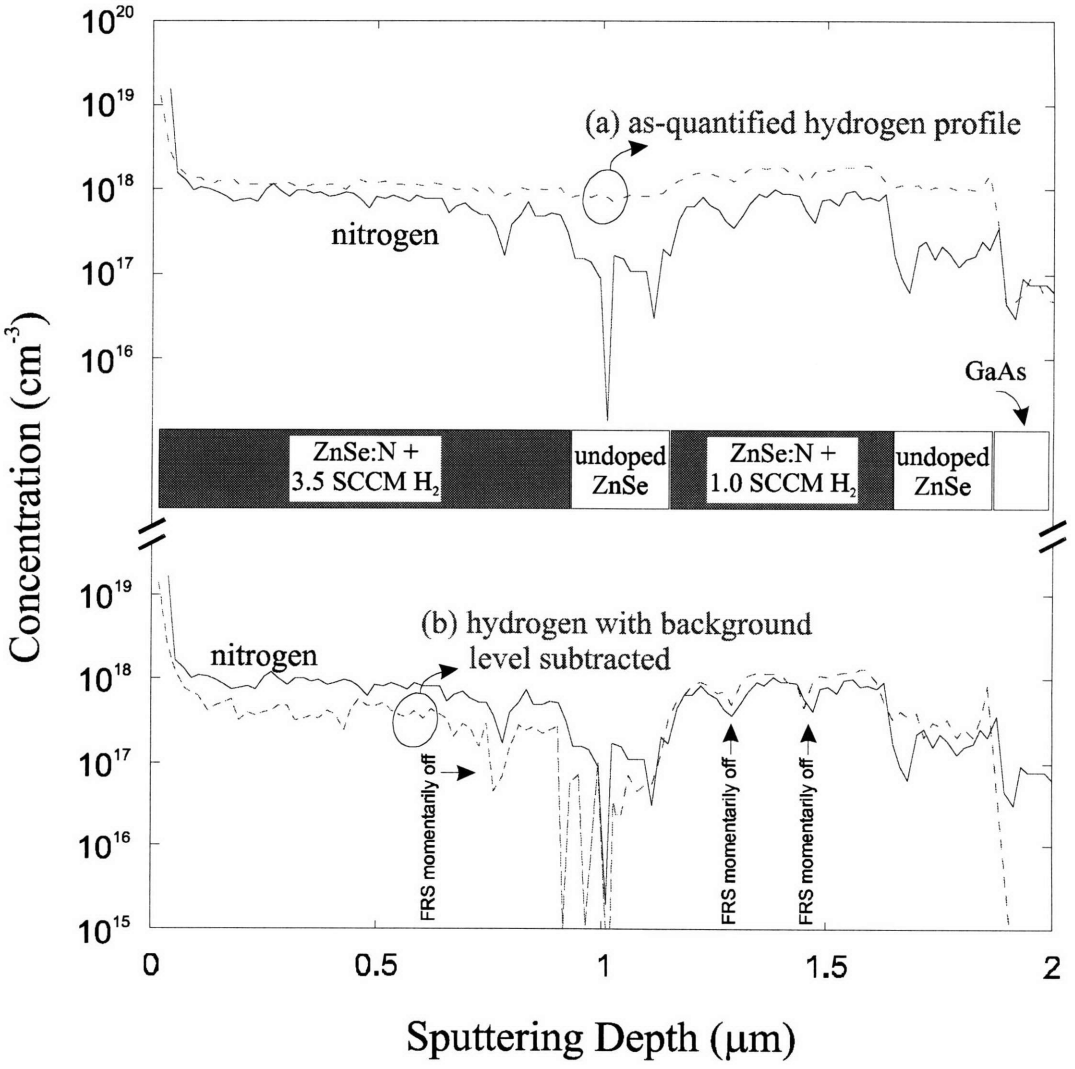

Figure A.4 SIMS profiles showing the effect of background subtraction on the hydrogen concentration: (a) as quantified [H], and (b) [H] after the instrument ambient background of $1x10^{18}$ cm^{-3} have been subtracted. The subtracted hydrogen profile is seen to behave as expected based on numerous past experiences.

collection optics due to the surface potential. Several procedures have been carried out to minimize the effect of charging:

(1) Within limits, normalization using the matrix signal (assuming that, to the first order, charging affects the matrix and impurity signals similarly) can reduce the effect of charging induced signal variations.

(2) Conductive Au-coating was sputtered on all samples prior to analysis.

(3) When possible, ZnSe samples were grown on conducting GaAs substrates to improve charge drainage.

(4) Primary ion beam current has, at times, been reduced to mitigate the effect of charging.

(5) Low energy electron beam flooding and automatic voltage compensation have been applied in all analyses, although with varying degrees of success.

Improving Background Impurity Levels

Distinguishing a measured SI signal from the background level is particularly important for impurities that are also present in the normal vacuum environment. Depending on the type of pumps employed in the SIMS apparatus and the nature of the sample stage, atmospheric components such as oxygen, nitrogen and hydrogen residuals may be ionized near the sample and give rise to an undesirable ion signal. This effect has been particularly troublesome with hydrogen, which is normally not effectively evacuated by UHV pumps such as the ion and cryogenic pumps typically employed in SIMS apparatuses. Whenever possible, the samples should be loaded into the chamber as early as possible. The background impurity level has been found to decrease if the samples are loaded into the Cameca 4f load-lock chamber and evacuated

for several days. Clean handling of the samples to reduce surface hydrocarbons can also be important.

A reference level for the impurity of interest should be designed into the layer structure for SIMS analysis whenever feasible. For example, in analyzing hydrogen passivation of nitrogen acceptors, an initial undoped layer (near the GaAs heterointerface) of sufficient thickness (>0.2 μm) can be used as an indicator of the background impurity levels. As long as the matrix signal remains flat and other signs of charging are absent, these reference levels can be taken as the detection levels for each profiling.

Another technique to distinguish whether the measured signal is indeed due to the impurities in the sample or arises due to the background level is to change the rastered area during profiling. If the ion signal of interest is increased as the raster area is increased, then the measured ion signal most likely** originates from the sample. Increasing the rastered area should cause more of the impurity ions to be bombarded from the surface relative to the constant background level that is present.

** It is, however, still possible that significant adsorption of the background impurity on the sample surface may also cause an increase in the ion signal as the rastered size in increased. Although the magnitude of the increase should be small as well as transient in nature.

Appendix B C-V Measurements

B.1. Backgrounds and Key Equations

Capacitance-voltage measurement (C-V) is a widely used and accepted method for measurement of dopant profiles in semiconductor. Its popularity arises from several key advantages:

(1) The ease in which test structures can be built and measurement made. The process is also largely non-destructive; in some cases (such as the use of mercury contacts on GaAs) the measurement can be made without permanently altering the surface conditions of the semiconductor.

(2) The ability to unambiguously determine the sign of the carriers responsible for conduction.

(3) Coupled with electro-chemical etching, detailed depth profile of dopants can be obtained.

For semiconductors with large energy bandgaps and electron affinities, it is often difficult to find metallic elements with sufficiently large work functions to form ohmic contacts that would enable Hall effect measurements. This is particularly true of p-type ZnSe, where all metals are known to form Schottky barriers. Consequently, for p-type ZnSe, C-V measurements remains the de-facto measurement method to demonstrate the achievement of p-type conductivity.

The basic concepts utilized in making C-V measurements using the Schottky diode geometry are relatively straight forward. A Schottky metal is deposited onto the semiconductor in question. The Schottky barrier formed generates a depletion region directly underneath the

Schottky metal and establishes a zero-bias depletion capacitance C_o, the value of which depends on the diode geometry, material properties, and the amount of space-charge per unit volume. By modulating the voltage of the Schottky metal relative to another collection terminal (which could be either an ohmic or a Schottky contact), the depletion region grows and shrinks depending on the quantity of space charge that is exposed in order to maintain overall electrical neutrality. Since the amount of space charge per unit volume can be related to the ionized donors (N_D^+) or acceptors (N_A^-) (assuming traps are negligible), the doping concentration as a function of depth probed by the edge of the depletion region can be obtained.

The key operating equations are as follows:

$$N(x) = \frac{-2}{q\varepsilon_o\varepsilon_r A^2}\left[\frac{d(\frac{1}{C^2})}{dV_A}\right]^{-1} \qquad \text{Equation B-1}$$

$$x_d = \frac{A\varepsilon_o\varepsilon_r}{C} \qquad \text{Equation B-2}$$

where N is the net doping concentration, q is the charge of the electron, ε_o is the free space dielectric permittivity, ε_r is the relative permittivity of the material, A is the area of the Schottky depletion region, V_A is the applied voltage, C is the measured capacitance, and x_d is the width of the depletion region (which is also the depth around which N is incrementally measured). For ZnSe, the numerical constants used are: q=1.6x10^{19} C, ε_o=8.854x10^{-12} F/m, and ε_r=9.1. Additionally, the Schottky barrier height ϕ_B can be calculated (assuming the calculated N's are reliable):

$$x_d = \sqrt{\frac{2(\phi_B - V_A)\varepsilon_o \varepsilon_r}{qN}} \qquad \text{Equation B-3}$$

Typical Schottky barrier heights using Cr/Au contacts are approximately 1 eV, in agreement with the various reported values for moderately-doped ZnSe:N.

B.2. Device Geometry Considerations

Because of the difficulty in obtaining ohmic contact to p-type ZnSe, C-V device geometry where both electrical contacts are made to ZnSe is commonly referred to as the double-Schottky or the lateral configuration. If doped GaAs is used as the substrate, vertical or through-wafer measurements can be performed by making an ohmic contact to the back side of the GaAs substrate. A schematic diagram of the two device geometries are shown in Figure B.1. The figure is drawn for the case of p-type ZnSe grown on GaAs. The lateral double-Schottky configuration must be used when semi-insulating substrates are used, as no vertical conduction is possible; the vertical through-wafer measurement must be adopted when conducting substrates are used in order to prevent carrier contributions from the substrate.

Let us first consider the double-Schottky configuration. From the point of view of the two contact terminals, this configuration is equivalent to two capacitors connected back-to-back in series. The capacitance due to the center Schottky dot, C_D, is usually designed to be much smaller than the capacitance of the outer diode, C_R (sometimes in the shape of a ring surrounding the dot). The two-terminal capacitance measured C is thus $C_D \cdot C_R/(C_D + C_R) \sim C_D$ when $C_R \gg C_D$. It may be necessary to take into account the sheet resistance between the center and outer electrodes [170], especially when the sample is lightly-doped or if surface effects are present. Typical measurement frequencies range from 100KHz to 1 MHz. The double-Schottky

configuration has the advantage that the results are easy to interpret without having to consider the heterojunction depletion capacitance between the ZnSe and the GaAs.

The vertical, or through-wafer, device geometry as shown in Figure B.1 is easier to fabricate than the lateral configuration, where a metal lift-off step of the annular gap is required after the metal deposition. Vertical devices typically only require a one-step metal evaporation onto ZnSe, as the In that is normally used in wafer mounting forms the ohmic contact to GaAs. Viewed from the terminals, the vertical configuration appears as two capacitors C_{HJ} and C_D (with their

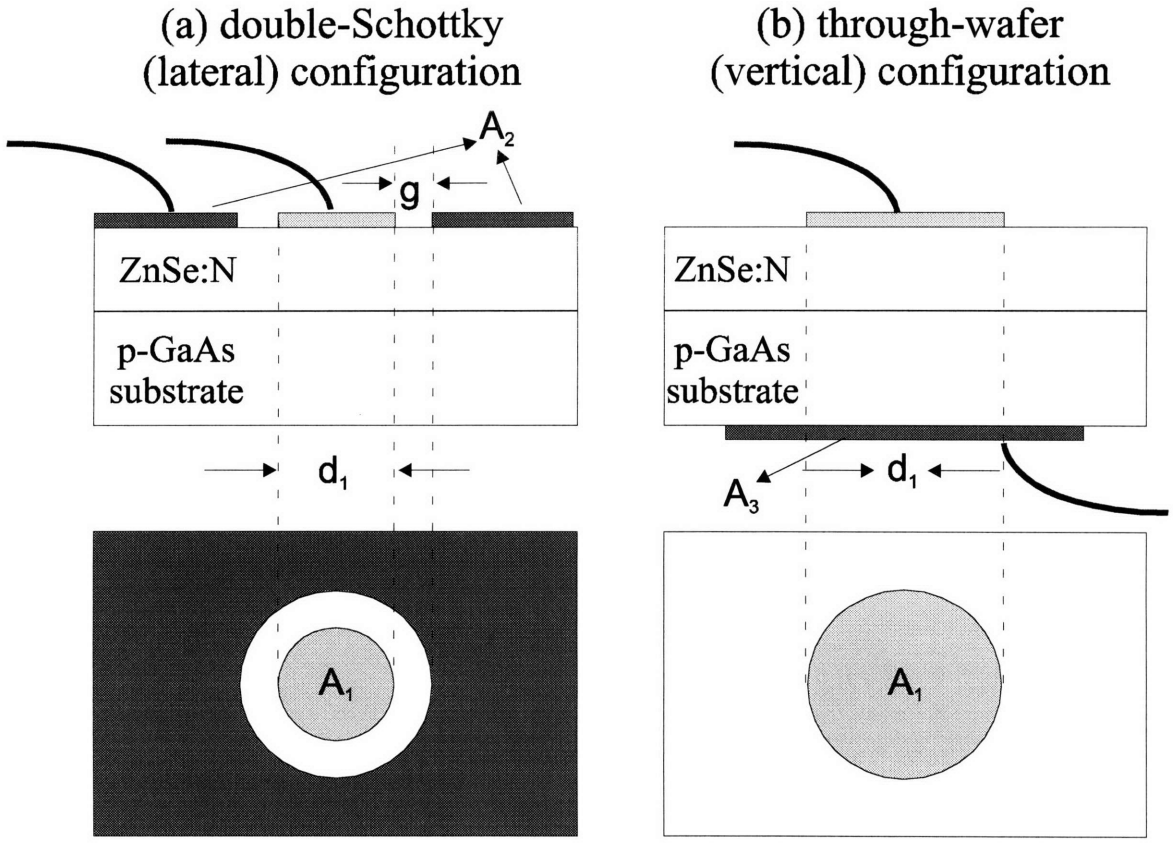

Figure B. 1 Schottky diode geometries for C-V measurement using the (a) double-Schottky lateral configuration, and (b) the vertical through-wafer configuration. g is the width of the annular gap, A_1 (diameter d_1) is the area of the circular "dot" anode, A_2 is the total area of the "ring" cathode in the lateral configuration, and A_3 is the area of the ohmic contact to GaAs substrate in the vertical configuration.

associated impedances) back-to-back connected in series. Analysis of the measured capacitance is more complication in this configuration because of the heterojunction depletion capacitance (C_{HJ}), which is frequency-dependent through the frequency dependence of current spreading. At low frequencies the current spreading is considerable, resulting in C_{HJ} much greater than C_D. Thus the measured capacitance at low frequencies reflects the Schottky diode capacitance C_D. At sufficiently high frequencies, the current spreading is minimal and $C_{HJ} \cong C_D$. It is important to emphasize that under this condition, some underestimation of the net doping concentration is to be expected (which is, in the worst case, at most 50% when $C_{HJ} = C_D$). Therefore, sufficiently low frequency should be used (below a frequency above which the C-V profile showed significant change) to ensure an accurate measurement.

B.3. Experimental Conditions

Cr/Au has been found to yield satisfactory Schottky barriers for C-V measurements of both ZnSe:N and ZnSe:Cl. The ~ 100 Å of Cr metal was mainly intended to improve the adhesion of Au on ZnSe. Prior to metal evaporation, the ZnSe surface was treated with a buffered HF solution for 5-10 seconds to remove the native oxides. For lateral devices, a photo-lithographic process using positive resists (Shipley-1813) has been used for subsequent lift-off of the ring-gap with acetone in an ultra-sonic bath. Devices with center electrode diameters (d_1) of 200 and 400 μm and ring-gaps (g) of 20 and 25 μm have been used. The center diode is normally taken to be the positive terminal. For the vertical configuration, either a shadow-masking or a photo-lithographically-defined dot of ~ 500 μm in diameter has been used. Indium or silver paint were used to mount the processed chips onto tantalum strips for measurement. The positive terminal is again usually the top electrode. The actual capacitance measurement is usually performed in

Professor Del Alamo's laboratory at MIT using a HP4194A impedance analyzer connected to a probe station. Experiments were performed under normal room-light conditions with long integration times to ensure a clean signal. Typical frequencies that have been used for determination of the net doping concentrations ranged from 10 kHz to 1 MHz. The raw C-V profile was then recorded and transferred to an IBM-compatible PC for differentiation.

In order to cross-check the accuracy and consistency of the C-V results, MBE-grown ZnSe:N samples with known values of $[N_A\text{-}N_D]$ have been obtained from Purdue University and processed according to the processes described above. The results were found to be in agreement with those obtained by Purdue University. A reference sample of nitrogen-doped ZnSe grown by MBE is normally included in each measurement session to ensure run-to-run consistency. For example, three separate measurements of the same sample over a 6-month period have produced $[N_A\text{-}N_D]$ of $2\text{x}10^{17}$ cm^{-3}, $2.2\text{x}10^{17}$ cm^{-3}, and $2.0\text{x}10^{17}$ cm^{-3} in three consecutive measurements.

Appendix C Cathodoluminescence

C.1. Background

A modern electron microscope system can provide a wealth of information about the material being examined by utilizing the myriad of interaction by-products between the material and a focused electron probe. Besides the usual secondary electron imaging (SEI) and transmission imaging (TEM) modes, many alternative configurations can be used to provide useful contrast between regions with different physical properties within a sample. In the scanning electron microanalysis, many imaging techniques are available: these include: back-scattered electron imaging (BEI), electron channeling patterns (ECP), electron probe microanalysis (EPMA), Auger electron spectroscopy (AES), electron beam-induced current (EBIC), and cathodoluminescence (CL). Cathodoluminescence, as the name suggests, makes use of the "luminescence" that results from the interaction of the material under investigation and the "cathode-rays" (i.e., beam of electrons). By injecting an energetic beam of electrons (typical energies of several to 50 keV), a large number of electron-hole pairs can be generated within the interaction volume and may subsequently radiatively recombine across the intrinsic energy bandgap or via impurity or trap states. Similar in many ways to photoluminescence measurements except in the details of the excitation of the electron-hole pairs, CL's sensitivity to the presence of optically active impurities can, in best cases, be as low as 10^{12} cm^{-3}.

CL is particularly well suited for routine analysis of optoelectronic materials for the following reasons:

(1) Optoelectronic materials are generally required to have good fluorescent efficiency to begin with, making them suitable for CL (as well as PL) observations.

(2) It is possible to obtain depth resolved information by varying the electron beam energy (and thus the range of electron beam penetration).

(3) Fairly good lateral resolution (on the order of 1 μm) is possible when CL information is collected in the scanning mode.

(4) Except in high-injection conditions, CL is largely a non-destructive, non-invasive characterization method.

(5) Other complementary modes of electron-probe analysis (such as SEM, EBIC or EPMA) can be readily utilized to obtain a more multi-faceted picture of the material in question.

The major limitation of CL characterization lies in the difficulty of obtaining quantitative information. Unlike PL excitation, where the energies of the incident photon can be resonantly tuned to the energy levels of the transitions in question, CL excitation generally leads to emission from all the emission mechanisms present in the material; tuning of the electron energy can only affect the detailed shape of the excitation volume. The lack of a universally applicable quantitative theory of CL spectral identification, the difficulty in obtaining standards and the large number of experimental and material conditions that can affect the outcome of the CL measurement[††] are the major challenges still facing the widespread adaptation of CL. But the ease in which CL can be performed using an SEM equipment and the rapid manner in which useful qualitative information can be obtained are sufficiently compelling reasons for its use.

[††] Experimental factors such as sample charging, luminescence collection efficiency, sample preparation and surface contamination all play a role in determining the amount of luminescence observed.

CL examination of II-VI on III-V heteroepitaxy has proven to be a valuable method to obtain information on the structural quality of the heterointerface. As have been shown in the previous chapters, luminescence contrast in the CL mode can be correlated to the defect densities determined by other means. Defect contrast can also be used to quickly deduce the effects that nucleation and interface conditions have on the structural qualities of the epilayer. In fact, the ability to perform *in-situ* CL characterization during the growth process would be invaluable in the effort to improve the quality of the II-VI/III-V interface.

C.2. General Principles of Cathodoluminescence

In order to practically utilize CL as an effective characterization tool, several key concepts are briefly discussed here. For more detailed expositions on CL as well as electron-matter interactions in general, readers are referred to the many review works found in the literature [for example, see 171,172].

The interaction of solid state materials with a beam of energetic electrons is highly complex, resulting in the production of numerous particles which can be selectively collected to yield useful information on the material. These particles include the emission of secondary electrons, back-scattered electrons, Auger electrons, continuous and characteristic X-rays, as well as photons in the visible and infrared range. The sequence of events that occurs in electron-matter interaction can be briefly summarized as follows: first, the energetic electrons enter the solid at an angle determined by the parameters of the electron gun optics. The trajectories of the electrons deviate quickly due to elastic scattering with the host atoms. A portion of the incident electrons eventually undergo enough randomizing collisions that they reemerge from the material as back-scattered electrons. The effective beam diameter is now rapidly broadened, typically

from tens of nanometers to micrometers. As the electron rapidly lose energy at a rate of tens of eV/nm via inelastic processes, these energy transfers to the outer and inner shell electrons and atomic cores result in the emission of secondary electrons and x-ray emissions, as well as optical luminescence. The electron-hole pairs that are generated continue to diffuse and further broaden the interaction volume. A fraction of them may eventually recombine radiatively, giving rise to a CL signal. Additionally, the injected electrons may interact with collective phenomenon such as plasmons (collective motion of free carriers) and phonons (non-radiative recombination). For CL imaging, several inter-related parameters are of key importance in understanding the results: lateral resolution, electron penetration range, and electron-hole pair generation rate. Although the electron probe diameter can be as small as tens of nanometers at low probe currents, the lateral resolution of CL imaging is, to the first order, limited by the electron-hole generation volume as the electron is elastically and inelastically scattered in the material. This limits the lateral resolution in scanning CL imaging to about 1 μm in typical III-V and II-VI semiconductors. The resolution is further limited (or deteriorated) by the minority carrier diffusion length, which effectively broadens the luminescent volume beyond the initial electron-hole pair generation volume by diffusion.

The depth to which the electrons are able to penetrate into the material is related to the energy of the electron beam. Higher keV electrons probe deeper into the materials surface; the lateral resolution suffers, however, because the electrons can now "scatter farther" from the point of entry. Figure C.1 shows an illustration of the shape of the electron interaction volume as a function of incident voltage and atomic number. Higher atomic number and electron energies tend to produce broader lateral profiles and deeper electron penetration ranges, respectively.

The most versatile method of estimating the size and shape of the interaction volume is by the Monte Carlo simulation. This is especially useful when the interaction volume is large and multiple scattering events are present, making analytical solutions impractical. To help visualize the shape and extent of typical interaction volumes, Figure C.2 shows the calculated electron trajectories for 30 keV electrons for Al (Z=13), Cu (Z=29), and Au (Z=65) at both normal and 45° incidence [174]. For large atomic number materials, such as Au, the interaction volume is seen to become more hemispherical and less sensitive to changes in the incident angle. Notice that the average atomic number Z_{ave} of 32 for ZnSe is similar to the case of Cu (a.m.u.=29).

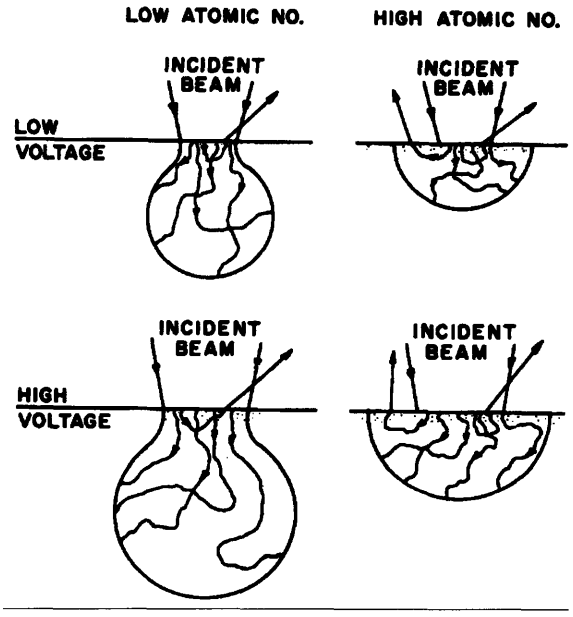

Figure C.1 Schematic of the electron interaction volume illustrating the effect of atomic number and electron beam voltage. Figure adapted from [173]

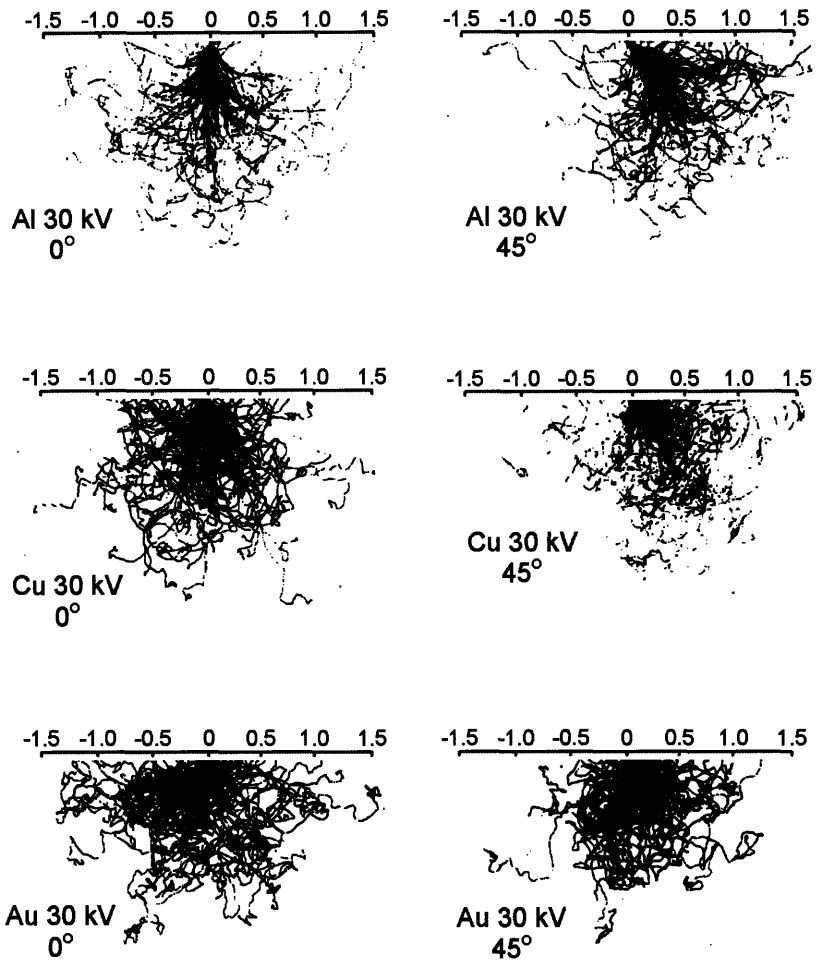

Figure C.2 Calculated electron trajectories for a 30kV beam in Al, Cu, and Au for both 0° (normal) and 45° incidences as indicated. Note that the horizontal axis is given in units of $\rho \cdot x$ (mg/cm^2). Figure adapted from [174]

For convenience, several empirical equations have been developed to estimate the electron penetration range (*R*). Using energy-loss considerations, Kanaya and Okayama [175] have developed a general expression that takes into account both elastic and inelastic collisions which agrees well with experimental results over a wide range of atomic numbers:

$$R = \frac{0.0276 \cdot A}{\rho \cdot Z^{0.889}} E^{1.67} \qquad \text{Equation C-1}$$

where R is the range of the electron penetration (where the electron excess energy becomes zero), A is the atomic weight in g/mole, Z is the atomic number, ρ is the density in g/cm^3, and E is the energy of the incident electrons in keV. Figure C.3 shows the calculated R as a function of the incident electron beam energy for ZnSe using ρ=5.26 g/cm^3 and numerical averages for A and Z. The electron-hole pair generation factor is, to the first order, proportional to E/e_i, where e_i is the ionization energy for the material.

Determination of the true interaction volume where cathodoluminescence occurs is further complicated by the need take into account the minority carrier diffusion lengths. For ZnSe, it has been found that in typical Bridgman-grown bulk ZnSe, the minority carrier diffusion length is ~

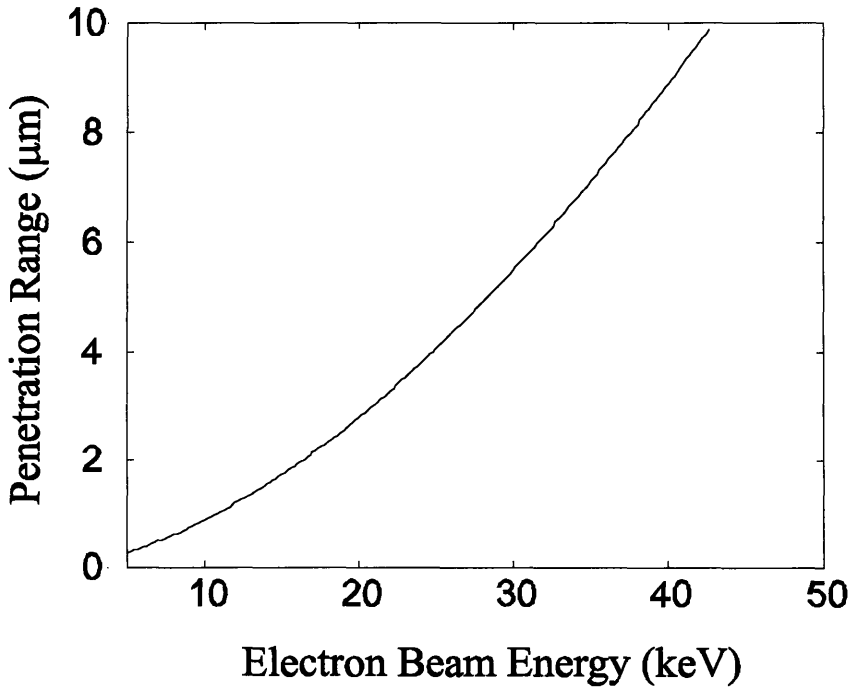

Figure C.3 Calculated electron range as a function of the electron beam energy using equation derived by Kanaya et. al. [175].

0.4 μm [142,176]. The interaction volume for the generation of CL is thus modified by the additional broadening due to carrier diffusion.

C.3. The JEOL JSM 6400 SEM at MIT

All of the CL experiments were performed on a JEOL JSM 6400 SEM with a CL attachment at Professor Kimerling's laboratory at MIT. Some pertinent specifications of the SEM apparatus are shown in Table C.1. A liquid helium cooled sample stage is available for low temperature (to ~ 4K) measurements.

Un-coated samples were normally mounted with silver conductive paint on cylindrical sample holders with an available mounting area of ~ 0.75" in diameter. Typical operating vacuum (with the acceleration voltage on) is in the low 10^{-6} Torr range. A fixed-focal point parabolloidal mirror having a small circular opening for the primary electrons is used to collect the luminescence. The collected light then passes through a monochromator with gratings blazed for the visible region of the spectrum. The output of the monochromator is then coupled to a photomultiplier tube and amplified with either a lock-in amplifier (for spectral measurements) or a current pre-amplifier (for direction image observation). Spectral measurements were taken with an MS-DOS microcomputer equipped with a data acquisition card. CL images were obtained by passing the output of the detector through a current preamplifier and displayed on a CRT. Images were stored either by capturing the CRT image on photographic film or transferred to a SUN workstation for subsequent image processing and retrieval.

Table C.1 Relevant Specifications of the MIT JSM-6400 SEM/CL facility

SEM Section	
Electron Filament Type	hairpin Tungsten filament
Accelerating Voltage	0.2-40 kV
Magnification	10-30,000 X
Secondary Electron Image Resolution (35 kV)	3.5 nm at 8mm working distance 10 nm at 39 mm working distance
Probe Current Range	10^{-5} to 10^{-12} Amps
Specimen movement range	X: 50 mm, Y: 70 mm, Z: 40 mm tilt: -5° to 90°, rotation: 360°
Secondary Electron Accelerating Voltage	10 kV
Secondary Electron Detector	scintillator/photomultiplier
Cathodoluminescence Section	
Photon Collection	retractable parabolloidal mirror; can collect up to 80% of all emitted light
Monochromator	Oxford Applied Research 0.3 m grating spectrometer; resolution=0.5 nm
Detector	thermal-electrically cooled photomultiplier; usable spectral response: 300~900 nm
Signal Processing	lock-in amplifier for spectral measurements, current pre-amp for direct image observations.

Some words of caution are in order regarding the interpretation of the images obtained using the setup described above. Since there are a large number of experimental/equipment settings that affect the apparent contrast in a CL image, it is necessary to ensure that some repeatable procedure be followed in order to compare one image to another. Time fluctuations in the probe current, the detector/photomultiplier acceleration voltage and temperature settings, the current pre-amplifier gain setting, the entrance and exit slits of the monochromator, and the analog-to-digital capturing process with independent brightness and contrast controls can all affect the apparent contrast of an image. Experience indicated that it is sometimes useful to include a known "dark spot" from a defect or dust particle in the original image that can serve as the

"optically dark" reference region. Comparison of the absolute brightness from one sample to another is also difficult; care must be taken to ensure that all the relevant experimental conditions (probe current, sample tilt, etc.) are as identical as possible. In particular, since the parabolloidal mirror has a well-defined focal spot, sample holder height adjustments may be necessary in order to maximize the collection efficiency. In general, most of the CL images in these studies were taken with the following key parameters: spectrometer entrance/exit slit at 0.5 mm, detector acceleration voltage at 1200V, current preamplifiers set at ~ 5-10X above the level at which output showed saturation. The contrast/brightness was then adjusted so that the maximum and minimum (reference dark-spot), as indicated on the SUN workstation prior to capture, spans 1/5 to 4/5 of the total dynamic range (8-bit grayscale). In this manner, some semblance of consistency was achieved among various samples with differing collection conditions.

References

1 G. Mandel, *Self-compensation limited conductivity in binary semiconductors. I. Theory*, Phys. Rev. A **134** (1964) 1073-1079.

2 D. J. Chadi and K. J. Chang, *Self-compensation through a large lattice relaxation in p-type ZnSe*, Appl. Phys. Lett. **55** (1989) 575-577.

3 D. J. Chadi, *Column V acceptors in ZnSe; Theory and experiment*, Appl. Phys. Lett. **59** (1991) 3589-3591.

4 R. M. Park, M. B. Troffer, C. M. Rouleau, J. M. DePuydt, and M. A. Haase, *P-type ZnSe by nitrogen beam doping during molecular beam epitaxial growth*, Appl. Phys. Lett. **57** (1990) 2127-2129.

5 K. Ohkawa, T. Karasawa, and T. Mitsuyu, *Characteristics of p-type ZnSe layers grown by molecular beam epitaxy with radical doping*, Jpn. J. Appl. Phys. **30** (1991) L152.

6 M. A. Haase, J. Qiu, J. M. Depuydt, and H. Cheng, *Blue-green laser diodes*, Appl. Phys. Lett. **59** (1991) 1272-1274.

7 N. Nakayama, S. Itoh, T. Ohata, K. Nakano, H. Okuyama, M. Ozawa, A. Ishibas hi, M. Ikeda, and Y. Mori, *Room temperature continuous operation of blue-green laser diodes*, Electron. Lett. **29** (1993) 1488.

8 A. Ishibashi and S. Itoh, *One-hour-long room temperature CW operation ZnMgSSe-based blue-green laser diodes*, paper presented at the LEOS'94 conference, Boston, MA., Nov. 2, 1994.

9 J. A. Wolk, J. W. Ager, K. J. Duxstad, E. E. Haller, N. R. Taskar, D. R. Dorman, and D. J. Olego, *Local vibrational mode spectroscopy of nitrogen-hydrogen complex in ZnSe*, Appl. Phys. Lett. **63** (1993) 2756-2758.

10 A. Kamata, H. Mitsuhashi, and H. Fujita, *Origin of the low doping efficiency of nitrogen acceptors in ZnSe grown by metalorganic chemical vapor deposition*, Appl. Phys. Lett. **63** (1993) 3353-3355.

11 H. Stanzl, K. Wolf, S. Bauer, W. Kuhn, A. Naumov, and W. Gebhardt, *Low temperature growth and characterization of ZnSe films grown on GaAs*, J. Electron. Mater. **22** (1993) 501-503.

12 W. Kuhn, A. Naumov, H. Stanzl, S. Bauer, K. Wolf, H. P. Wagner, W. Gebhardt, U. W. Pohl, A. Krost, W. Richter, U. Dumichen, and K. H. Thiele, *Low temperature*

MOVPE growth of ZnSe with ditertiarybutylselenide, J. Crystal Growth **123** (1992) 605-610.

13 Sz. Fujita, T. Asano, K. Maehara, and Sg. Fujita, *Nitrogen doping in ZnSe by photo-assisted metalorganic vapor phase epitaxy*, J. Electron. Mater. **23** (1994) 263-268.

14 Sz. Fujita, T. Tojyo, T. Yoshizawa, and Sg. Fujita, *Thermal annealing effects on p-type conductivity of nitrogen-doped ZnSe grown by metalorganic vapor phase epitaxy*, J. Electron. Mater. **24** (1995) 137-141.

15 Y. Fujita, T. Terada, and T. Suzuki, *Growth of nitrogen-doped ZnSe and inhibition of hydrogen passivation of nitrogen acceptor by photoassisted metal-organic chemical vapor deposition*, Jpn. J. Appl. Phys. **34** (1995) L1034-L1036.

16 A. Toda, T. Margalith, D. Imanishi, K. Yanashima, and A. Ishibashi, *MOCVD-grown blue-green laser diode*, Electron. Lett. **31** (1995) 1921-1922.

17 H. Ando, A. Taike, R. Kimura, M. Konagai, and K. Takahashi, *Metalorganic molecular beam epitaxial growth of ZnSe using diethylzinc and diethylselenide*, Jpn. J. Appl. Phys. **25** (1986) L279-L281.

18 N. Kobayashi, Y. Shinoda, and Y. Kobayashi, *Comparative study of ZnSe growth rate by metal organic molecular beam epitaxy using different Zn sources*, Jpn. J. Appl. Phys. Lett. **27** (1988) L1728-L1730.

19 D. Rajavel, J. J. Zinck, and J. E. Jensen, *Metalorganic molecular beam epitaxial growth kinetics and doping studies of (001) ZnSe*, J. Crystal Growth **138** (1993) 19-27.

20 J. Suda, Y. Kawakami, Sz. Fujita, and Sz. Fujita, *Gas-source molecular beam epitaxial growth of (Zn,Mg)(S,Se) using bis-methylcyclopentadienyl-magnesium and hydrogen sulfide*, Jpn. J. Appl. Phys. **33** (1994) L290-L293.

21 M. Imaizumi, Y. Endoh, K. Ohtsuka, T. Isu, and M. Nunoshita, *Active-nitrogen doped p-type ZnSe grown by gas-source molecular beam epitaxy for blue-light-emitting devices*, Jpn. J. Appl. Phys. **32** (1993) L1725-L1727.

22 M. Imaizumi, Y. Endoh, K. Ohtsuka, M. Suita, T. Isu, and M. Nunoshita, *Blue light emitting laser diodes based on ZnSe/ZnCdSe structure grown by gas source molecular beam epitaxy*, Jpn. J. Appl. Phys. **33** (1994) L13-L14.

23 G. Cantwell, W. C. Harsch. H. C. Cotal, B. G. Markey. S. W. S. Mckeever, and J. E. Thomas, *Growth and characterization of substrate-quality ZnSe single crystals using seeded physical vapor transport*, J. Appl. Phys. **71** (1992) 2931-2936.

24 H. C. Cotal. B. G. Markey, S. W. S, Mckeever, G. Cantwell, and W. C. Harsch, *Substrate-quality, single-crystal ZnSe for homoepitaxy using seeded physical vapor transport*, Physica B **185** (1993) 103-108.

25 M. H. Jeon, L.C. Calhoun, and R.M. Park, *Molecular beam epitaxial growth of green light emitting diodes on ZnSe wafers*, J. Electron. Mater. **24** (1995) 177-181.

26 Z. Yu, D. B. Eason, C. Boney, J. Ren, W. C. Hughes, W. H. Rowland, Jr., J. W. Cook, Jr., J. F. Schetzina, G. Cantwell, and W. C. Harsch, *High-brightness II-VI light-emitting diodes grown by molecular-beam epitaxy on ZnSe substrates*, J. Vac. Sci. Technol. B **13** (1995) 711-715.

27 Z. Yu, C. Boney, W. C. Hughes, W. H. Rowland, Jr., J. W. Cook, Jr., J. F. Schetzina, G. Cantwell, and W. C. Harsch, *Blue-green laser diodes on ZnSe substrates*, Electron. Lett. **31** (1995) 1341-1342.

28 J. Jeon, J. Ding, W. Patterson, A. V. Nurmikko, W. Xie, D. C. Grillo, M. Kobayashi, and R. L. Gunshor, *Blue-green injection laser diodes in (Zn,Cd)Se/ZnSe quantum wells,* Appl. Phys. Lett. **59** (1991) 3619-3621.

29 H. Okuyama, T. Miyajima, Y. Morinaga, F. Hiei, M. Ozawa, and K. Akimoto, *ZnSe/ZnMgSSe blue laser diode*, Electron. Lett. **28** (1992) 1798-1799.

30 J. M. Gaines, R. R. Drenten, K. W. Haberern, T. Marshall, P. Mensz, and J. Petruzello, *Blue-green injection lasers containing pseudomorphic* $Zn_{1-x}Mg_xS_ySe_{1-y}$ *cladding layers and operating up to 394K*, Appl. Phys. Lett. **62** (1993) 2462-2464.

31 S. Itoh, H. Okuyama, S. Matsumoto, N. Nakayama, T. Ohata, T. Miyajima, A. Ishibashi, and Y. Mori, *Room temperature pulsed operation of 498 nm laser with ZnMgSSe cladding layers,* Electron. Lett. **29** (1993) 766-768.

32 D. C. Grillo, J. Han, M. Ringle, G. Hua, R. L. Gunshor, P. Kelkar, V. Kozlov, H. Jeon, and A. V. Nurmikko, *Blue ZnSe quantum-well diode laser,* Electron. Lett. **30** (1994) 415-416.

33 S. Itoh, N. Nakayama, S. Matsumoto, M. Nagai, K. Nakano, M. Ozawa, H. Okuyama, S. Tomiya, T. Ohata, M. Ikeda, A. Ishibashi, and Y. Mori, *ZnCdSe/ZnSSe/ZnMgSSe SCH laser diode with a GaAs buffer layer,* Jpn. J. Appl. Phys. **33** (1994) L938-940.

34 A. Salokatve, H .Jeon, J. Ding, M. Hovinen, A. V. Nurmikko, D. C. Grillo, L. He, J. Han, Y. Fan, M. Ringle, R. L. Gunshor, G. C. Hua, and N. Otsuka, *Continuous-wave, room temperature, ridge waveguide green-blue diode lasers,* Electron. Lett. **29** (1993) 2192-2193.

35 A. Ishibashi, *II-VI blue-green laser diodes*, IEEE Journal on Selected Topics in Quantum Electronics **1** (1995) 741-748.

36 For the latest performance and life-time data of blue-green laser diodes from the 3M Company or Philips North American, please check their unofficial blue-green WWW homepage: http://www.nml.org/blue_laser/blue_green_laser.html. The record lifetime is reported to be 3.5 hours under room temperature, CW conditions at 1 mW/facet output power and threshold voltage of 3.8 volts (as of January 1996).

37 F. Hiei, M. Ikeda, M. Ozawa, T. Miyajima, A. Ishibashi, and K. Akimoto, *Ohmic contacts to p-type ZnSe using ZnTe/ZnSe multiquantum wells*, Electron. Lett. **29** (1993) 878-879.

38 Y. Fan, J. Han, L. He, J. Saraie, R. L. Gunshor, M. Hagerott, H. Jeon, A. V. Nurmikko, G. C. Hua, and N. Otsuka, *Graded band gap ohmic contact to p-ZnSe*, Appl. Phys. Lett. **61** (1992) 3160-3162.

39 Y. Fan, *Optimization of compositional grading in Zn(Se,Te) graded ohmic contacts to p-type ZnSe*, Appl. Phys. Lett. **67** (1995) 1739-1741.

40 I. Akasaki, H. Amano, S. Sota, H. Sakai, T. Tanaka, and M. Koike, *Stimulated emission by current injection from an AlGaN/GaN/GaInN quantum well device*, Jpn. J. Appl. Phys. **34** (1995) L1517-1519.

41 J. Cunningham, Private communications.

42 C. A. Coronado, E. Ho, L. A. Kolodziejski, and C. A. Huber, *Photo-assisted molecular beam epitaxy of ZnSe*, Appl. Phys. Lett. **61** (1992) 534-536.

43 E. Ho, C. A. Coronado, and L. A. Kolodziejski, *Elimination of surface site blockage due to alkyl radicals in the MOMBE of ZnSe*, Journal of Electronic Materials: Special Issue on Wide Bandgap II-VI Materials **22** (1993) 473-478.

44 B. A. Banse and J. R. Creighton, *The adsorption of triethylgallium on GaAs (100)*, Surface Sci. **257** (1991) 221-229.

45 A. J. Murrell, A. T. S. Wee , D. H. Fairbrother, N. K. Singh, J. S. Foord, G. J. Davies, and D. A. Andrews, *Surface chemical processes in metal organic molecular-beam epitaxy; Ga deposition from triethylgallium on GaAs (100)*, J. Appl. Phys. **68** (1990) 4053-4063.

46 M. A. Rueter and J. M. Vohs, *Adsorption and reaction of diethylzinc on GaAs (100)*, J. Vac. Sci. Technol. B **10** (1992) 2163-2169.

47 S. Fujii, Y. Fujita, and T. Iuchi, *Photo-assisted MOCVD of CdTe using an excimer laser*, J. Crystal Growth **93** (1988) 750-754.

48 Y. Fujita, T. Terada, S. Fujii, and T. Iuchi, *Reaction measurements and growth of HgTe/CdTe by photo-assisted MOCVD using an excimer laser*, J. Crystal Growth **107** (1991) 621-625.

49 B. J. Morris, *Photochemical organometallic vapor phase epitaxy of mercury cadmium telluride*, Appl. Phys. Lett. **48** (1986) 867-869.

50 J. J. Zinck, P. D. Brewer, J. E. Jensen, G. L. Olson, and L. W. Tutt, *Excimer laser-assisted metalorganic vapor phase epitaxy of CdTe on GaAs*, Appl. Phys. Lett. **52** (1988) 1434-1436.

51 R. N. Bicknell, N. C. Giles, and J. F. Schetzina, *Growth of high mobility n-type CdTe by photoassisted molecular beam epitaxy*, Appl. Phys. Lett. **49** (1986) 1095-1097.

52 R. N. Bicknell, N. C. Giles, and J. F. Schetzina, *P-type CdTe epilayers grown by photoassisted molecular beam epitaxy,* Appl. Phys. Lett. **49** (1986) 1735-1737.

53 Sz. Fujita, A. Tanabe, T. Sakamoto, M. Isemura, and Sg. Fujita, *Investigations of photo-association mechanism for growth rate enhancement in photo-assisted OMVPE of ZnSe and ZnS*, J. Crystal Growth **93** (1988) 259-264.

54 R. L. Gunshor, L. A. Kolodziejski, A. V. Nurmikko, and N. Otsuka, *Strained-Layer Superlattices: Materials Science and Technology*, in Semiconductors and SemiMetals, edited by T. P. Pearsall (Academic Press, Boston, MA 1990), pp. 337-400.

55 R. L. Harper, S. Hwang, N. C. Giles, J. F. Schetzina, D. L. Dreifus, and T. H. Myers, *Arsenic-doped CdTe epilayers grown by photoassociated molecular beam epitaxy*, Appl. Phys. Lett. **54** (1989) 170-172.

56 N. Matsumura, T. Fukada, and J. Saraie, *Laser irradiation during MBE growth of ZnS_xSe_{1-x}: a new growth parameter*, J. Crystal Growth **101** (1990) 61-66.

57 J. Simpson, S. J. A. Adams, J. M. Wallace, K. A. Prior, and B. C. Cavenett, *Photoassisted molecular beam epitaxial growth of ZnSe under high UV irradiances*, Semicond. Sci. Technol. **7** (1992) 460-465.

58 A. Yoshikawa, T. Okamoto, T. Fujimoto, K. Onoue, S. Yamaga, and H. Kasai, *Ar ion laser-assisted MOVPE of ZnSe using DMZn and DMSe as reactants*, Jpn. J. Appl. Phys. **29** (1990) L225-L228.

59 Y. Aoyagi, M. Kanazawa, A. Doi, S. Iwai, and S. Namba, *Characteristics of laser metalorganic vapor-phase epitaxy in GaAs*, J. Appl. Phys. **60** (1986) 3131-3135.

60 S. M. Bedair, J. K. Whisnant, N. H. Karam, D. Griffis, N. A. El-Masry, and H. H. Stadelmaier, *Laser selective deposition of III-V compounds on GaAs and Si substrates*, J. Crystal Growth **77** (1986) 229-234.

61 S. P. DenBaars and P. D. Dapkus, *Atomic layer epitaxy of compound semiconductors with metalorganic precursors*, J. Crystal Growth **98** (1989) 195-208.

62 V. M. Donnelly and J. A. McCaulley, *Selected area growth of GaAs by laser-induced pyrolysis of adsorbed triethylgallium*, Appl. Phys. Lett. **54** (1989) 2458-2460.

63 V. M. Donnelly, C. W. Tu, J. C. Beggy, V. R. McCrary, M. G. Lamont, T. D. Harris, F. A. Baiocchi, and R. F. C. Farrow, *Laser-assisted metalorganic molecular beam epitaxy of GaAs*, Appl. Phys. Lett. **52** (1988) 1065-1067.

64 H. Kukimoto, Y. Ban, H. Komatsu, M. Takechi, and M. Ishizaki, *Selective area control of material properties in laser-assisted MOVPE of GaAs and AlGaAs*, J. Crystal Growth **77** (1986) 223-228.

65 K. Nagata, Y. Iimura, Y. Aoyagi, and S. Namba, *Laser assisted chemical beam epitaxy*, J. Crystal Growth **105** (1990) 52-56.

66 J. Nishizawa, H. Abe, T. Kurabayashi, and N. Sakurai, *Photostimulated molecular layer epitaxy*, J. Vac. Sci. Technol. A **4** (1986) 706-710.

67 H. Sugiura, T. Yamada, and R. Iga, *Mechanism of GaAs selective growth in Ar^+ laser-assisted metalorganic molecular beam epitaxy*, *Jpn. J. Appl. Phys.* **29** (1990) L1-L3.

68 C. W. Tu, V. M. Donnelly, J. C. Beggy, F. A. Baiocchi, V. R. McCrary, T. D. Harris, and M. G. Lamont, *Laser-modified molecular beam epitaxial growth of (Al)GaAs on GaAs and (Ca,Sr)F_2/GaAs substrates*, Appl. Phys. Lett. **52** (1988) 966-968.

69 T. Yamada, R. Iga, and H. Sugiura, *Double-wavelength laser array with InGaAsP/InGaAsP multiple quantum well grown by Ar ion laser-assisted metalorganic molecular beam epitaxy*, Appl. Phys. Lett. **61** (1992) 2449-2451.

70 T. Takahashi, Y. Arakawa, M. Nishioka, and T. Ikoma, *Selective growth of GaAs wire structures by electron beam induced metalorganic chemical vapor deposition*, Appl. Phys. Lett. **60** (1992) 68-70.

71 C. Coronado, *Growth and Characterization of ZnSe by Metalorganic and Gas Source Molecular Beam Epitaxy,* Ph. D. thesis, Massachusetts Institute of Technology, June 1994.

72 H. Hou, Z. Zhang, U. Ray, and M. Vernon, *A crossed laser molecular-beam study of the photodissociation dynamics of $Zn(C_2H_5)_2$ and $(Zn(C_2H_5)_2)_2$ at 248 and 193 nm*, J. Chem. Phys. **92** (1990) 1728-1746.

73 A. Yoshikawa, T. Okamoto, and T. Fujimoto, *Effects of Ar ion laser irradiation on MOVPE of ZnSe using DMZn and DMSe as reactants*, J. Crystal Growth **107** (1991) 653-658.

74 Y. Okada, T. Sugaya, O. Shigeru, T. Fujita, and M. Kawabe, *Atomic hydrogen-assisted GaAs molecular beam epitaxy*, Jpn. J. Appl. Phys. **34** (1995) L238-L244.

75 M. Sato, *Effect of plasma-generated hydrogen radicals on the growth of GaAs using trimethylgallium*, Jpn. J. Appl. Phys. **34** (1995) L93-L96.

76 J. Qiu, J. M. DePuydt, H. Cheng, and M. A. Haase, *Heavily doped p-ZnSe:N grown by Molecular Beam Epitaxy*, Appl. Phys. Lett. **59** (1991) 2992.

77 M. Ringle, D. C. Grillo, J. Han, R. L. Gunshor, G. C. Hua, and A. V. Nurmikko, *Compositional control of (Zn,Mg)(S,Se) epilayers grown by MBE for II-VI blue green laser diodes*, Inst. Phys. Conf. Ser. No 141 (1994) Chapter 5, 513-518.

78 K. Lu, J. L. House, P. A. Fisher, C. A. Coronado, E. Ho, G. S. Petrich, and L. A. Kolodziejski, *(In,Ga)P buffer layers for ZnSe-based visible emitters*, J. Crystal Growth **138** (1994) 1-7.

79 S. Myhajlenko, J. L. Batstone, H. J. Hutchinson, and J. W. Steeds, *Luminescence studies of individual dislocations in II-VI (ZnSe) and III-V (InP) semiconductors*, J. Phys. C **17** (1984) 6477-6492.

80 J. Saraie, N. Matsumura, M. Tsubokura, K. Miyagawa, and N. Nakamura., *Y-Line emission and lattice relaxation in MBE-ZnSe and -ZnSSe on GaAs*, Jpn. J. Appl. Phys. **28** (1989) L108-L111.

81 S. Satoh, and K. Igaki, *Photoluminescence and electrical properties of undoped and Cl-doped ZnSe*, Jpn. J. Appl. Phys. **22** (1983) 68-75.

82 K. Shahzad, J. Petruzzello, D. J. Olego, D. A. Cammack, and J. M. Gaines, *Distortion of excitonic emission bands due to self-absorption in ZnSe epilayers*, Appl. Phys. Lett. **56** (1990) 180-182.

83 C. A. Coronado, E. Ho, P. A. Fisher, J. L. House, K. Lu, G. S. Petrich, and L. A. Kolodziejski, *Gas source molecular beam epitaxy of ZnSe and ZnSe:N*, J. Electron. Mater. **23** (1994) 269-273.

84 S. O. Ferreira, H. Sitter, and W. Faschinger, *Molecular beam epitaxial doping of ZnMgSe using $ZnCl_2$*, Appl. Phys. Lett. **66** (1995) 1518-1520.

85 K. Ohkawa, T. Mitsuyu, and O. Yamazaki, *Characteristics of Cl-doped ZnSe layers grown by molecular beam epitaxy*, J. Appl. Phys. **63** (1987) 3216-3221.

86 Z. Zhu, T. Yao, and H. Mori, *Selective doping of N-type ZnSe layers with chlorine grown by molecular beam epitaxy*, J. Electron Mater. **22** (1993) 663-666.

87 G. Mandel, *Self-compensation limited conductivity in binary semiconductors, I. Theory*, Phys. Rev. **134** (1964) A1073-A1079.

88 D. J. Chadi, and K. J. Chang, *Self-compensation through a large lattice relaxation in p-type ZnSe*, Appl. Phys. Lett. **55** (1989) 575-577.

89 K. W. Kwak, R. D. King-Smith, and D. Vanderbilt, *Pseudopotential total-energy calculations of column-V acceptors in ZnSe*, Physica B **185** (1993) 154-158.

90 R. M. Park, M. A. Haase, and N. M. Salanski, *Photoluminescence properties of nitrogen-doped ZnSe grown by molecular beam epitaxy*, J. Appl. Phys. **58** (1985) 1047-49.

91 K. Ohkawa, T. Karasawa, and T. Mitsuyu, *Characteristics of p-type ZnSe layers grown by molecular beam epitaxy with radical doping*, Jpn. J. Appl. Phys. **30** (1991) L152-L155.

92 R. M. Park, M. B. Troffer, C. M. Rouleau, J. M. Depuydt, and M. A. Haase, *P-type ZnSe by nitrogen beam doping during molecular beam epitaxial growth*, Appl. Phys. Lett. **57** (1990) 2127-2129.

93 Y. Fan, J. Han, L. He, R. L. Gunshor, M. S. Brandt, J. Walker, N. M. Johnson, and A. V. Nurmikko, *Observations on the limits to p-type doping in ZnSe*, Appl. Phys. Lett. **65** (1994) 1001-1003.

94 K. Ohkawa, A. Tsujimura, S. Hayashi, S. Yoshii, and T. Mitsuyu, *ZnSe-based laser diodes and p-type doping of ZnSe*, Physica B **185** (1993) 112-117.

95 Z. Yang, K. A. Bowers, J. Ren, Y. Lansari, J. W. Cook Jr., and J. F. Schetzina, *Electrical properties of p-type ZnSe:N thin films*, Appl. Phys. Lett. **61** (1992) 2671-2673.

96 J. Han, M. D. Ringle, Y. Fan R. L. Gunshor, and A. V. Nurmikko, *X center behavior for holes implied from observation of metastable acceptor states*, Appl. Phys. Lett. **65** (1994) 3230-3232.

97 M. Ikeda, A. Ishibashi, and Y. Mori, *Molecular beam epitaxial growth of ZnMgSSe and its application to blue and green laser diodes*, J. Vac. Sci. Technol. A **13** (1995) 683-689.

98 P. J. Dean, D. C. Herbert, C. J. Werkhoven, B. J., Fitzpatrick, and R. N. Bhargava, *Donor bound-exciton excited states in zinc selenide*, Phys. Rev. B **23** (1981) 4888-4901.

99 Z. Yang, K. A. Bowers, J. Ren, Y. Lansari, J. W. Cook Jr., and J. F. Schetzina, *Electrical properties of p-type ZnSe:N thin films*, Appl. Phys. Lett., **61** (1992) 2671.

100 J. Chevallier, W. C. Dautremont-Smith, C. W. Tu, and S. J. Pearton, *Donor neutralization in GaAs(Si) by atomic hydrogen*, Appl. Phys. Lett. **47** (1985) 108-110.

101 H. Y. Cho, W. C. Choi, and S. Min, *Positively charged states of a hydrogen atom in p-type InP*. Appl. Phys. Lett. **63** (1993) 1558-1560.

102 N. M. Johnson, R. D. Burnham, R. A. Street, and R. L. Thornton, *Hydrogen passivation of shallow-acceptor impurities in p-type GaAs*, Phys. Rev. B **33** (1986) 1102-1105.

103 D. M. Kozuch, M. Stavola, S. J. Pearton, C. R. Abernathy, and W. S. Hobson, *Passivation of carbon-doped GaAs layers by hydrogen introduced by annealing and growth ambients*, J. Appl. Phys. **73** (1993) 3716-3724.

104 R. Rahbi, B. Pajot, J. Chevallier, A. Marbeuf, R. C. Logan, and M. Gavand, *Hydrogen diffusion and acceptor passivation in p-type GaAs*, J. Appl. Phys. **73** (1993) 1723-1731.

105 For example, see: S. J. Pearton, J. W. Corbett, and M. Stavola, *Hydrogen in crystalline semiconductors*, (Springer-Verlag, Berlin, 1991)

106 A. Kamata, H. Mitsuhashi, and H. Fujita, *Origin of the low doping efficiency of nitrogen acceptors in ZnSe grown by metalorganic chemical vapor deposition*, Appl. Phys. Lett. **63** (1993) 3353-3354.

107 J. A. Wolk, J. W. Ager, K. J. Duxstad, E. E. Haller, N. R. Taskar, D. R. Dorman, and D. J. Olego, *Local vibrational mode spectroscopy of nitrogen-hydrogen complex in ZnSe*, Appl. Phys. Lett. **63** (1993) 2756-2758.

108 P. A. Fisher, E. Ho, J. L. House, G. S. Petrich, L. A. Kolodziejski, J. Walker and N. M. Johnson, *P-type and n-type doping of ZnSe: effects of hydrogen incorporation*, J. Crystal Growth **150** (1995) 729-733.

109 E. Ho, P. A. Fisher, J. L. House, G. S. Petrich, L. A. Kolodziejski, J. Walker and N. M. Johnson, *Hydrogen passivation in nitrogen and chlorine-doped ZnSe films grown by gas source molecular beam epitaxy*, Appl. Phys. Lett. **66** (1995) 1062-1064.

110 K. Ogata, D. Kawaguchi, T. Kera, Sz. Fujita, and Sg. Fujita, paper presented at the Seventh International Conference on II-VI Compounds and Devices, August 13-18, 1995, Edinburgh, Scotland, UK.

111 M. Imaizumi, Y. Endoh, K. Ohstuka, T. Isu, and M. Nunoshita, *Active-nitrogen doped p-type ZnSe grown by gas source molecular beam epitaxy*, Jpn. J. Appl. Phys. **32** (1994) L1725-L1727.

112 M. Imaizumi, Y. Endoh, K. Ohstuka, M. Suita, T. Isu, and M. Nunoshita, *Blue light emitting laser diodes based on ZnSe/ZnCdSe structures grown by gas source molecular beam epitaxy*, Jpn. J. Appl. Phys. **33** (1994) L13-L14.

113 D. Rajavel, J. J. Zinck, and J. E. Jensen, *Metalorganic molecular beam epitaxial growth kinetics and doping studies of (001) ZnSe)*, J. Crystal Growth **138** (1994) 19-27.

114 Z. Yu, D. B. Eason, C. Boney, J. Ren, W. C. Hughes, W. H. Rowland Jr., J. W. Cook, Jr., J. F. Schetzina, G. Cantwell, and W. C. Harsch, *High-brightness II-VI light-emitting diodes grown by molecular-beam epitaxy on ZnSe substrates,* J. Vac. Sci. Technol. B **13** (1995) 711-715.

115 M. H. Jeon, L. C. Calhoun, and R. M. Park, *Molecular beam epitaxial growth of green light emitting diodes on ZnSe wafers*, J. Electron. Materials **24** (1995) 177-181.

116 Z. Yu, C. Boney, W. C. Hughes, W. H. Rowland Jr., J. W. Cook, Jr., J. F. Schetzina, G. Cantwell, and W. C. Harsch, *Blue-green laser diodes on ZnSe substrates,* Electron. Lett. **31** (1995) 1341-1342.

117 L. H. Kuo, L. Salamanca-Riba, B. J. Wu, G. Hofler, J. M. Depuydt, and H. Cheng, *Dependence of the density and type of stacking faults on the surface treatment of the substrate and growth mode in ZnSxSe10x/ZnSe buffer layer/GaAs heterostructures*, Appl. Phys. Lett. **67** (1995) 3298-3300.

118 S. Guha, H. Munekata, and L. L. Chang, *Structural quality and the growth mode in epitaxial ZnSe/GaAs(100)*, J. Appl. Phys. **73** (1993) 2294-2300.

119 W. Xie, D. C. Grillo, R. L. Gunshor, M. Kobayashi, H. Jeon, J. Ding, A. V. Nurmikko, G. C. Hua, and N. Otsuka, *Room temperature blue light emitting p-n diodes from Zn(S,Se)-based multiple quantum well structures*, Appl. Phys. Lett. **60** (1992) 1999-2001.

120 S. Guha, J. M. DePuydt, M. A. Haase, J. Qui, and H. Cheng, *Degradation of II-VI based blue-green light emitters*, Appl. Phys. Lett. **63** (1993) 3107.

121 G. C. Hua, N. Otsuka, D. C. Grillo, Y. Fan, J. Han, M. D. Ringle, R. L. Gunshor, M. Hovinen and A. V. Nurmikko, *Microstructure study of a degraded pseudomorphic separate confinement heterostructure blue-green laser diode*, Appl. Phys. Lett. **65** (1994) 1331-1333.

122 H. Ehrenreich and J. P. Hirth, *Mechanism for dislocation density reduction in GaAs crystals by indium addition*, Appl. Phys. Lett. **46** (1985) 668-670.

123 E. D. Bourret, M. B. Tabache, J. W. Beeman, A. G. Elliot and M. Scott, *Silicon and indium doping of GaAs: measurements of the effect of doping on mechanical behavior and relation with dislocation formation*, J. Crystal Growth. **85** (1987) 275-281.

124 Y. Fan, J. Han, L. He, J. Saraie, R. L. Gunshor, M. Hagerott, H. Jeon, A. V. Nurmikko, G. C. Hua, and N. Otsuka, *Graded band gap ohmic contact to p-ZnSe*, Appl. Phys. Lett. **61** (1992) 3160-3162.

125 Y. Lansari, J. Ren, B. Sneed, K. A. Bowers, J. W. Cook, Jr., and J. F. Schetzina, *Improved ohmic contacts for p-ZnSe and related p-on-n diode structures*, Appl. Phys. Lett. **61**, (1992) 2554-2556.

126 B. J. Skromme, M. C. Tamargo, F. S. Turco, S. M. Shibli, W. A. Bonner, and R. E. Nahory, *Characterization of heteroepitaxial ZnSe grown by MBE on GaAs, AlAs and InGaAs*, Proceedings of the Fifteenth International Symposium on Gallium Arsenide and Related Compounds (1989) 205-210.

127 B. J. Skromme, M. C. Tamargo, J. L. de Miguel, and R. E. Nahory, *Photoluminescence characterization of heteroepitaxial ZnSe/GaAs and ZnSe/AlAs grown by MBE*, Proceedings of the Epitaxy of semiconductor layered structures Symposium **102** (1988) 577-582.

128 G. C. Hua, N. Otsuka, W. Xie, D. C. Grillo, M. Kobayashi, M. and R. L. Gunshor, *Growth and characterization of ZnSe/ZnCdSe diode structures on (In,Ga)As buffer layers*, Proceedings of the Materials Research Society Symposium **242** (1992) 221-226.

129 S. Saito, Y. Nishikawa, M. Onomura, P. J. Parbrook, M. Ishikawa, and G. Hatakoshi, *Surface preparation effects for molecular beam epitaxial growth of ZnSe layer on InGaP layers*, Jpn.ese Journal of Applied Physics **33** (1994) L705-707.

130 K. Itaya, M. Ishikawa, and G. Hatakoshi, *Current-voltage characteristics of p-p isotype InGaAlP/GaAs heterojunction with a large valence-band discontinuity*, Jpn. J. Appl. Phys. **32** (1993) 1919-1922.

131 T. Ylkogawa, T. Saitoh, J. Hoshina, and T. Narusawa, *Effect of strain on ZnSe/AlGaInP heterostructures grown by MOVPE*, J. Crystal Growth **99** (1990) 418-421.

132 K. Iwata, H. Asahi, J. H. Kim, X. F. Liu, S. Gonda, Y. Kawaguchi, A. Ohki, and T. Matsuoka, *Gas source MBE growth of InAlP band offset reduction layers on p-type ZnSe*, J. Crystal Growth **150** (1995) 833-837.

133 K. Iwata, H. Asahi, T. Ogura, J. Sumino, S. Gonda, A. Ohki, Y. Kawaguchi, and T. Matsuoka, *Low temperature grown Be-doped InAlP band offset reduction layer to p-type ZnSe*, Proceedings of the Seventh International Conference on Indium Phosphide and Related Materials (1995) 183-186.

134 E. Ho, G. S. Petrich, and L. A. Kolodziejski, *Comparison of hydrogen passivation of ZnSe:N using gas source and conventional molecular beam epitaxy*, paper presented at the Seventh International Conference on II-VI Compounds and Devices, August 13-18, 1995, Edinburgh, Scotland, UK.

135 M. Onomura, M. Ishikawa, Y. Nishikawa, S. Saito, P. J. Parbrook, K. Nitta, J. Rennie, and G. Hatakoshi, *Blue-green laser diode operation of CdZnSe/ZnSe MQW structures grown on InGaP band offset reduction layers*, Electron. Lett. **29** (1993) 2114-2115.

136 M. Ishikawa, Y. Nishikawa, S. Saito, M. Onomura, P. J. Parbrook, K. Nitta, J. Rennie and G. Hatakoshi, *Low voltage carrier injection in ZnSe-based blue-green laser diodes on p-type GaAs substrates with InGaAIP band offset reduction layers*, Proceedings of the 14th IEEE International Semiconductor Laser Conference (1994) 199-200.

137 M. K. Lee, H. C. Liao, C. C. Hu, and M. Y. Yeh, *Heterojunction ZnSe/InP field-effect transistor by metalorganic chemical vapor deposition*, Materials Chemistry and Physics **38** (1994) 398-401.

138 D. Coquillat, D. Bouchara, A. Abounadi, A. Ribayrol, J. P. Lascaray, J. Calas, A. Haidoux, P. Tomasini, and M. Maurin, *Optical measurements in MOVPE-grown ZnSe/InP epilayers*, Physica Status Solidi B **180** (1993) 383-389.

139 A. Haidoux, P. Tomasini, M. Maurin, J. C. Tedenac, D. Coquillat, A. Ribayrol, J. P. Lascaray, D. Bouchara, A. Abounadi, J. Calas, and B. Ducourant, *Heterostructure of binaries II-VI semiconductors ZnTe and ZnSe/III-V (GaAs, InP, GaSb)*, Journal De Physique IV **3** (1993) 147-54.

140 H. C. Tseng, J. L. Shen, and R. C. Hsieh, *DC and AC characteristics of ZnSe/Ge/GaAs and ZnSe/InGaAs/GaAs lattice-matched heterojunction bipolar transistors grown by metal-organic chemical vapor deposition*, Jpn. J. Appl. Phys. **33** (1994) L1759-1761.

141 J. Schreiber, and S. Hildebrandt, *Basic dislocation contrasts in SEM-CL/EBIC on III-V semiconductors*, Mater. Sci. Eng. B **24** (1994) 115-120.

142 T. Uemoto, A. Kamata, H. Misuhashi, K. Hirahara, and T. Beppu, *Lattice matching effect on luminescence properties of n-ZnSSe on GaAs*, J. Crystal Growth, **99** (1990) 422-426.

143 J. L. Batstone and J. W. Steeds, *TEM and CL characterization of dislocations in OMCVD ZnSe*, in Microscopy of semiconducting materials, Proceedings of the Royal Microscopical Society Conference (1985) 383-388.

144 S. Guha, H. Munekata, and L. L. Chang, *Structural quality and the growth mode in epitaxial ZnSe/GaAs(100)*, J. Appl. Phys. **73** (1993) 2294-2300.

145 L. H. Kuo, L. Salamanca-Riba, J. M. Depuydt, H. Cheng and J. Qiu, *Misfit dislocation nucleation in doped and undoped ZnSe/GaAs*, Appl. Phys. Lett. **63** (1993) 3197-3199.

146 L. H. Kuo, L. Salamanca-Riba, B. J. Wu, G. M. Haugen, J. M. Depuydt, G. Hofler, and H. Cheng, *Generation of degradation defects, stacking faults, and misfit dislocations in ZnSe-based films grown on GaAs*, J. Vac. Sci. Technol. B **13** (1995) 1694-704.

147 S. Ruvimov, E. D. Bourret, J. Washburn, and Z. Liliental-Weber, *Nucleation and evolution of misfit dislocations in ZnSe/GaAs (001) heterostructures grown by low-pressure organometallic vapor phase epitaxy*, Appl. Phys. Lett. **68** (1996) 346-348.

148 M. Yamaguchi, A. Yamamoto, and M. Kondo, *Photoluminescence of ZnSe crystals diffused with a group-III element*, J. Appl. Phys. **48** (1977) 5237-5244.

149 J. Gutowski, N. Presser, and G. Kudlek, *Optical properties of ZnSe epilayers and films*, Phys. Status Solidi A **120** (1990) 11-59.

150 A. D. Raisanen, L. J. Brillson, L. Vanzetti, A. Bonanni, and A. Franciosi, *Deep level formation at ZnSe/GaAs(100) interface*, J. Vac. Sci. Technol. **13** (1995) 1705-1710.

151 S. Akram, H. Ehsani, I. B. Bhat, and S. K. Ghandhi, *Characteristics of ZnSe layers grown on Zn-stabilized and Se-stabilized GaAs substrates*, Proceedings of the materials research society **242** (1992) 261-266.

152 A. Bonanni, L. Vanzetti, L. Sorba, A. Franciosi, M. Lomascolo, P. Prete, and R. Cingolani, *Optimization of interface parameters and bulk properties in ZnSe-GaAs heterostructures*, Appl. Phys. Lett. **66** (1995) 1092-1094.

153 L. Vanzetti, A. Bonanni, G. Bratina, L. Sorba, A. Franciosi, M. Lomascolo, D. Greco, and R. Cingolani, *Influence of growth parameters on the properties of ZnSe-GaAs (001) heterostructures*, J. Crystal Growth **150** (1995) 765-769.

154 J. Qiu, Q. D. Qian, M. Kobayashi, R. L. Gunshor, D. R. Menke, D. Li, N. Otsuka, and L. A. Kolodziejski, *Low interface state densities in as-grown epitaxial ZnSe/epitaxial GaAs heterostructures*, Proceedings of the international symposium of GaAs and related compounds (1990) 201-206.

155 G. Bratina, L. Vanzetti, L. Sorba, G. Biasiol, A. Franciosi, M. Peressi, and S. Baroni, *Lack of band-offset transitivity for semiconductor heterojunctions with polar orientation: ZnSe-Ge(001), Ge-GaAs(001), and ZnSe-GaAs(001)*, Phys. Rev. B **50** (1994) 11723-11792.

156 R. L. Gunshor, private communications.

157 J. M. Gaines, J. Petruzzello, and B. Greenberg, *Structural properties of ZnSe films grown by migration enhanced epitaxy*, J. Appl. Phys. **73** (1993) 2835-2840.

158 J. M. Gaines and C. A. Ponzoni, *Beating in RHEED oscillations observed during MEE growth of ZnSe*, Surf. Sci. **290** (1993) 172-178.

159 J. Petruzzello, J. gaines, P. van der Sluis, D. Olego, and C. Ponzoni, *Effect of N doping on the structural properties of ZnSe epitaxial layers grown by molecular beam epitaxy*, Appl. Phys. Lett. **62** (1993) 1496-1498.

160 L. H. Kuo, L. Salamanca-riba, J. M. Depuydt, H. Cheng, and J. Qiu, *Dislocation nucleation mechanism in nitrogen-doped ZnSe/GaAs*, Phil. Mag. **69** (1994) 301-313.

161 E. Fuchs, H. Oppolzer, and H. Rehme, Particle Beam Microanalysis: Fundamentals, Methods And Applications, (VCH Verlagsgesellschaft, Weinheim, 1990).

162 A. Benninghoven, F. G. Rudenauer, and H. W. Werner, Secondary Ion Mass Spectrometry. Basic Concepts, Instrumental Aspects, Applications and Trends, (Wiley, New York, 1987).

163 R. G. Wilson, F. A. Stevie, and C. W. Magee, Secondary Ion Mass Spectrometry. A Practical Handbook for Depth Profiling and Bulk Impurity Analysis, (Wiley & Sons, New York, 1989).

164 J. C. Vickerman, A. Brown, and N. M. Reed, *Secondary Ion Mass Spectrometry. Principles and Applications*, (Clarendon Press, Oxford, 1989).

165 H. H. Anderson, and H. L. Bay, *Ion sputtering by particle bombardment I*, Springer Series Topics in Applied Physics **47**, edited by R. Behrisch, (Springer Verlag: Berlin, 1981) pp. 145.

166 H. A. Storms, K. F. Brown, and J. D. Stein, *Evaluation of a cesium positive ion source for secondary ion mass spectrometry*, Anal. Chem. **49** (1977) 2023-2030.

167 C. A. Andersen, J. R. Hinthorne, *Ion microprobe mass analyzer*, Science **175** (1972) 853-860.

168 A. Brown, J. C. Vickerman, *Static SIMS studies of adsorbate structure. II. CO adsorption on Pd(111); adsorbate-adsorbate interactions on Ru(001), Ni(111) and Pd(111)*, Surf. Sci. **124** (1983) 267-278.

169 J. Maul and K. Wittmaack, *Secondary ion emission from silicon and silicon oxide*, Surf. Sci. **47** (1975) 358-369.

170 Y. Kawakami, T. Ohnakado, M. Tsuka, S. Tokudera, Y. Ito, Sz. Fujita, and Sg. Fujita, *P-type ZnSe grown by molecular beam epitaxy with remote microwave plasma of N_2*, J. Vac. Sci. Technol. B **11** (1993) 2057-2061.

171 D. B. Holt and D. C. Joy, SEM microcharacterization of semiconductors, (Academic Press, San Diego, 1989).

172 J. I. Goldstein and H. Yakowitz, Practical scanning electron microscopy; electron and ion microprobe analysis, (Plenum Press, New York, 1975).

173 P. Duncumb and P. K. Shields, *The present state of quantitative X-ray microanalysis Part 1: Physical basis*, Brit. J. Appl. Phys. **14** (1963) 617-625.

174 K. Murata, T. Matsukawa, and R. Shimizu, *Monte Carlo calculations on electron scattering in a solid target*, Jpn. J. Appl. Phys. **10** (1971) 678-686.

175 K. Kanaya and S. Okayama, *Penetration and energy-loss theory of electrons in solid targets*, J. Phys. D **5** (1972) 43-58.

176 S. Mora, N. Romeo, and L. Tarricone, *Minority carriers diffusion length in ZnSe by SPV method*, Solid State Commun. **33** (1980) 1147-1149.